Development of Raman and Electrochemical Biosensors and Fabrication of Hybrid Materials for Supercapacitors

by

Yajiao Yu

A dissertation submitted to the Graduate Faculty of
Auburn University
in partial fulfillment of the
requirements for the Degree of
Doctor of Philosophy

Auburn, Alabama
August 3, 2013

Keywords: Surface-enhanced Raman Scattering, Electrochemical proximity assay, Supercapacitor

Approved by

Curtis Shannon, Chair, Professor of Chemistry
Christopher Easley, Assistant Professor of Chemistry
Wei Zhan, Associate Professor of Chemistry
Minseo Park, Associate Professor of Physics

Abstract

This dissertation describes the development of sensors for the detection of biologically relevant molecules and the fabrication of hybrid supercapacitor materials for energy storage purposes. Specifically, DNA sensors based on surface-enhanced Raman spectroscopy (SERS) and electrochemical proximity assay (ECPA) are described. Both sensors have great potential for point-of-care testing and research has focused recently on point-of-care analysis with the goal of speeding up the disease diagnosis. It is also convenient for use in poor or remote areas where highly trained personnel are not readily available.

Hybrid supercapacitors, on the other hand, exhibit high power and energy densities and can undergo several charging/discharging cycles without significant loss in performance. Mn_3O_4 has emerged recently as a potential candidate due to the fact that Mn is earth-abundant and therefore inexpensive. The oxide can be easily deposited electrochemically on substrates such as stainless steel and carbon fibers to form hybrid materials that exhibit higher performances than the oxide alone.

Chapter 1 gives a brief introduction of the principles of surface-enhanced Raman spectroscopy and the fabrication techniques of surface-enhanced Raman spectroscopy substrates. Also, recent biosensor developments based on surface-enhanced Raman spectroscopy and electrochemistry techniques are described. In addition, the principles of supercapacitors are described and their preparation is briefly reviewed.

Chapter 2 describes the preparation of SERS-active substrates and their biosensor applications. Ag/Au film over nanosphere substrates (FONs) have been prepared, and a large enhancement of Raman intensity was achieved. In addition, the distance dependence of the Raman signal from the nanostructure responsible for signal enhancement is reported.

Chapter 3 describes a DNA biosensor system, developed for detection of DNA sequences using Ag/Au FONs substrate. By incorporating the sensor system into a microfluidic channel, the reproducibility of the system was significantly improved.

Chapter 4 presents two kinds of hybrid materials, namely carbon fiber and stainless steel fiber with Mn_3O_4 for supercapacitor application. These materials were found to exhibit very high capacitance.

Chapter 5 deals with the optimization of the ECPA biosensor system. By incorporating uracil bases into DNA sequences, a reusable sensor was successfully developed with good signal recovery and selectivity. A faster detection (3 minutes) was also achieved, and the detection of insulin concentration in blood serum was demonstrated.

Finally, Chapter 6 summarizes the research work and presents possible future directions that would follow this work.

Acknowledgments

I would like to express my deepest gratitude to my advisor Dr. Curtis Shannon for his continuous guidance, constant motivation, and endless support for my research study at Auburn University. I am so grateful for his kindness and encouragement, which will be always remembered. Without him, I could not have had the chance to finish my studies. Also, his enthusiasm for science will continuously inspire me for my career pursuits.

I would like to give thanks to all the committee members: Dr. Christopher Easley, Dr. Minseo Park, and Dr. Wei Zhan for their precious suggestions and helpful guidance during my research. I would also like to thank my outside reader Dr. Alex Simonian for his participation in evaluating my work. I would like to give special thanks to Dr. Easley for his kindness and valuable suggestions.

I would like to give thanks to all the faculty, staff, and friends from the chemistry department because I have received so much support from them. I would like to give thanks to Dr. Rik Blumenthal for his help with the XRD instrument. Also, I would like to thank Dr. Michael Miller from biology department, Dr. Virginia Davis from chemical engineering department, and Dr. Xinyu Zhang from polymer and fiber engineering department for their help and valuable suggestions. I would like to give thanks to all my friends from various departments and these working outside the campus.

I would like to give thanks to Jiaming Hu and Kennon Deal from Dr. Easley' s lab for the great collaborations works and other members of his lab. Also, I would like to give thanks to Dr. Kai, Jiang, Dr. Chengguo and other members from Dr. Zhan's lab.

I would like to give thanks to my wonderful colleagues in Dr. Shannon's group. Dr. Tsunghsueh Wu, Dr. Junxua Xin, Dr. Anand Sankarraj, Dr. Hongxia Zhang, Dr. Sridevi Ramakrishnan, Dr. Rajakumari Ramaswamy, Dr.Weiping Li, Dr. Tanyu Wang, Mrs. Sanghapi Ndzesse, and Mary Miller. And I would like to wish the best to all the new graduate students, Sanjun Fan, Apu Mazumder, and Li Zhang. I am so thankful to have them as my labmates.

I would like to thank my family, my parents, my two sisters, and elder brother for their support and encouragement during my graduate studies. Last but not least, I would like to express special thanks to my husband Bianzhu Fu, for his unconditioned love and his endless encouragement during my graduate studies and my life.

Table of Contents

List of Tables

List of Figures

List of Abbreviations

SERS	surface-enhanced Raman scattering
FONs	film over nanosphere substrate
EBL	electron beam lithography
NIL	nanoimprint lithography
NSL	nanosphere lithography
SERRS	surface Enhanced Resonant Raman Spectroscopy
MCH	mercaptohexanol
EDLCs	electric double layer capacitors
OHP	outer Helmholtz plane
IHP	inner Helmholtz plane
ATP	4-aminothiophenol
SAM	self-assembled monolayers
R6G	rhodamine 6G
PDMS	poly dimethylsiloxane
PEI	polyethylenimine
XRD	X-ray diffraction
SEM	scanning electron microscopy
ECPA	electrochemical proximity assay

Chapter 1

Introduction

1.1 Surface-enhanced Raman scattering

Raman spectroscopy involves excitation of molecules by using an intense light source and measuring the scattered radiation by the molecules. Because of the low probability of light being scattered, the Raman intensity is inherently weak. Therefore, a lot of effort has been invested in order to improve the intensity of the scattered light. One technique that has been developed to improve the intensity is called Surface-enhanced Raman Spectroscopy/scattering (SERS). This technique was first reported by Fleischmann *et al*. in 1974[1]. They observed that, when pyridine was absorbed on a roughened silver electrode, the Raman intensity increased by a factor of 10^6 compared to pyridine not absorbed on the surface. Since then, a lot of work has been done to understand the reason for the enhancement. In addition to Fleischmann's group, the research groups of Van Duyne and Jeanmaire, and Albrecht and Creighton, independently reported the significant enhancement of the Raman scattering when molecules are adsorbed on a metal surface [2-3]. Van Duyne and Jeanmaire concluded that a possible contributing factor is from the change of the electric field experienced by the molecules. This phenomenon is known as electromagnetic enhancement (EM). At the same time, Albrecht and Creighton also reported that Raman scattering was enhanced by electron transfer between the molecules and the metal substrate. This is referred to as chemical enhancement. Other mechanisms and models that explain the phenomenon have been reported. Although the mechanisms leading to the

enhancement are still not completely understood, electromagnetic and chemical enhancement are accepted as the two main explanations for the SERS enhancement. The electromagnetic enhancement is thought to be the main contribution resulting in an enhancement factor of 10^6 to 10^{10}. The chemical enhancement usually contributes only a factor of 10^2 to the enhancement. With the development of SERS in recent years, research interests have shifted to practical applications [4-8]. To better understand the SERS behavior, some fundamentals, including the two main mechanisms, electromagnetic enhancement, and chemical enhancement will be inclusively depicted in the following sections.

1.1.1 Mechanisms

Electromagnetic enhancement mechanism

Electromagnetic enhancement (EM) focuses on enhanced electromagnetic fields induced by the change of surface plasmons that reside on metal surface [9-11], while the chemical enhancement can be supported by the charge transfer between the adsorbents and the metal surfaces [12].

Surface plasmon in conduction materials is formed due to rapid oscillation of their electron density induced by incident light. The particle resulting from the quantization of the oscillation is termed “plasmon.” When plasmon is restricted to surfaces and interacts strongly with incident light, a polariton is formed, also known as nonradiative evanescent wave. The wave resides at the interface of the materials with positive dielectric constant and those with negative dielectric constant. The plasmon can either be localized or propagating. When the nanostructure dimensions of conducting materials are smaller than the wavelength of the excitation light, such as metallic nanoparticles, the formed evanescent wave is known as localized surface plasmon resonance (LSPR). The most widely accepted model of the LSPR

phenomenon on nanoparticle surface is illustrated in Figure 1.1 (a) [15]. When the nanoparticle is irradiated by the incident light, the oscillating electric field localized on the surface can cause the metal electrons to oscillate coherently. As shown in Figure 1.1 (a), when the charged cloud of conduction electrons is oscillated away from the nuclear frame work of the nanoparticle, strong coulombic attraction energy arises and forces the oscillation of the conduction electron cloud back to the nuclear framework. This back and forth oscillation results in a large enhancement of electromagnetic field of the light at the surface of nanoparticle. The magnification of both the incident EM field and the Raman scattering field composes the SERS EM enhancement mechanism [10]. Experimentally, as illustrated in Figure 1.1 (b), the excitation peak represents the excitation of the LSPR at the surface of metal nanoparticle. In this figure, the excitation peak at 420 nm is measured from silver colloids solution.

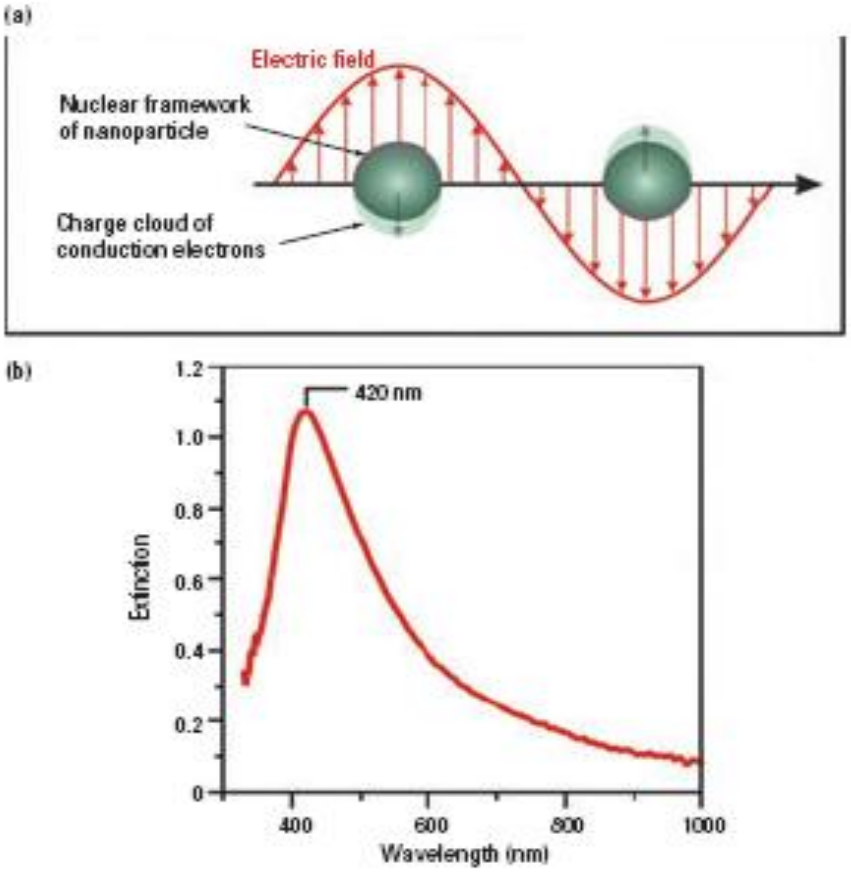

Figure 1.1 (a) Model of LSPRs at the spherical nanoparticle surface (b) Extinction spectrum of silver nanoparticle. The peak indicates the excitation of the LSPR. Taken from Ref 15 with permission.

The model of a metal sphere used in Figure 1.1 is used to illustrate the EM mechanism for simplicity. The ideal metal sphere is used because the electric field is homogeneous around the nanosphere. For a nanoparticle with a radius significantly smaller than the wavelength of the incident light, the electric field due to plasmon on the surface of the metal sphere is related to the electric field of the incident light according to the following Equation (1)

$$E\ (\text{induced}) = \left(\frac{\varepsilon_1 - 2\,\varepsilon_2}{\varepsilon_1 + 2\,\varepsilon_2}\right) E\ (\text{light}) \qquad (1)$$

where E (induced) and E (light), represent for the electric or electromagnetic (EM) field induced on the surface and electric field of the excitation light. There, ε_1 and ε_2 are the complex dielectric function and relative permittivity of the media respectively. Theoretically, from the equation, when ε_1 equals -2 ε_2, an infinite EM is achieved on the surface which is an ideal LSPR condition. Research experiments can benefit from this study by the relative adjustment of the complex dielectric function and the media phase to satisfy the condition for LSPR. Physical properties of the nanosphere surface can also be modified to enhance LSPR [107, 15].

Chemical enhancement mechanism

The chemical enhancement mechanism is thought to contribute an average enhancement factor of 10^2 to the total surface signal. This mechanism includes any enhancement of the Raman intensity of surface species via the formation of a chemical bond with the surface. The mechanism is correlated to the charge transfer between the probed molecule and the surface, because charge transfer between the interacting species is one of the most significant characteristics of chemical reactions [13].

1.1.2 Distance dependence

As mentioned earlier, the larger part of the overall enhancement of SERS is due to the EM enhancement mechanism. The EM enhancement is a result of the presence of physical nanostructures at the metal surface. The intensity of the Raman scattering (I) is proportional to the square of the magnitude of any electric fields (E) irradiated on the analyte on the surface as shown in Equation (2).

$$I \propto E^2 \quad \textbf{(2)}$$

The magnitude of EM field includes two parts as defined by the Equation (3).

$$E = Ea + Ep \quad \textbf{(3)}$$

Respectively, Ea and Ep are electric fields induced on the analyte without and with nanostructure feature on the surface.

Since the EM effect is the primary contribution in SERS and electric fields decrease in strength with space from the excitation source, an analyte can benefit from the enhancement even if it is some distance away from the enhancing nanostructure surface. Theoretically, in a sphere model, SERs enhancement (G) is related to the radius of the spherical structure (r) and the distance between analyte and the spherical structure according to the following equation:

$$G = [r / (r + d)]^{10} \quad \textbf{(4)}$$

Experimental studies of the relationship between the enhanced intensity and the distance between the analyte and the spherical metal roughness feature were performed using Al_2O_3 by Duyne's group in 2004 [14]. They used Al_2O_3 deposition layer to control the thickness of the film over nanosphere substrate (FONs) and observed the consistency between the theoretical relationship and the practical use in their fabrication substrate. The calculated value for the size of average

nanostructure feature is 12 nm for their substrate. Experimentally, the Raman enhancement intensity drops by a factor of 10 with an increasing distance of 2 to3 nm.

1.1.3 SERS active substrates

Substrates play a critical role for the SERS techniques. Based on the enhancement mechanism, the properties of the substrates should meet certain requirements. Firstly, since the EM enhancement depends on the phenomenon of LSPR, all of the factors satisfying the LSPR conditions needed to be fulfilled in order to benefit from the enhanced signal. This includes controlling properties of the substrate such as the dimension and shape of nanostructure and the dielectric of the media [15, 109]. Secondly, SERS requires that the feature sizes of metallic nanostructures clearly below the wavelength of the exciting light, because the ability of a metal to show the SERS effect is determined by the frequency dependent complex dielectric function (ε_1) as described in Equation (1). SERS- active nanostructure should have sharp features in order to benefit from the "antenna effect" [108-110]. Furthermore, the enhancement can be highly amplified if the analyte molecule is absorbed between two or more neighboring sharp structures, which are depicted as a "hot spot" [16]. In addition, further requirements are needed for experimental applications: (1) the substrate should have the chemical and biological compatibility with the analytes molecule, (2) it should be inexpensive as well as chemically and temporally stable, (3) tenability and reproducibility of substrates is favorably required for practical studies. Based on these requirements, various methods have been developed to prepare SERS active substrates. For instance, nanoparticle colloids [17-21], metallic rough surfaces [22-23], and periodic nanostructures [24] capable of signal enhancement are summarized in Figure 1.2. The first two categories mainly rely on fundamentally random formations; hence the reproducibility is significantly limited.

Among these studies, the method of electrochemically roughening metal electrodes was used to prepare substrates showing SERS and can usually realize an enhancement factor of 10^6. Colloid dispersion has been successfully prepared by an easy reduction reaction of the respective metal salts as shown in the right top graph in Figure 1.2 [25]. For example, silver and gold nanoparticles can be prepared according to the method of Lee and Meisel by reducing $AgNO_3$ and $HAuCl_4$ [26]. Besides pure metal nanoparticles, some scientists also found that core shell bimetal nanoparticles allow a shift of the resonance frequency as a function of the shell thickness, which is an efficient method for SERS measurement. Moreover, various shapes such as nano-cube, octahedral and nano-rods can be prepared in addition to spherical nanoparticle [17-21]. A nanorod possesses a long axis which can excite the phenomenon of multipolar Plasmon [27-28]. Tian and co-workers studied nanowires made of different metals with different widths and lengths and found that nanowire substrate exhibited better SERS activity than that of a randomly roughened metal surface. In addition to metal nanowires, more complicated structures have been developed as desired. Crescent-shaped metal nanoparticles with three dimensions have been fabricated by Lee *et al*., which shows remarkable enhancement [28].

Although nanoparticle colloids are simple and easy to prepare, they are not always homogeneous or stable. Methods for homogeneous and reproducible substrate fabrication have thus attracted great attention from research scientists. Among all the methods studied, lithography is most often implemented because of its excellent reproducibility. One generally used method is electron beam lithography (EBL) which can prepare highly reproducible patterns of variable shape and tens of nanometers in size. Felidj *et al.* studied SERS enhancement on oblate Au spheroid arrays prepared by EBL and found that they exhibited good reproducibility and resulted in an enhancement factor of 10^5 [29]. Structures with different shapes can be

achieved by EBL technique, including cylinders, square trigonal prisms, or even nanowire arrays [30].

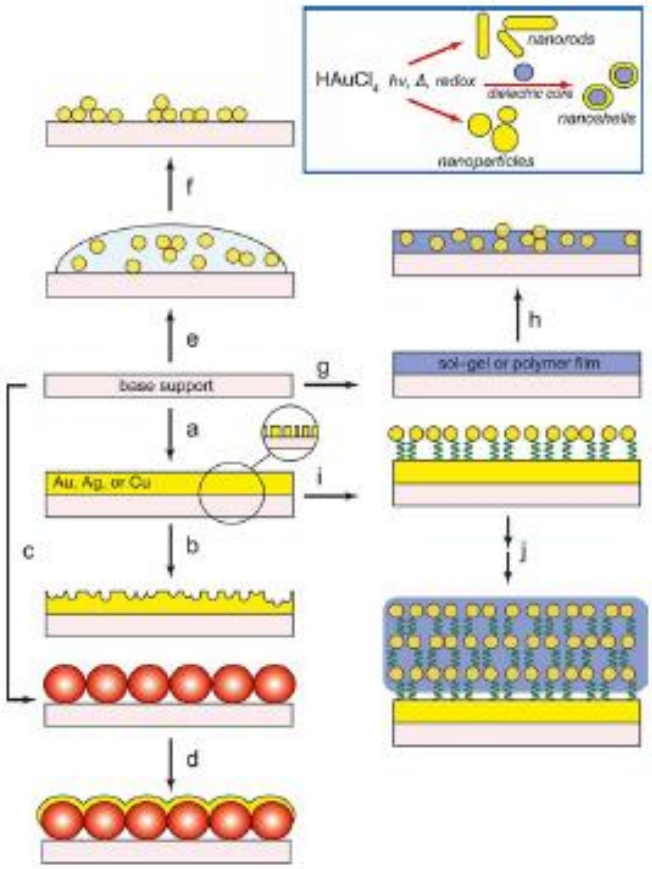

Figure 1.2 Some fabrication processes for nanostructures SERS substrate: (a) sputter coating of metal thin film, (b) electrochemical roughening or corrosive etching, (c) nanosphere deposition (d) sputter coating on deposited nanosphere mask (e) and (f) metal colloid nanosphere SAM, (g) aqueous sol-gel or polymer deposition, (h) metal nanoparticle entrapment in a matrix, (i) layer by layer colloid multiplayer formation, (j) subsequent organosilane overlayer deposition. Top right shows chemical reduction methods used to prepare various metal nanostructures. Taken from Ref 103 with permission.

Another lithographic technique is called nanoimprint lithography (NIL). The fabrication process is as follows: (1) a mold with certain pattern is fabricated, (2) the mold is then used to create a thickness contrast in a resist known as imprinting process, (3) after imprinting, the mold is removed from the resist, resulting in transfer of a contrast pattern to the resist, (4) finally the pattern is transferred by using etching processes to get rid of residue.

In 2012, a novel method with high performance and high flexibility was developed by engineering nanostructures on a silicon base using focused ion beam direct writing (FIBDW) technology [31]. It was found that this technique has great potental for high performance SERS' active substrates development. By reducing the spacing between "hot spots," single molecular detection can be achieved.

The lithographic techniques depicted above can help achieve a substrate surface that is both highly reproducible and adjustable in size and shape. However, the high cost of the fabrication process greatly hinders their applications. Economical methods without loss of the high performance are therefore required.

1.1.4 Nanosphere lithography (NSL) and films over nanospheres (FON)

The technique of Nanosphere lithography (NSL) was first developed by Fischer *et al.* in 1981 [32]. The fabrication process is shown in Figure 1.3. In principle, a solution containing nanospheres such as polystyrene latex spheres of homogeneous diameter is self-assembled on the surface of a substrate to form a two dimensional deposition mask with subsequent deposition of a metal layer. In this technique, chemical modification of the nanosphere surface is needed to improve the stability and ensure the informality of the self-assembled monolayer (SAM) on the

substrate. After the self-assembling process, a thin film of metal is coated by the sputter coating process.

By tuning the size and shape of the nanoparticles used in NSL prepared substrates, the substrates can show good LSPR performance. In 1995 Hulteen and van Duyne[33] developed periodic nanoparticle pattern with nanometer features using single layer and double layer self-assembled sphere masks. They reported the preparation of defect-free substrates at moderate cost and proposed the term nanosphere lithography (NSL). Enhancement factors above 10^7 can be achieved in NSL.

The films over nanospheres (FON) approach is similar to the NSL process except that the spheres are not removed. Enhancement factors of approximately 10^8 were obtained for film over nanosphere, which is comparable with NSL structures.

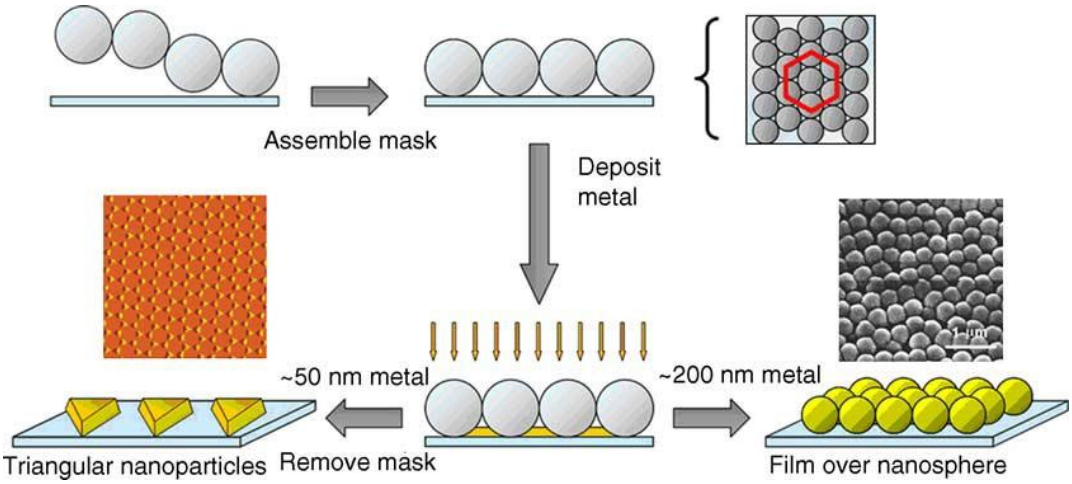

Figure 1.3 Schematic representation of the nanosphere lithography (NSL) fabrication process
Reprinted from Ref 102 with permission.

1.2 Biosensors

According to the definition from International Union of Pure and Applied Chemistry (IUPAC) gold book, a biosensor is "a device that uses specific biochemical reactions mediated by isolated enzymes, immunosystems, tissues, organelles or whole cells to detect chemical compounds usually by electrical, thermal or optical signals" [34]. In a typical design, a biosensor consists of three parts: (1) the sensitive elements or biological sensing material, which incorporates the target bio-analytes, (2) the transducer or detector element, which converts the sensing signal into a clear and measurable readout, (3) the signal processor, which displays the transformed signal in an accessible way. The biological sensing material can be a protein such as an enzyme, a nucleic acid, an antibody, or even a plant, animal and bacterial tissue, and a whole microbial cell [35].

Biosensors can be divided into several categories based on the transducer and detector devices, such as electrochemical, optical, piezoelectric, mass, thermal, and calorimetric [37-41]. Optical methods such as fluorescence, Raman spectroscopy, reflection interference contrast microscopy (RICM), and surface Plasmon resonance (SPR) [42] are widely employed because of their simple and straightforward use. Many optical applications in biosensors are dependent on target molecule labeled with optical reporter molecules, such as radioisotopes, fluorophores, UV-absorbing and Raman-active reporter [43-45]. Electrochemical methods are of great importance because of their low cost and high sensitivity. They can be classified into amperometric, potentiometric, impedance, and conductometric methods [46].

1.2.1 DNA- and Aptamer- based Biosensors

Recently, nucleic acid analysis has played a significant role in the detection of pathogens, genetic diseases and virus infection [45-49]. This analysis has many applications including point-

of-care (POC) diagnostics, along with environmental and food monitoring [46-49]. Conventional DNA hybridization detecting techniques, such as gel electrophoresis or southern blotting are usually time-consuming, laborious and not suitable for on-site monitoring. Generally, the principle of the DNA biosensor is based on the DNA sequences base coupling. The principle relies on the immobilization of a single stranded DNA sequence probe on a surface which can recognize its complementary sequence to form double-stranded DNA sequences. The analyte can be selectively bound on the recognition surface [50]. The signal can come from an electro-active reporter that binds with single strand DNA, or an intercalator incorporated with double strand DNA [51-53].

1.2.2 Immunosensors

Antibody-based biosensors are also called immunosensors. Immunosensors are antibody-based affinity biosensors, where the detection of an analyte is achieved by its binding to a region of an antibody, such as sandwich type immunoassays, known as enzyme-linked immunosorbent assay (ELISA). Antibody-based sensors are an attractive alternative to the more conventional quantitative analytical methods such as chromatography (GC) and mass spectrometry (MS), because of their remarkably high specificity, small sample volumes, low detection limits, and reduced sample preparation [51]. However, the application is limited because the labeling process for antibodies is usually expensive, inconvenient, and time-consuming. Moreover, the process of antibody modification on a surface always has problems such as poor orientation and insufficient surface coverage. These problems can be overcome by complexing of the protein to nucleic acid, because nucleic acids can be easily modified with a variety of molecules [51-52]. Also, the modification process of the DNA sequence can be easily controlled by optimizing the self-assembled monolayer of thiolated DNA sequence [54].

1.2.3 Aptamers

Aptamers are defined as oligonucleic acid sequences which can recognize specific ligands and bind to diverse target molecules including ions or proteins. There are both RNA and DNA aptamers. The selection process of the aptamers sequences is called selection evolution of ligands by exponential enrichement (SELEX) [55]. Similar to antibodies and antigens, aptamers can bind to the target with high selectivity and affinity which can be competitive with antibodies. Aptamers also have several advantages such as accuracy, reproducibility, chemical stability, easier bio-activity treatment and reversible thermal denaturation.

1.2.4 SERS biosensors

The most widely used optical biosensor, including molecular Beacons, Taquman, and Scorpion probes, is based on fluorescence detection during PCR amplification [56-57]. Generally, fluorescence detection is easily accessible, and labels and many probes are commercially available. However, due to the high detection limits of fluorescence, a large number of PCR cycles are needed to generate sufficient targets, a time-consuming process. In addition, the multiplexing ability is limited by the use of optical filters to differentiate between fluorophores [51]. Moreover, background fluorescence can lead to decreased sensitivity due to the inefficient quenching of the fluorophore.

SERS or SERRS (surface enhanced resonant Raman spectroscopy) offers a very useful alternative technique with several important benefits. In this technique, a sharp fingerprint spectrum can be obtained, allowing discrimination between analytes in a mixture without separation. The technique tolerates a large range of colored molecules to be used as SERS reporters, including standard commercial fluorophores. It can also be widely used in DNA

probes, for example, the detection of a single-stranded DNA (ss-DNA), double-stranded DNA (ds-DNA) as well enzyme immunoassay.

Specific DNA sequences or individual DNA bases detection within a sequenced genome is significant to the assessment and diagnosis of specific illnesses. In recent years, a number of methods have been reported for detecting specific sequences of DNA. Typical SERRS based detection designs are shown in Figure 1.4. One general design is DNA hybridization detection with Raman reporter labeled with complementary target oligonucleotide as depicted in Figure 1.4 (a). In other designs, nanoparticle array substrate can be used in sandwich assay, and the signal can be directly detected from Raman label or it can be achieved by introduction of secondary nanoparticle conjugation as shown in Figure 1.4 (b).

1.2.5 SERRS Beacons

SERRS Beacon combines SERRS techniques with the fluorescence molecular Beacon concept to provide the option of using the two detections methods together. The principle of molecular Beacon was originally proposed by Tyagi S *et al*. A molecular Beacon is a single strand DNA sequence detained in a loop by a self-complementary stem. In the absence of the complementary DNA sequence, the molecular Beacon does not fluoresce, whereas after hybridization with the complementary sequence, fluorescence is released. Figure 1.4 (c) shows the principle behind the SERRS beacon approach. Similarly, SERRS Beacon is DNA sequence labeled with a Raman active reporter at one end. When the sequence is held in a loop structure, highly enhanced SERS signals are achieved, while after hybridization with the target sequence, the SERS signals are reduced. The difference between SERRS Beacon and molecular Beacon is that one is dependent on “signal off” detection and the other one relies on “signal on” detection.

Using the SERRS beacon concept, Musundi B. Wabuyele and Tuan Vo-Dinh *et al.* used plasmonics-based nanoprobes as "molecular sentinels" for DNA diagnostics (58-60). In their study, plasmonics nanoprobe or "molecular sentinel" (MS), were utilized to detect the gag gene sequence of the human immunodeficiency virus type 1 (HIV-1) successfully.

The color changes associated with DNA detection were detected visually on a reverse-phase silica plate, allowing for optimized detection of about 10 f M of an oligonucleotide [61-62, 111]. In 2002, the Mirkin group developed a method to use gold particles for DNA sequencing. In their study, Au particles were functionalized with Cy3-labeled oligonucleotides, which is complementary with part of the target DNA. When exposed to laser light, the nanoparticles became SERs active. Six different Raman active molecules were used as probes for six different DNA strands to reach a detection limit of 20 fM with the ability to simultaneous detect of the probes [67].

1.2.6 Electrochemical biosensors

Compared to other techniques, the electrochemical sensor has advantages such as low cost, simple instrument, high sensitivity, freedom from sample turbidity and ease of miniaturization for micro-fabrication assay [63]. These advantages give electrochemical sensors high potential and compatibility for implantable and portable hand-held products. In general, there are several methods that can be used to detect an electrochemical signal during a bio-recognition event, and these methods can be categorized as amperometric, potentiometric, impedance, and conductometric [63-64]. In the past decades, many research papers have been published about applications of electrochemical biosensors in various fields, especially in the clinical analysis area.

Electrochemical DNA sensors are based on the immobilization of a single-chain DNA strand onto an electrode and the measurement of changes in electrical readout caused by the hybridization. Biosensors utilizing aptamers as bio-recognition materials have been defined as "aptasensors." Much work has been published with thrombin aptamers. A thrombin binding aptamer is a 15 bases pair DNA sequence (GGT TGG TGT GGT TGG from 5' to 3') which can fold to a G-quartet conformation in the presence of thrombin. Generally, thrombin can be detected by different assays based on the thrombin binding aptamer. As shown in Figure 1.5 A) and B), one mode is thrombin binding aptamer based aptasensor using electrochemical methods. The other assay is based on molecular beacon fluorescence technique as shown in Figure 1.5 B) [105]. The principle of the aptasensor relies on the conformational change before and after the binding behavior. The conformational change can be measured electrochemically through changes in electron transfer from an attached re-dox reporter relatively near or far from an electrode surface. This field of research is progressing so rapidly that new achievements have appeared. One of the applications is the fabrication of DNA microarrays, which can be further used for multiplexing detection of different DNA targets.

1.2.7 Fabrication techniques of DNA biosensors

In a DNA biosensor design, immobilization of ssDNA onto the substrate or electrode surface plays an important role in the performance of the biosensors. Different types of DNA sequences can be used in different research, such as linear olignucleotides DNA (LO), hairpin olignucleotides DNA (HO), peptide nucleic acids (PNAs) [65] and locked nucleic acids (LNAs). The most commonly used DNA sequences are linear olignucleotides DNA, which exhibit high levels of specificity. Various approaches have been developed to immobilize the DNA probe to the solid surface of biosensors: (1) self-assembling monolayer (SAM) of thiolated

oligonucleotides on substrate or gold electrodes [66-67], (2) biotinylated DNA probes attached through Biotin-Streptavidin moiety reaction for protein detection, [68] (3) electro polymerization[69].

Self-assembled monolayer (SAM) of thiolated oligonucleotides is currently the most widely used approach through the reaction of the thiol group with the metal surface. The advantages of the SAMs are that they are well-ordered, and have strong covalent bond energy and van der Waals forces between the neighboring molecules. However, SAM systems have limitations such as low thermal stability. Moreover, the density of the probe DNA sequence on the surface can increase the charge repulsion of the sequence and affect the efficiency of hybridization with target sequence [66A]. The modification of the SAM on the surface needs precise control so that optimal DNA probe density and probe orientation can be realized. For example, a two-step immobilization approach is currently extensively used in the research. The attractive method consists of the simultaneous co-immobilization of the thiolated DNA probe with another thiolated molecule called “backfiller” such as mercaptohexanol (MCH). Schematic illustration of the co-immobilization approach is shown in Figure 1.6 [66B]. The process includes thiolated DNA immobilization, passivation layer co-immobilization and hybridization process of DNA probe and target.

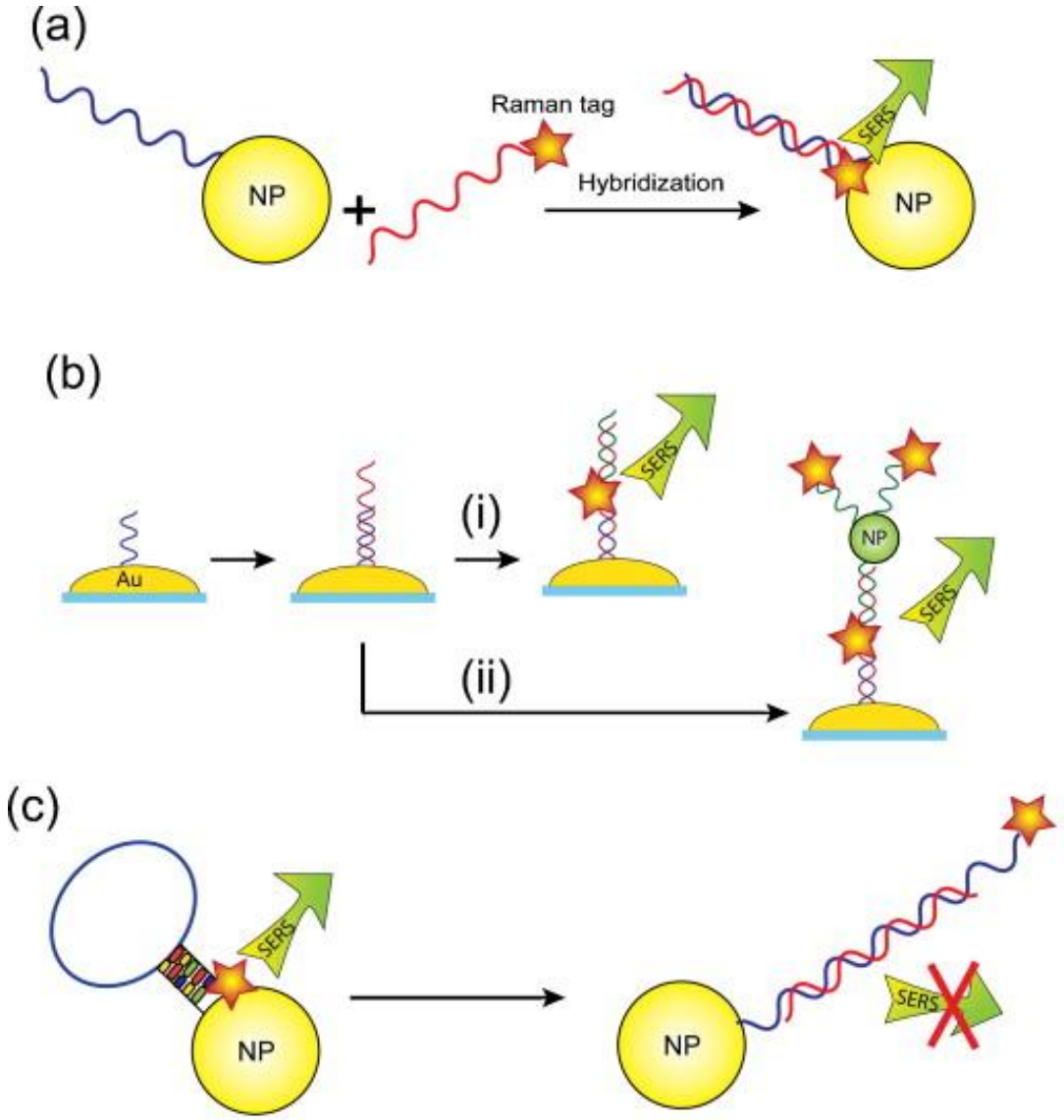

Figure 1.4 SERRS based DNA or protein detection designs. (a) DNA hybridization detection with Raman tag labeled complementary target DNA. (b) Au nanosphere substrate used with sandwich assay with direct readout (i) and (ii) amplification of SERs signal using nanoparticle. (c) SERRS molecular Beacon design. Taken from Ref 104 with permission.

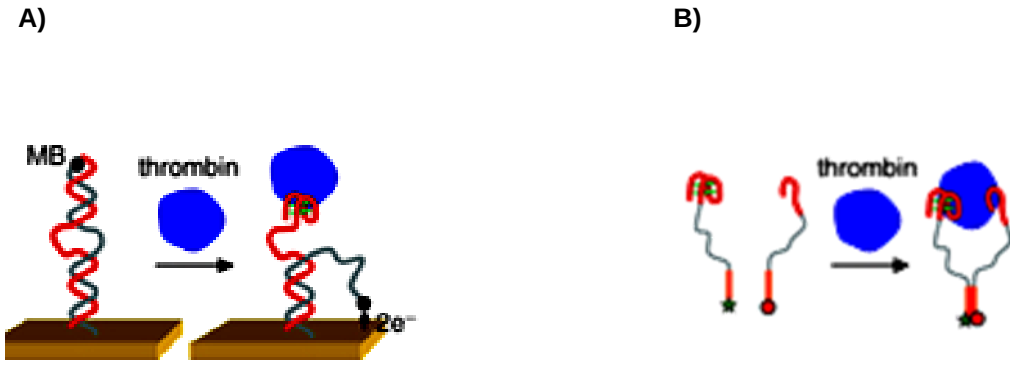

Figure 1.5 Thrombin aptasensor based on conformational change from aptamer target interactions. A) Thrombin binding aptamer based electrochemical biosensors (MB attached as the redox reporter). B) Thrombin molecular beacon fluorescence technique. Taken from Ref 105 with permission.

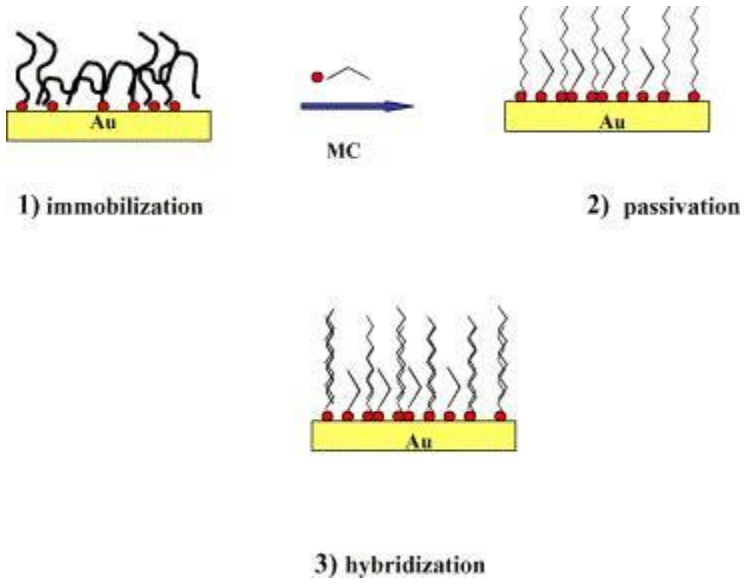

Figure 1.6 Schematic illustration of the co-immobilization approach: immobilization of thiolated DNA, co-immobilization of mercaptohexnol (MC) passivation layer and hybridization with target DNA sequence. Taken with permission from Ref 66.

1.3 Introduction to types of energy storage devices nowadays

The energy crisis has been a severe problem threatening every existence and development of human civilization. Currently, people are driven to find more sustainable and renewable and environmentally friend resources. Among them, production of electrochemical energy is under serious concern as an alternative energy source [77-78]. Electric double layer capacitors (EDLCs), also acknowledged as supercapacitors, have received increased attention because they can offer better power performance and provide superior energy density than conventional battery and capacitors [74-76].

Principally, there are some major differences between batteries, fuel cells and electrochemical capacitors. On one hand, energy stored in a battery is released from chemical re-dox reactions and converted to electricity; however, electrical energy is generated by physically charging from an outside electric source. On the other hand, the principle of the energy storage and release from electrochemical capacitor is due to electrical double layers (EDLs) [79, 80]. A wide variety of different electrode materials and electrolytes are currently being manipulated to improve the efficiency and practicality of EDLCs. In the following sections, three types of capacitors and the development of related materials will be reviewed and described based on recent publications.

1.3.1 Introduction of supercapacitors

Supercapacitors are also called ultracapacitors because of their higher capacitance values than conventional capacitors currently accessible. The energy storage of supercapacitors is based on the charge storage in the electrical double layer (EDL) of a high surface area electrode [80].

Until now, millions of dollars per year are spent on the study and development of supercapacitors, including potential application in portable electronic devices and PCs, low CO_2 emission hybrid cars and other vehicles [81]. Basically, supercapacitors can be generally divided into three categories based on the energy storage mechanism: EDLc, pseudocapacitors, and hybrid capacitors [82]. Faradaic processes include charge transfer process via redox reactions. During non-Faradaic mechanism process, charges are dispersed on surfaces by physical forces without electron charge transfer. Supercapacitors and pseudocapacitors rely on the non-Faradaic process, and faradaic process respectively. Hybrid capacitor is based on both processes.

Ragone plot is widely used to compare the performance between different types of energy storage system as shown in Figure 1.7. Compared with batteries and fuel cells, electric capacitors have much more specific power or power density. Other benefits of supercapacitor also include long reusability, more environmental and eco-friendly, harmless, and light weight. Cycle life and stability of supercapacitors can easily exceed 10^6 cycles, much better than battery electrodes [80]. Those advantages offer supercapacitors as a promising alternative power source for electrical vehicles, digital telecommunication kits, uninterruptible power supply for PCs and other devices particularly under the non-serviceable condition. [83].

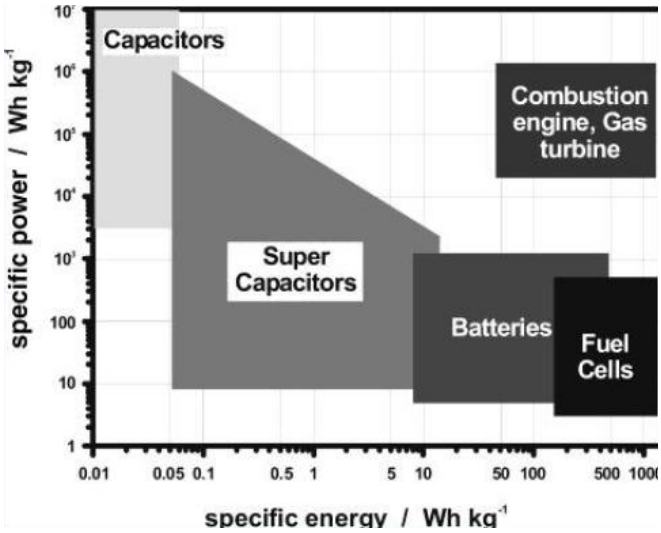

Figure 1.7 Ragone chart of the energy storage comparison. Taken from Ref 106 with permission.

Property	Battery	Electrochemical capacitor
Storage mechanism	Chemical	Physical
Power limitation	Reaction kinetics, mass transport	Electrolyte conductivity
Energy storage	High	Limited
Charge rate	Kinetically limited	High, same as discharge rate
Cycle life	Mechanical stability, chemical reversibility	Side reactions

Table 1.1 Comparison of battery and electrochemical capacitors. Taken from Ref 106 with permission.

1.3.2 Electrical Double Layer capacitors

The concept of the double layer was originally proposed and modeled by Hermann von Helmholtz when he was investigating the charge distribution with nanoparticle suspensions [84]. Later, this concept was found to be well applied to the surface of metal electrodes [85]. As mentioned earlier, electrochemical double-layer capacitors (EDLCs) store and release the energy through a non-faradaic process, without electron transfer between electrode surface and molecules.

When an electrode is immersed into an electrolyte solution, there is a spontaneous organization of charges at the surface of the electrode and in the electrolyte facing the electrode as shown in Figure 1.8. This organization of charges is known as electrical double layer. When an outer voltage is applied, negative charges and positive charges will accumulate on the electrode surfaces. According to the Helmholtz model, electrochemical double-layers are formed on the electrodes and electrolyte surface, called Helmholtz double-layers. The outer Helmholtz plane (OHP) refers to the distance of closest approach of nonspecifically solvated cation in solution, while the inner Helmholtz plane (IHP) refers to the distance of closest approach of specifically adsorbed ions to the metal electrode surface. They are represented by x_1 and x_2 in the Figure 1.8. In practice, the structure of the EDL is much more complicated than the models discussed above. Helmholtz model is the earliest simplest model to explain the double layers. By introducing a diffusion layer model, Gouy-Chapman is established. However, the combination of the two models is most widely used for the theoretical studies.

Carbon materials have the characterizations of high surface area, low cost and more established fabrication techniques. Thus, they are the primary choice for fabrication of electrode

materials. There are diverse types of carbon materials that can be utilized as the EDLCs electrodes. Generally they are activated carbons, carbon aerogels, and carbon nanotubes [86-91, 112].

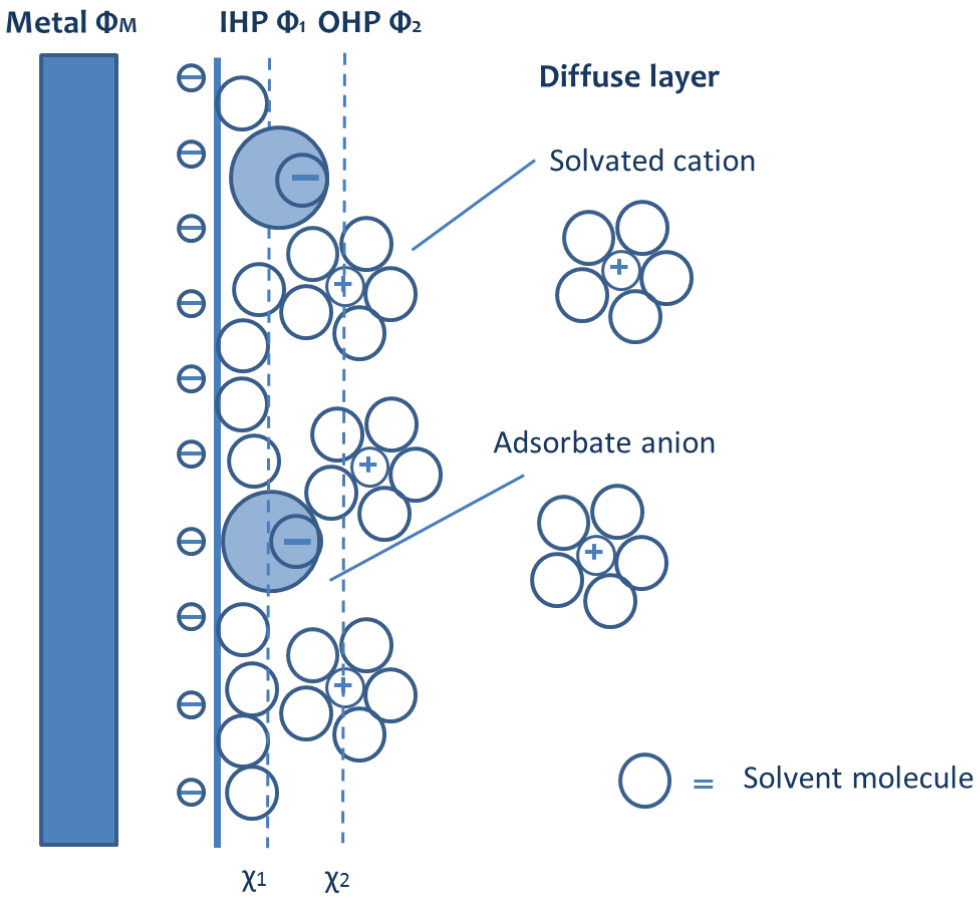

Figure 1.8 Model of Electrical Double Layer (EDLCs). In this model, Φ represents electrostatic potential.

1.3.3 Pseudocapacitors

Pseudocapacitors store energy by electron charge transfer between electrode surface and electrolyte. The charge storage attainable by this mechanism is approximately one order of magnitude higher than for the EDL mechanism. Unlike EDLCs, a pseudocapacitor involves a charge transfer process at the electrode surface. This can be caused through different chemical reactions such as electro-sorption, re-dox reactions and chemical intercalations. These Faradaic charge transfers may improve the capacitance and energy densities. However, the chemical process can also lead pseudocapacitors to "fading problem," and loss of capacity through repeated charging and discharging cycles. So compared to EDLCs, the lifetime of pseudocapacitors is usually shorter.

Typically, materials such as conducting polymers and metal oxides are used to store energy in pseudocapacitors [90-92].Typical metal oxide materials are transition metal oxides, which have multiple oxidation and reduction processes. Among the various metal oxides materials, ruthenium dioxide has been reported to show a remarkably high capacitance [93]. However, the commercial applications of ruthenium are limited because of its low abundance, high cost and toxicity. Manganese dioxide, MnO_2 or Mn_3O_4 is one of the alternative materials with favorable properties such as high specific capacitance, high power density, low cost and environmental compatibility [94-95].

1.3.4 Hybrid supercapacitors

Hybrid supercapacitors have attracted much attention recently because they combine the advantages of EDLCs and pseudocapacitors to have better performance characteristics. The energy storage of a hybrid supercapacitor involves both Faradaic and non-Faradaic processes. Higher energy and power densities with cycling stability and affordability can be achieved when

compared with supercapacitors. Recent research has focused on three different types of hybrid composite materials: (1) combination of carbon materials with conducting polymer, (2) metal oxide, and (3) incorporation of both. On one hand, the carbon-based materials have a high surface area that improves the contact between the solution and deposition [93]. On the other hand, the pseudocapacitive deposition is enabled to further improve the capacitance through the electron charge transfer process. One example is Graphene/Mn_3O_4 composite materials, which are prepared by a simple hydrothermal synthesis process [95]. The hybrid materials have a higher capacitance and higher power density than Mn_3O_4 nanorods dispersion. The capacitance of the hybrids was 100% retained after 10^4 cycles at a charging current of 5 A/g.

1.3.5 Supercapacitor materials developments

The development of electrochemical capacitors is combined with seeking optimal electrode materials that can accumulate electrical energy efficiently with a long durability. The key to obtaining a high capacitance charging double layer is to use materials with high surface area and electronically conducting electrodes. There are mainly three different electrode materials for supercapacitors: conducting polymers, related carbon materials and transition metal oxides or metal hydroxides [96-98].

More materials with high surface active area were studied by various research groups. Among them, carbon-based materials, such as grapheme, activated carbon, mesoporous carbon, CNT, and carbon fibers are used as electrode active materials, as summarized in Figure 1.9. Activated carbons are widely used due to their moderate cost [89-91]. Metal oxides such as MnO_2, Mn_3O_4, V_2O_5, and RuO_2 are widely used and developed for pseudocapacitors. [95-96] Conducting polymers, such as polythiophene, polypyrrole (PPY), polyaniline, and their

derivatives for example Poly 3,4-ethylenedioxythiophene (PEDOT), are used as an alternative as well [98-101].

Carbon material can provide a long life cycle and high power density but its low specific capacitance restricts applications for devices that require high energy density. On the contrary, conducting polymer materials can achieve high capacitance, good conductivity and low cost but they have relatively low stability and short life cycle. In addition to the advantage of DL capacitance, transition metal oxides and hydroxides involve the pseudocapacitance process and have a large charge/discharge potential range, but they have small surface area and shorter life cycle. The combination of these unique advantages of various nano-scale capacitive materials to form hybrid materials is a significant method to control, develop and optimize the structures and properties of electrode materials, whose performance is greatly enhanced for supercapacitors. Both the individual components of the hybrid materials and their morphology and interfacial characteristics can affect the supercapacitor's performance. Recently, much research has been focused on the fabrication of hybrid materials, such as conducting polymers mixed with metal oxides or carbon nanotubes, and graphene mixed with metal oxides or conducting polymers [89, 99, 100].

Although major improvements have been accomplished to fabricate nano-composite materials, there are still many challenges to be overcome. Many factors need be considered for the design and fabrication route of nanocomposite materials such as synthesis methods, fabrication process, interfacial characteristics, and nanocrystallite size.

Materials	**Specific surface area /m^2g^{-1}**	**Density/g cm^{-3}**	**Aqueous electrolyte**	
			/F g^{-1}	**/F cm^{-3}**
Carbon materials:				
Activated carbons	1000-3500	0.4-0.7	<200	<80
Functionalized porous carbons	300-2200	0.5-0.9	150-300	<180
Carbon nanotube (CNT)	120-500	0.6	50-100	<60
Activated carbon fibers	1000-3000	0.3-0.8	120-470	<150
Carbon aerogels	400-1000	0.5-0.7	100-125	<80
Carbon composite material:				
CNT-MnO_2	234	1.5	199	300
AC-polyaniline	1000	-----	300	----

Table 1.2 Properties and characteristic of various carbon materials. Reprinted from Ref 107.

References

[1] Fleischmann, M.; Hendra, P. J.; McQuillan; A. J. *Chem. Phys. Lett.***1974**, *26*, 163.

[2] Jeanmaire, D. L.; Van Duyne, R. P. *J. Electroanal. Chem.* **1977**, *84*, 1.

[3] Albrecht, M. G.; Creighton, J. A. *J. Am. Chem. Soc.***1977**, *99*, 5215.

[4] Driskell, J. D.; Kwarta, K. M.; Lipert, R. J.; Porter, M. D. *Anal. Chem.* **2005**, *77*, 6147.

[5] Braun, G.; Lee, S. J.; Dante, M.; Nguyen T.; Moskovits, M.; Reich, N. *J. Am. Chem. Soc.* **2007**, *129*, 6378.

[6] Haynes, C. L.; McFarland, A. D.; Van Duyne, R. P. *Anal. Chem.* **2005**, *77*, 338A.

[7] Haes, A. J.; Haynes, C. L.; McFarland, A. D.; Zou, S.; Schatz, G. C.; Van Duyne, R. P. *MRS Bull.* **2005**, *30*, 368.

[8] Yonzon, C. R.; Young, M. A. J.; Zhang, Y. X.; Van Duyne, R. P. *Farad. Discuss.* **2006**, *132*, 9.

[9] Hao, E.; Schatz, G. C. *J. Chem. Phys.* **2004**, *120*, 357.

[10] Haynes, C. L. *Anal. Chem.* **2008**, *80*, 3431.

[11] Campion, A.; Kambhampati, P. *Chem. Soc. Rev.* **1998**, *27*, 241.

[12] Campion, A. *J. Chem. SOC., Faraday Trans.* **1996**, *92*, 4775.

[13] Stiles, P. L.; Dieringer, J. A. N.; Shah, C.; Van Duyne, R. P. *Annu. Rev. Anal. Chem.* **2008**, *1*, 601.

[14] Haynes, C.L.; Van Duyne, R.P. *J. Phys. Chem. B*, **2001**, *105*, 5599.

[15] Haynes, C. L.; McFarland, A. D. Van Duyne, R. P. *Anal. Chem.* **2005**, *77 1*, 338 A.

[16] Qin, L.; Zou, S.; Xue, C.; Atkinson, A.; Schatz, G. C.; Mirkin, C. A. *Proc. Natl. Acad. Sci. USA.* **2006**, *103*, 13300.

[17] Sun, Y.; Xia, Y. *Science* **2002**, *298*, 2176.

[18] Wiley, B.; Sun, Y.; Mayers, B.; Xia, Y.; *Chem. Eur.* **2005**, *11*, 454.

[19] Jin, R.; Cao Y. C.; Hao, E.; Metraux, G. S.; Schatz, G. C.; Mirkin, C. A. *Nature* **2003**, *425*, 487.

[20] Leverette, C. L.; Jacobs, S. A.; Shanmukh, S.; Chaney, S. B.; Dluhy, R. A.; Zhao, Y. P.; *Appl. Spectrosc.* **2006**, *60*, 906.

[21] Zhang, J.; Gao, A.; Alvarez-Puebla, R. A.; Buriak, J. M.; Fenniri, H.; *Adv. Mater*, **2006**, *18*, 3233.

[22] Jeanmaire, D. L.; Van Duyne, R. P. *J. Electroanal. Chem*. **1977**, *84*, 1.

[23] Wang, Z.; Rothberg, L. J. *Appl. Phys. B.* **2006**, *84*, 289.

[24] Haynes, C. L.; McFarland, A. D.; Zhao, L.; Van Duyne, R. P.; Schatz, G. C.; Gunnarsson, L.; Prikulis, J.; Kasemo, B.; Kall, M.; *J. Phys. Chem. B.* **2003**, *107*, 7337.

[25] Lee, P. C.; Meisel, D. J.; *J. Phys. Chem*. **1982**, *86*, 3391.

[26] Steinbrück, A.; Csaki, A.; Festag, G.; Fritzsche, W. *Plasmonics* **2006**, *1*, 79.

[27] Yao, J. L.; Pan, G. P.; Xue, K. H.; Wu, D. Y. B.; Ren, D. M.; Sun, J.; Tang, X.; Tian, Z. Q. *Pure Appl. Chem*. **2000**, *72*, 221.

[28] Lee, S. J.; Morrill, A. R.; Moskovits, M. *J. Am. Chem. Soc*. **2006**, *128*, 2200.

[29] Kahl, M.; Voges, E.; Hill, W.; *Spectrosc. Eur*. **1998**, *10*, 8.

[30] Haynes, C. L.; McFarland, A. D.; Zhao, L.; Van Duyne, R. P.; Schatz, G. C.; Gunnarsson. L.; Prikulis, J.; Kasemo, B.; Kall, M. *J. Phys. Chem. B* **2003**, *107*, 7337.

[31] Whitney, A. V.; Elam, J. W.; Zou, S.; Zinovev, A. V.; Stair, P. C.; Schatz, G. C.; Van Duyne, R. P. *J. Phys. Chem.* **2005**, *109*, 20522.

[32] Fischer, U. C.; Zingsheim, H. P. *J. Vac. Sci. Technol.* **1981**, *19*, 881.

[33] Hulteen, J. C.; Van Duyne, R. P. *J. Vac. Sci. Technol.* **1995**, *A13*, 1553.

[34] Thevenot, D. R.; Tóth, K.; Durst, R. A.; Wilson, G. S. *Pure Appl. Chem*. **1999**, *71* , 2333.

[35] Wang, J. *Analytical Electrochemistry*, John Wiley & Sons VCH, Hoboken, NJ, USA, **2006**.

[36] Kang, Y.; Feng, K. J.; Chen, J. W.; Jiang, J. H.; Shen, G. L.; Yu, R. Q. *Bioelectrochemistry* **2008**, *73*, 76.

[37] Millan, K. M.; Saraullo, S.; Mikkelsen, S. R. *Anal. Chem.* **1994**, *66*, 2943.

[38] Piunno, P. A.; Krull, U. J.; Hudson, R. H.; Damha, M. J.; Cohen, H. *Anal. Chim. Acta.* **1994**, *288*, 205.

[39] Minunni, M.; Tombelli, S.; Scielzi, R.; Mannelli, I.; Mascini, M.; Gaudiano, C. *Anal. Chim. Acta*. **2003**, *48*, 55.

[40] Sawata, S.; Kai, E.; Ikebukuro, K.; Iida, T.; Honda, T.; Karube, I. *Biosens. Bioelectron.* **1999**, *14*, 397.

[41] Kelley, S. O.; Boon, E. M.; Barton, J. K.; Jackson, N. M.; Hill, M. G. *Nucleic Acids Res.* **1999**, *27*, 4830.

[42] Thiel, A. J.; Frutos, A. G.; Jordan, C. E.; Corn, R.M.; Smith, L. M. *Anal. Chem.* **1997**, *69*, 4948.

[43] Mori, T.; Maeda, T. *Polym. J.* **2002**, *34*, 624.

[44] Wang, J.; Polsky, R.; Xu, D. *Langmuir* **2001**, *17*, 5739.

[45] Wang, J.; Polsky, R.; Merkoci, A.; Turner, K. L. *Langmuir* **2003**, *19*, 989.

[46] Wang, J. *Anal. Chim. Acta.* **2002**, *288*, 205.

[47] Gooding, J. *J. Electroanalysi.* **2002**, *14*, 1149.

[48] Kimmel, D. W.; LeBlanc, G.; Meschievitz, M. E.; Cliffel, D. E. *Anal. Chem.* **2012**, *84*, 685.

[49] Ispas, C. R.; crivat, g.; Andreescu, S. *Anal. Lett.* **2012**, *45*, 168.

[50] Chen, S.; Yuan, R.; Chai, Y.; Xu, Y.; Min, L.; Li, N. *Sens. Actuators* **2008**, *135*, 236.

[51] Corry, B.; Uilk, J.; Crawley, C. *Anal. Chim. Acta.* **2003**, *496*, 103.

[52] Pampalakis, G.; Kelley, S. O. *Analys.* **2009**, *134*, 447.

[53] Ye, Y. K.; Zhao, J. H.; Yan, F.; Zhu, Y. L.; Ju, H. X. *Biosens. Bioelectron.* **2003**, *1*, 1501.

[54] Chaubey, A.; Malhotra, B. D. *Biosens. Bioelectron.* **2002**, *17*, 441.

[55] Blanco-Lopez, M. C.; Lobo-Catanon, M. J.; Miranda-Ordieres, A. J.; Tunon-Blanco, P. *Trends Anal. Chem.* **2004**, *23*, 36.

[56] Dou, X.; Takama, T.; Yamaguchi, Y.; Harai, K.; Yamamoto, H.; Doi, S.; Ozaki, Y. *Appl. Opt.* **1998**, *37*, 759.

[57] Millot, J. M. *Anal. Chem*. **2003**, *75*, 4305.

[58]Wang, J.; Ozsoz, M.; Cai, X.; Rivas, G.; Shiraishi, H.; Grant, D. H.; Chicharro, M.; Fernandes, J.; Palecek, E. *Bioelectrochem. Bioenerg.* **1998**, *45*, 33.

[59] Balamurugan, S.; Obubuafo, A.; Soper, S. A.; Spivak, D. A. *Anal. Bioana. Chem.* **2008**, *390*, 1009.

[60] Khan, H.; Missailidis, S. *Gene. Ther. Mol. Biol*. **2008**, *12*, 111.

[61] Tyagi, S.; Kramer, F. R. *Nat. Biotechnol*. **1996**, *14*, 303.

[62] Whitcombe, D.; Theaker, J.; Guy, S. P.; Brown, T. Little, S. *Nat. Biotechnol*. **1999**, *17*, 804.

[63] Wabuyele, M. B.; Vo-Dinh, T. *Anal. Chem*. **2005**, *77*, 7810.

[64] Vo-Dinh, T.; Yan, Fei.; Wabuyele, M. B. *J. Raman. Spectrosc.* **2005**, *36*, 640.

[65] Kneipp, K.; Kneipp, H.; Itzkan, I.; Dasari, R. R.; Feld, M. S. *Chem. Rev.* **1999**, *99*, 2957.

[66] Gearheart, L. A.; Ploehn, H. J.; Murphy, C. J. *J. Phys. Chem. B.* **2001**, *105*, 12609.

[67] Wei, Y.; Cao, C.; Jin, R.; Mirkin, C. A. *Science* **2002**, *1536*, 297.

[68] Chaubey, A.; Malhotra, B. D. *Biosens. Bioelectron.* **2002**, *17*, 441.

[69] Blanco-Lopez, M. C.; Lobo-Catanon, M. J.; Miranda-Ordieres, A. J.; Tunon-Blanco, P. *Trends Anal. Chem.* **2004**, *23*, 36.

[70] Wang, J.; Palecek, E.; Nielsen, P.; Rivas, G.; Cai, X.; Shiraishi, H.; Dontha, N.; Luo, D.; Farias, P. *J. Am. Chem. Soc.* **1996**, *118* , 7667.

[71] Herne, T.; Tarlov, M. *J. Am. Chem. Soc.* **1997**, *119*, 8916.

[72] Levicky, R.; Herne, T.; Tatlov, M.; Satija,S. *J. Am. Chem. Soc*. **1998**, *120*, 9787.

[73] Ebersole, R.; Miller, J.; Moran, J.; Ward, M. *J. Am. Chem. Soc.***1990**, *112*, 3239.

[74] Simon, P.; Gogots, Y. *Nature Mater.* **2008**, *7*, 845.

[75] Miller, J. R.; Simon, P. *Science* **2008**, *321*, 1.

[76] Arbizzani, C.; M. Mastragostino. *J. Power Sources*, **2001**, *100*, 164.

[77] Armand, M.; Tarascon, J. M. *Nature* **2008**, *451*, 652.

[78] Bard, A. J.; Faulkner, L. R. *Electrochemical Methods: Fundamentals and Applications.* 2nd edition, **2001**

[79] Kotz, R.; Carlen, M. *Electrochim. Acta.* **2000**, *45*, 2483.

[80] Miller, J. R.; Simon, P. *Science* **2008**, *321*, 651.

[81] Conway, B. E. *New York, Kluwer-Plenum*. **1999**

[82] Burke, A. *J. Power Sources* **2000**, *91*, 37.

[83] Chu, A.; P. Braatz. *J. Power Sources* **2002**, *112*, 236.

[84] Miller, J. R.; Burke, A. *Electrochem. Soc. Interf*. **2008**, *17*, 53.

[85] Pandolfo, A. G.; Hollenkamp, A. F. *J. power sources*, **2006**, *157*, 11.

[86] Gogotsi, Y. *Carbon Nanomaterials*, CRC Press, Boca Raton **2006**, 56

[87] Futaba, D. N.; Hata, K.; Yamada, T.; Hiraoka, Tatsuki.; Hayamizu, Y.; Kakudate, Y.; Tanaike, O.; Hatori, H.; Yumura, M.; Iijima, S. *Nature Mater*. **2006**, *5*, 987.

[88] Portet, C.; Chmiola, J.; Gogotsi, Y.; Park, S.; Lian, K. *Electrochim. Acta*, **2008**, *53*, 7675.

[89] Niu, C.; Sichel, E. K.; Hoch, R.; Moy, D.; Tennent, H. *Appl. Phys. Lett*. **1997**, *70*, 1480.

[90] Gamby, J.; Taberna, P. L.; Simon, P.; Fauvarque, J. F.; Chesneau, M. *J. Power Sources* **2001**, *101*, 109.

[91] Moseley, P.T.; Nelson, R.F.; Hollenkamp, A.F. *J. Power Sources* **2006**, *157*, 11.

[92] Naoi, K.; Simon, P. *Electrochem. Soc. Interf.* **2008**, *17*, 34.

[93] Kim, I. H.; Kim, K. B. *Electrochem. Solid St.* **2001**, *4*, A62.

[94] Yu, G.; Hu, L.; Vosgueritchian, M.; Wang, H.; Xie, X.; McDonough, J. R.; Cui, Xu.; Cui,Yi.; Bao, Z. *Nano Lett*. **2011**, *11*, 2905.

[95] An, G.; Yu, Ping,; Xiao, M.; Liu, Z.; Miao, Z.; Ding, K.; Mao, L. *Nanotechnology*. **2008**, *19*, 275709.

[96] Zheng, J. P.; P. J. Cygan.; Jow, T. R. *J. Electrochem. Soc*. **1995**, *142*, 2699.

[97] Jurewicz, K.; Delpeux, S.; Bertagna, V.; Beguin, F.; Frackowiak, E. *Chem. Phys. Lett*, **2001**, *347*, 36.

[98] Lu, W.; Hartman, R. *J. Phys. Chem. Lett.* **2011**, *2*, 655.

[99] Rudge, A.; Davey, J.; Raistrick, I.; Gottesfeld, S.; Ferraris, J. *J. Power Sources* **1994**, *47*, 89.

[100] Fusalba, F.; Gouerec, P.; Villers, D.; Belanger, D. *J. Electrochem. Soc*. **2001**, *148*, A1.

[101] Frackowiak, E.; Khomenko, V.; Jurewicz, K.; Lota, K.; Beguin, F. *J. Power Sources* **2006**, 153, 413.

[102] Yonzon, C. R.; Stuart, D. A.; Zhang, X.; McFarland, A. D.; Haynes, C. L.; Van Duyne, R. P. *Talanta* **2005**, *65*, 438.

[103] Baker, G. A. *Anal. Bioanal.Chem.* **2005**. *382*, 1751.

[104] Petryayeva, E.; Krull, U. J. *Anal. Chim. Acta*.**2011**, *706*, 8.

[105] Gu, L. *Nanopores*. Springer-Verlag, New York, **2011**. *51*.

[106] Whittingham, M. S.; Savinell, R. F.; Zawodzinski, T.; Zawodzinski, T. *Chem. Rev.* **2004**, *104*, 4247.

[107] Zhang, L.; Zhao, X. S. *Chem. Soc. Rev.* **2009**, *38*, 2520.

[108] Hao, E.; Schatz, G. C. *J. Chem. Phys*. **2004**, *120*, 357.

[109] Jin, R.; Cao, Y. W.; Mirkin, C. A. *Science*, **2001**, *294*, 1901.

[110] Xu, H. *Appl. Phys. Lett*. **2004**, *85*, 5980.

[111] Rella, R.; Spadavecchia, J.; Manera, M.G.; Siciliano, P.; Santino, A.; Mita, G. *Biosens. Bioelectron.* **2004**, *20*, 1140.

[112] An, K. H.; Jeon, K. K.; Heo, J.K.; Lim, S.C.; Bae, D.J.; Lee, Y.H. *J. Electrochem. Soc*. **2002**, *149*, A1058.

Chapter 2

Optimization of Ag/Au film over nanoshpere SERS active substrates for biosensor applications

2.1 Introduction

As mentioned in Chapter 1, the sensitivity of the SERS technique is comparable to that obtained by fluorescence spectroscopy (FS) [1–3]. With the development of SERS substrates, enhancements of Raman signals by a factor of 10^6 to 10^{16} can be obtained [5–7]. The enhancement mechanisms in SERS are based on the chemical mechanism and EM field enhancement due to LSPR (Localized surface Plasmon resonance). Therefore, SERS can reach the appropriate sensitivity for ultra-trace level and even single-molecule (SM) detection [3, 4, 8].

For an ideal substrate, there are several requirements, especially in biosensor applications [9]. First, the substrate must have high SERS activity and sensitivity. By controlling the size and inter-particle spacing, the LSPR frequency of the substrate can be tuned to match the incident laser frequency to maximize the enhancement. This technique is called surface enhanced resonance Raman scattering (SERRS). Second, the substrate must be uniform so that the deviation in enhancement over the entire surface is less than 20%, which involves a relatively ordered arrangement of the nanoparticles on the substrate. Third, the substrate must have excellent stability and reproducibility. Even after a long shelf time, the enhancement effect still must be maintained. The aberration in the enhancement should be less than 20% for different pieces of substrates prepared by the same method.

Various methods have been developed to prepare active SERS substrates. A large portion of SERS research has utilized colloidal Au or Ag nanoparticles or roughened metal surfaces [10, 11]. Although high enhancement factors have been achieved for those substrates, tenability and reproducibility have remained a challenge for biosensor applications. To overcome these problems, several techniques, such as fabricating nanospheres, nano-gaps, and even nano-shells, have been developed [12-15]. Among them, the nanosphere lithography method developed by the Van Duyne group [16] and the Bartlett group [17] showed great potential for the preparation of the active substrate. The advantage of the nanosphere lithography method is that the shape, size, and spacing of the nanostructures can be controlled by changing the size of the nanospheres and the thickness of the deposited metal, thereby adjusting the position of the LSPR to match the excitation wavelength and to optimize the SERS enhancement [18]. However, the success rate of this approach really depends on the experience of the scientists and how accurately the experiment can be controlled; therefore, it is still a challenge to obtain an ordered surface without any defects.

In this chapter, a substrate fabrication method based on the film over nano-sphere (FON) technique is optimized and utilized for biosensor applications. In addition, by using the self-assembled monolayer of alkanethiol, the distance dependence on the phenomenon of surface-enhanced Raman scattering is investigated.

2.2 Experimental

2.2.1 Chemicals

All the chemicals used were reagent grade or better. Both 4-aminothiophenol (4-ATP) and thiol chemicals were purchased from Aldrich. Thiol chemicals involved mercaptohexanol (C6), mercaptooctanol (C8), mercaptoundecanol (C10), and mercapto octadecanol (C18).

Polystyrene nanosphere latex was obtained from Invitrogen Company. Two kinds of polystyrene nanosphere were used in the experiments with diameter of 300 nm and 600 nm, respectively. Piranha solution (3:1 concentrated H_2SO_4: 30% H_2O_2) and 5:1:1 H_2O: NH_4OH: 30%H_2O_2 solution were used for the glass surface treatment. Caution: Piranha solution is extremely corrosive and must be handled with care.

2.2.2 SERS substrate fabrication

In this study, the film over nanosphere technique was used to prepare the substrate according to the method of Van Duyne[16]. Glass cover slides were first cleaved to an area about 1 cm^2 and then cleaned by immersion in piranha solution (3:1 concentrated H_2SO_4: 30% H_2O_2) at approximately 80 °C for 1 h. After cooling down, the substrates were rinsed thoroughly with distilled water and then soaked in 5:1:1 H_2O: NH_4OH: 30%H_2O_2 solution for 60 min. The glass substrates were rinsed repeatedly with D.I. water and then used immediately. The polystyrene nanospheres suspension was diluted to 4 wt% (w/v) solution in distilled water. Then 10 μL of diluted suspension was spin coated at around 500-1000 rpm on the pre-treated glass to form a polystyrene nanosphere monolayer. After air drying overnight, the nanosphere film was sputter coated with layers of silver and gold. The sputter coating was carried out in a vacuum chamber by PELCO SC-7 sputter coater (Ted Pella Inc). The operation settings were 0.09 mbar of the vacuum chamber under the Argon gas situation, with 70 mm working distance between the metal target and the substrate, 25 mA of sputtering current, and 360 seconds of the sputtering time. Under the optimized condition, the thickness of the gold and silver produced was 145 nm, measured by Veeco Dektak prolifier instrumentation.

2.2.3 SERS instrument

SERS spectra were measured by Raman instrumentation (Renishaw InVia) with a 514.5nm green laser and a 50× long working distance objective lens. The scattered light was first passed through a holographic notch filter to get rid of the Rayleigh scattering and then dispersed onto a charge-coupled device (CCD) detector. The spectrum accumulation time is 20 seconds with five accumulations under laser power 25mW.

2.3 Results and discussion

Film over nanosphere substrate optimization

Experiments were performed to optimize the Ag/Au FONs in order to achieve strongest SERS. Silver and gold metal thin films with a deposition time ratio of 1:1 and total thickness about 145 nm were found to be optimum. Figure 2.1 shows the SEM image of the prepared SERS substrate. It demonstrates that Ag/Au substrate is mostly uniform. Experimental treatments were performed extremely carefully because the substrate can become unstable due to extensive treatments and exposure time because of the weakness of the bond between silver and gold and the glass. A self-assembled monolayer of 4-aminothiophenol (4-ATP) was used as the Raman probe molecule for the following experiments. The chemical structure and the Raman peak assignments are shown in Table 2.1.

Figure 2.2 demonstrates the stability of the FONs. First, the freshly prepared substrate was immobilized in 1mM 4-aminothiophenol solution, and self-assembled monolayer of 4-aminothiophenol were formed on the surface. After that, substrate was washed thoroughly and incubated in D.I. water from 1 hour to 12 hours. As depicted in Figure 2.2, the substrate remains stable within the time scale. The freshly prepared substrate with different sputtering coating times and different ratios of Au and Ag thickness were incubated in the 1 mM 4-ATP in ethanol

solution for 20 minutes. Then the substrate was washed three times with ethanol to remove the non-specific 4-ATP on the surface. Finally, the substrate was dried in air room temperature before Raman measurements. Based on the previous studies, 300 nm nanosphere was selected for the substrate fabrication under the laser excitation wavelength at 514 nm, while 600 nm nanosphere was found more suitable for substrate fabrication for the 785 nm laser.

Because the total thickness of the metal layer on the surface can affect the Raman enhancement, the total thickness was optimized by changing the sputtering coating time with 60 seconds, 180 seconds, 360 seconds, 420 seconds, and 720 seconds. The corresponding thicknesses are 24nm, 72nm, 145nm, 168nm and 308nm respectively, measured by Veeco Dektak prolifier instrumentation. Clearly, as shown in Figure 2.3, with an increase in the sputter-coating time, Raman intensity tends to increase for a time period up to 360 seconds. The highest Raman signal is therefore achieved when the deposition time equals 360 seconds. The thickness of the gold and silver thin film deposited was 145nm.

In addition, the ratio of Au/Ag deposition thickness can affect the Raman enhancement because it affects the surface characterization. For the sputter-coating system, a linear relationship is expected between the deposition time and the thickness of the metal films. Deposition time ratio of gold to silver layer was tuned to achieve the greatest enhancement. The ratio of the gold to silver was changed from 4:1 to 1:16, as shown in Figure 2.4. It was found that optimized enhancement is achieved when the sputter-coating times are equivalent for gold and silver. An alloy surface with gold and silver is formed during this process for high electro-magnetic enhancement, which is responsible for the enhancement of the Raman signal.

Distance dependence function

SERS response is distance-dependent as described in the previous chapter. EM effect is the primary enhancement in SERS and because EM field decreases in strength with distance from the surface of the SERS substrate. It is presumed that an analyte could benefit from the enhancement of a SERS-active substrate if it were within a certain distance from a substrate. Theoretical calculations have indicated that the SERs enhancement (G) is related to the distance (*d*) from the substrate according to the following equation:

$$\boldsymbol{G = [r/(r + d)]^{10}} \quad \textbf{(1)}$$

Self-assembled monolayers (SAMs) are always of great interest for fabrication of new functional molecules. First of all, SAMs form dense, tightly bonded, and well-ordered monolayers and can provide a straightforward chemical modification environment specific for analytes. Moreover, they can always be used to improve the binding efficiency of large proteins and DNA by patterning and controlling the orientation of large molecules [19-20].

In this study, the optical properties of Au/Ag FON substrate were chemically modified with a series of alkanethiol self-assembled monolayers. The alkanethiol had different chain lengths with formula $HOOCCH_3(CH_2)xSH$ where x equals 6, 8, 10, and 18. For brevity, thiol chemcials are referred to as C6, C8, C10, and C18, respectively. The method used in this work involved self-assembled monolayers (SAMs) of straight-chain alkanethiols on FONs substrates. The monolayer acts as a spacer to determine both the distance dependence of SERS and the EM enhancement. Here, 1mM of the alkanethiol was used for the SAM formations. The surface modifications are as illustrated in Figure 2.5 A). The fresh prepared FON substrate was incubated in the 1mM alkanethiol solution in ethanol for 30 minutes. Then the substrate was washed with plenty of distilled water. After drying at room temperature, R6G as the probe

molecule was spin-coated on the top of the self-assembled monolayer to form another monolayer and its Raman intensity was monitored.

The structure of R6G and the Raman peak assignment are shown in Table 2.2. As indicated in Figure 2.5 B), the Raman intensity is decreased with the increasing of carbon chain length in the self-assembled monolayer. According to theoretical equation, the relative Raman intensity have a relationship with the distance $\boldsymbol{r}$ as $\boldsymbol{G} = [\boldsymbol{a}/(\boldsymbol{a}+\boldsymbol{r})]^{\boldsymbol{10}}$. By integrating the peaks at 1650 cm^{-1}, the experimental data are shown as blue dots in Figure 2.6 A). The nanostructure features of the FON substrate are hypotheses as the distance $\boldsymbol{a}$ between two near nanoparticles with thin film depositions, as illustrated in Figure 2.6 B). From the theoretical geometry calculation, the nanosphere feature of the FON substrate is approximately 40 nm. The best fit polynomial relationship is shown by the blue curve and yields the equation f(r) = 0.942 – 0.225 r+0.0433 r^2. The series expansion of the theoretical equation $\boldsymbol{G} = [\boldsymbol{a}/(\boldsymbol{a}+\boldsymbol{r})]^{\boldsymbol{10}}$ is G=1 - 10 (r/a) + 55 (r^2/a^2), where (10/a) = 0.225, and (55/a^2) = 0.433. By calculating these two equations, the value of the average size of Raman enhancing nanostructure feature a = 40$\pm$5 nm for the FON substrates, which is consistent with the theoretical founding.

1.4 Conclusion

In summary, Ag/Au film over nanosphere as SERS active substrates were fabricated based on the traditional Ag FONs techniques. By optimizing the film thickness, high enhancement factors were achieved for the biosensor condition. In agreement with previous studies, it was shown that by tuning the nanosphere diameter and the thickness, the nanostructure on the substrate surface can be tuned to suit different laser conditions and chemicals [21-22]. These substrates have great potential to be implemented into SERS-based research.

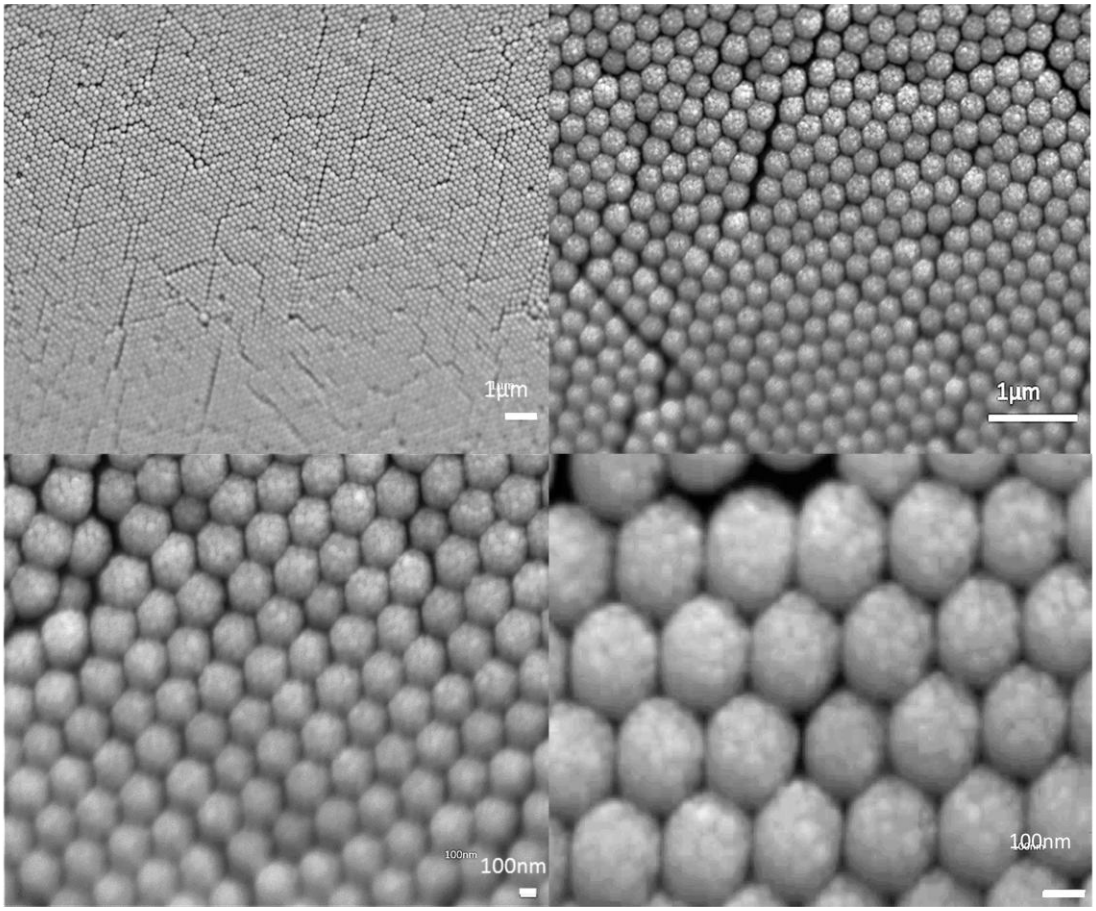

Figure 2.1 SEM of FONs made with 300nm nanosphere.

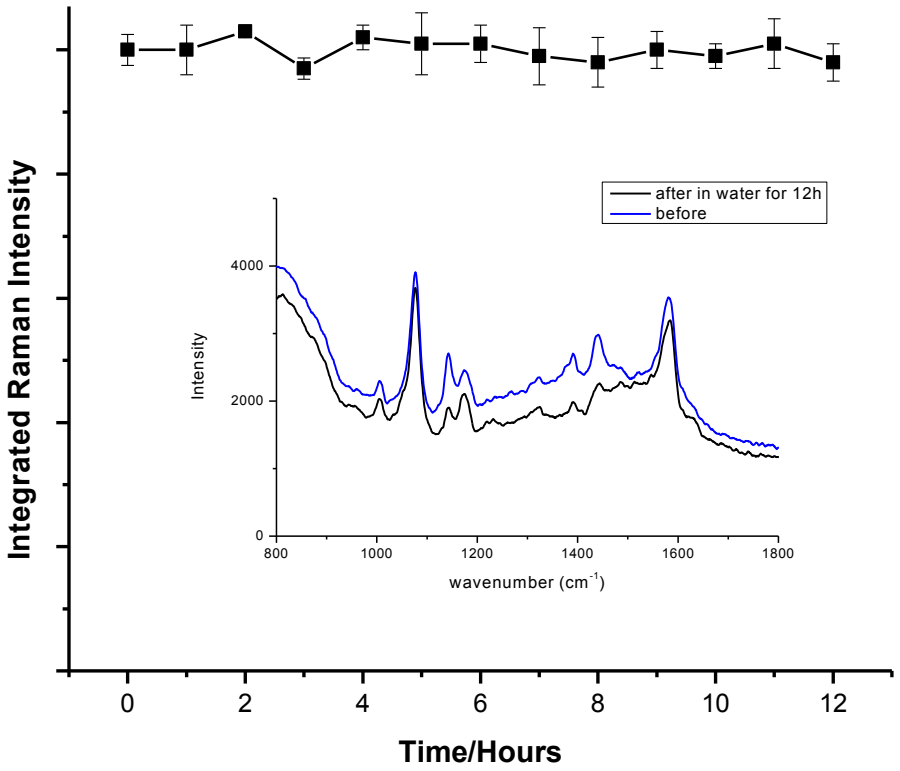

Figure 2.2 Stabiltiy of the FONs substrate. Raman condition: 514nm excitation laser. 20 seconds accommulation time with laser power 25mW. Inset plot shows Raman spectrum of 4-aminothiolphenol before and after 12 hours incubation.

4-Aminothiolphenol (4-ATP)

Wavenumber ν(cm^{-1})	Raman peaks assignment
1077	ν (C-S)
1142	δ (C-H)
1393	δ (C-H)+ δ (C-C)
1440	δ (C-H)$_+$ δ (C-C)
1573	ν (C-C)

Table 2.1 Raman peak assignments of 4-aminothiolphenol [24].

A)

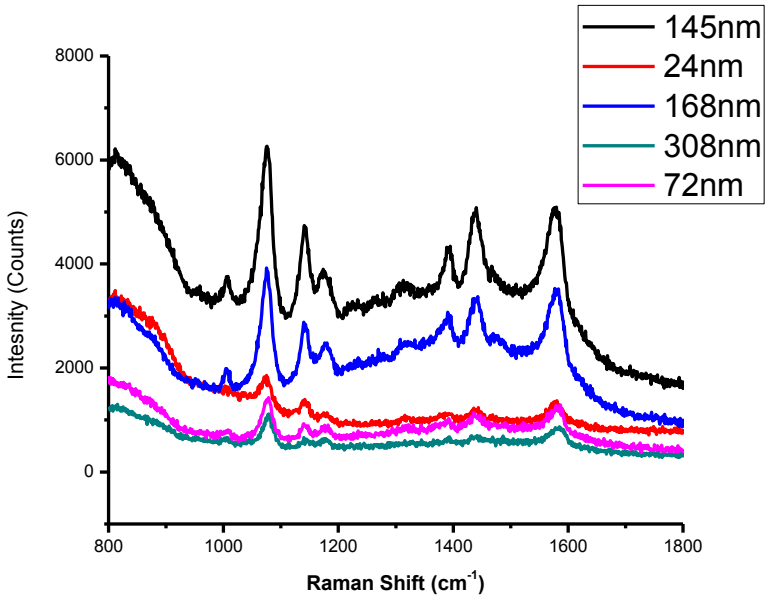

B)

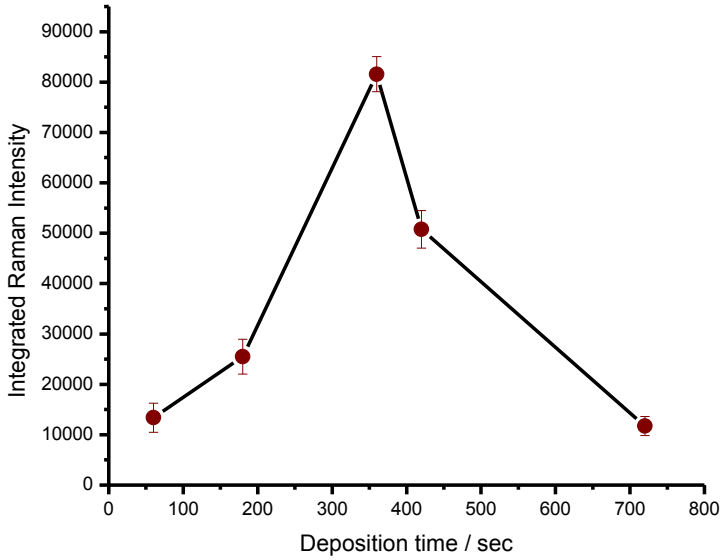

Figure 2.3 Optimizing the total metal thickness on FONs under 514nm laser condition, with different thickness. A) Raman signal at different depostion time. B) Integrated signal trend.

A)

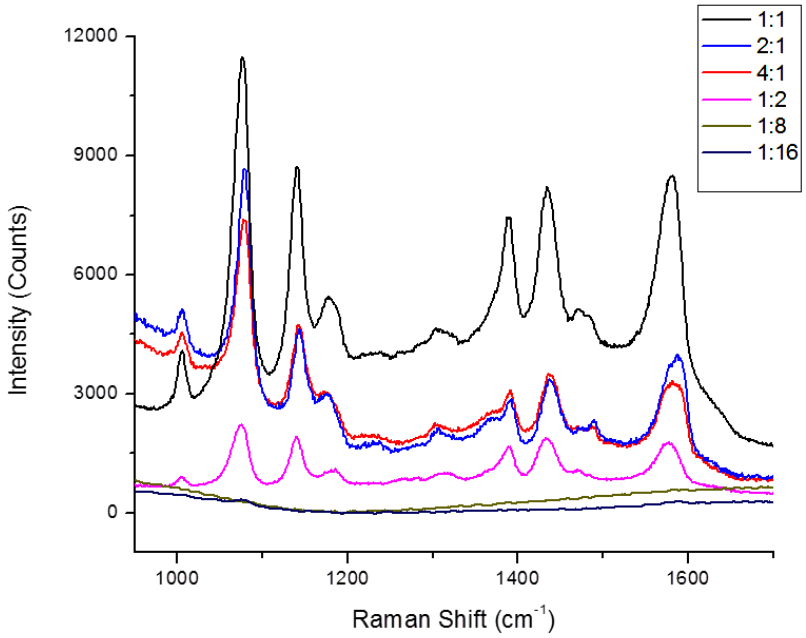

B)

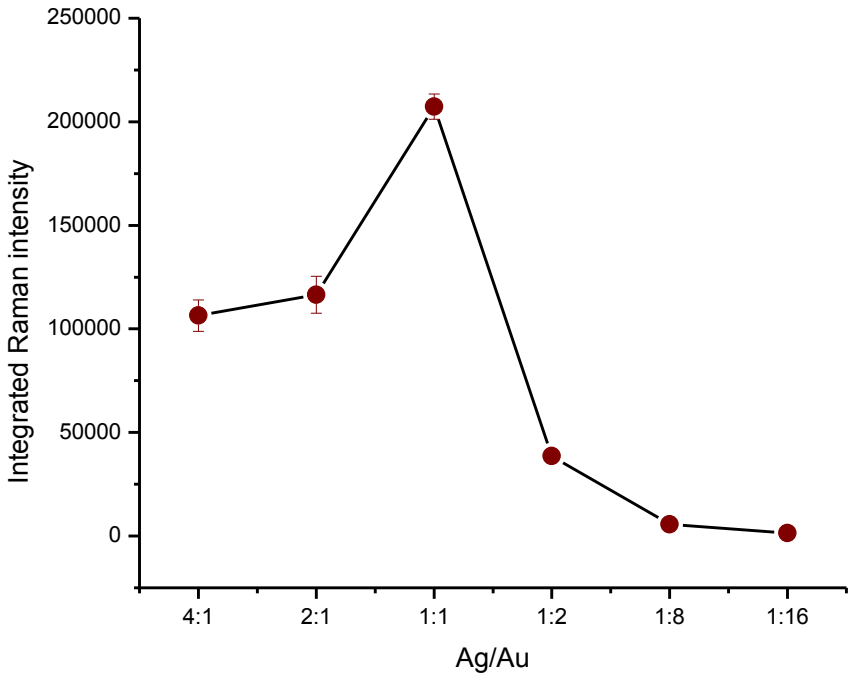

Figure 2.4 A) Optimization of the thickness ratio of Au to Ag: 1:1, 1:2, 4:1, 1:2, 1:8, 1:16 B) Corresponding Raman spectrum of 4-ATP.

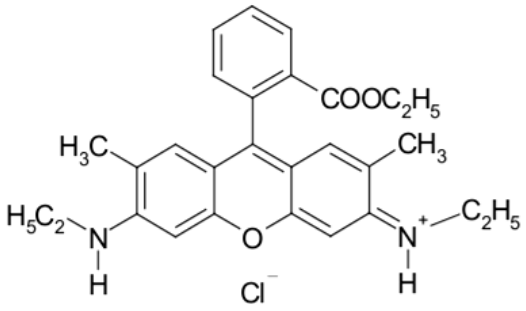

Rhodamine 6G

Regular Raman shift of R6G (cm^{-1})	Assignment	SERS peaks (cm^{-1})
1651	ν(CC)	1650
1569	ν(COC)	1574
1515	ν(CC)	1535
1360	ν(CC)+ν(CN)	1362
1328	ν(CC)+ν(CN)	1313
1198	δ(CH)	1185
778	δ(CH)	772
620	δ(CCC)	613

Table 2.2 Raman peak assignments of R6G [23].

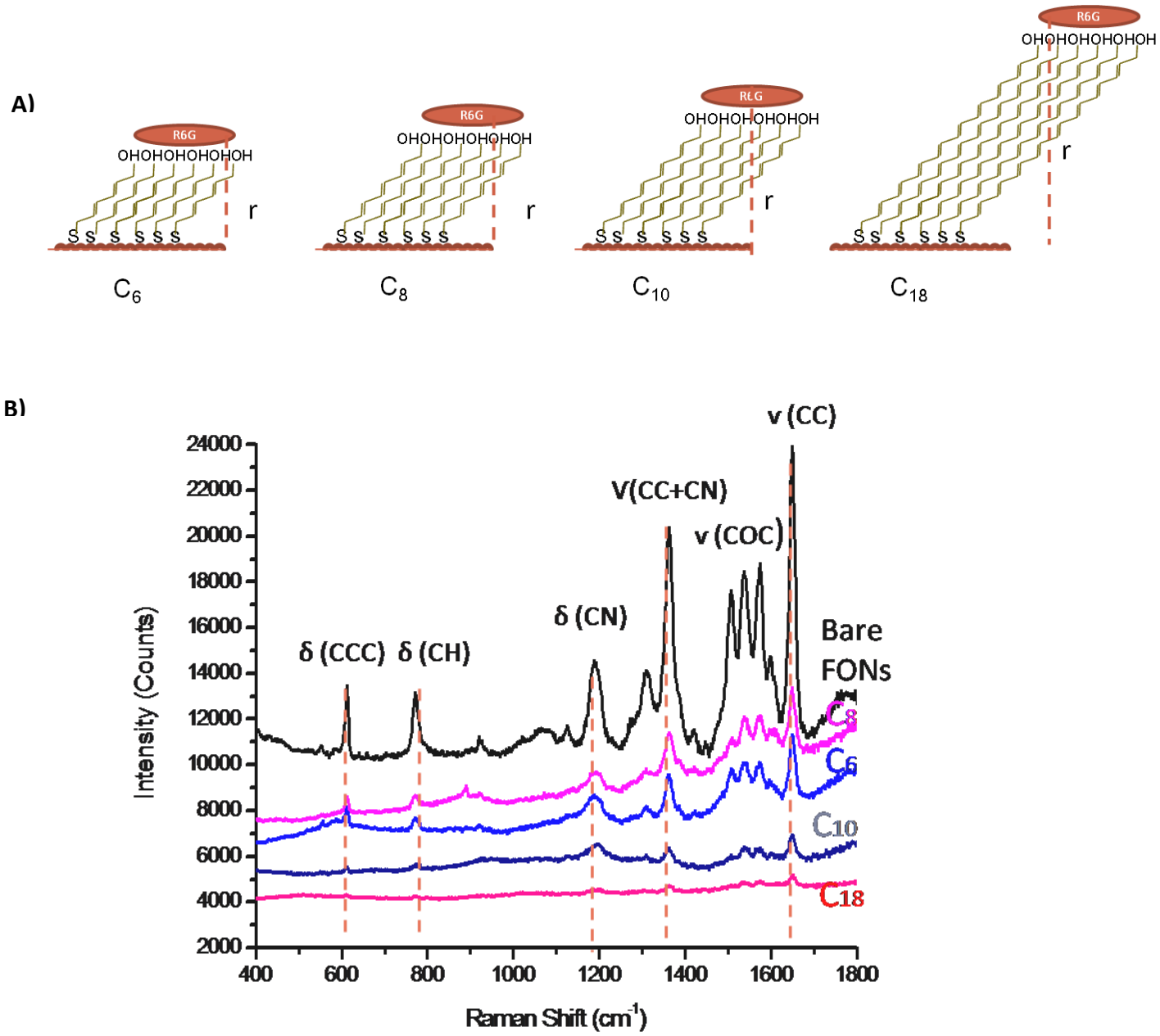

Figure 2.5 A) Illustration of distance-dependent experiments with different alkanethiols. B) Raman spectra of R6G on the FONs substrate surface with SAM of C6, C8, C10, and C18.

A)

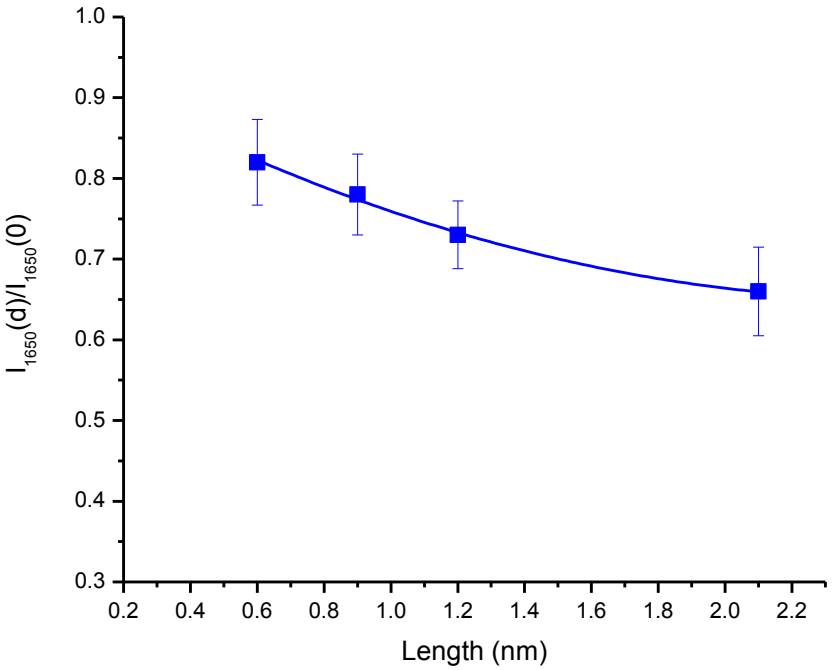

B)

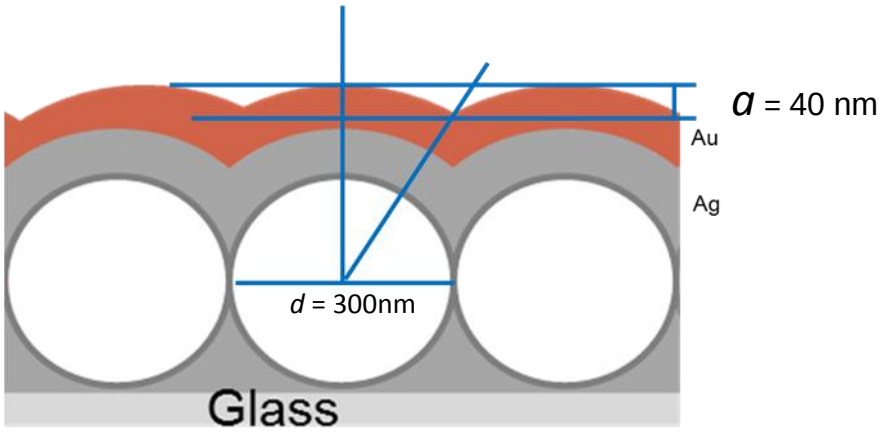

Figure 2.6 A) Relationship between the SERS intensity and length of SAM. B) Geometry model of FONs nanostructure features.

References

[1] Campion, A.; Kambhampati, P. *Chem. Soc. Rev.* **1998**, *27*, 241.

[2] Otto, A. *J. Raman Spectrosc*. **2002**, *33*, 593.

[3] Kneipp, K.; Wang, Y.; Kneipp, H. *Phys. Rev. Lett*. **1997**, *78*, 1667.

[4] Pavel, I.; McCarney, E.; Elkhaled, A.; Morrill, A.; Plaxco, K.; Moskovits, M. *J. Phys. Chem. C,* **2008**, *112*, 4880.

[5] Kelly, K.; Coronado, L.; Zhao, L. L.; Schatz, G. C. *J. Phys. Chem. B*, **2003**, *107*, 668.

[6] Haynes, C. L.; Van Duyne, R. P. *J. Phys. Chem. B*, **2003**, *107*, 7426.

[7] Nie, S.; Emory, S. R. *Science*, **1997**, *275*, 1102.

[8] Hankus, M. E.; Li, H.; Gibson, G. J.; Cullum, B. M. *Anal. Chem.* **2006**, *78*, 7535.

[9] Natan, M. J. *Farad. Discuss.* **2006**, *132*, 321.

[10] Lim, D. K.; Jeon, K. S.; Kim, H. M.; Nam, J. M.; Suh, Y. D. *Nature Mater*. **2010**, *9*, 60.

[11] Sherry, L. J.; Chang, S. H.; Schatz, G. C.; Van Duyne, R. P.; Wiley, B. J.; Xia, Y. *Nano Lett*, **2005**, *5*, 2034.

[12] Yan, B.; Thubagere, A.; Premasiri, W. R.; Ziegler, L. D.; Negro, L. D.; B. Reinhard, M. *ACS Nano,* **2009**, *3*, 1190.

[13] Hatab, N. A.; Hsueh ,C. H.; Gaddis, A. L. *Nano Lett.* **2010**, *10*, 4952.

[14] Im, H.; Bantz, K. C.; Lindquist, N. C.; Haynes, C. L.; Oh, S. H. *Nano Lett*, **2010**, *10*, 2231.

[15] Gartia, M. R.; Xu, Z.; Behymer, E. *Nanotechnology* **2010**,*21*, 39.

[16] Willets, K. A.; Van Duyne, R. P. *Annu. Rev. Phy. Chem.* **2007**, *58*, 267.

[17] Mahajan, S.; Abdelsalam, M.; Suguwara, Y.; Cintra, S.; Russell, A.; Baumberg, J.; Bartlett, P. *Phys. Chem. Chem. Phys*. **2007**, *9*, 104.

[18] Haynes, C. L.; Van Duyne, R. P. *J. Phys. Chem.B*, **2003**, *107*, 7426.

[19] Camden, J. P.; Dieringer, J.; Zhao, J.; Van Duyne, R. P. *Acc. Chem. Res*. **2008**, *41*, 1653.

[20] Haynes, C. L.; Haes, A. J.; McFarland, A. D.; Van Duyne, R. P. *In Topics in Fluorescence Radiative Decay Engineering;* Springer; New York, **2005**, *8*, 47.

[21] Hagan, M. F.; Chakrabortya, A. K.; *J. Chem. Phys*. **2004**, *120*, 4959.

[22] Keighley, S. D.; Li, P.; Estrela, P.; Migliorato. P. *Biosens. Bioelectron.* **2008**, *23*, 1291.

[23] Binh, T. N. *VNU. J. Sci.* **2010**, *26*, 187.

[24] Osawa, M.; Matsuda, N.; Yoshii, K.; Uchida, I. *J. Phys. Chem.* **1994**, *98*, 12702.

Chapter 3

Hairpin-DNA probe for human immunodeficiency virus DNA sequence detection using surface-enhanced Raman spectroscopy

3.1 Introduction

Detection of specific DNA sequences with high selectivity and sensitivity is vital to the future understanding of the human genome project and disease [1]. Many techniques have been developed in the field. These include fluorescence spectroscopy [2] and electrochemical methods [3]. Raman spectroscopy, especially surface-enhanced Raman scattering (SERS), have experienced increasing applications in many fields because of its advantages of very narrow spectral vibrational features characteristic of the investigated samples [4-5]. Following the observation of a high surface-enhanced Raman scattering (SERS) effect for molecules adsorbed on special metallic nanostructured surfaces and nanoparticles; such as Au Ag Cu[6,7], research interests have been focused on two aspects: the active substrate preparation and the practical application. SERS enhancement can reach enhancement factors of 10^{13} to 10^{16}[6, 8]. The technique has been shown great multiplexing ability and has been reported to simultaneously detect several labeled DNA sequences by Mirkin's group [9].

Microfluidic techniques [10, 11] have recently been developed to perform a variety of biomedical and chemical analyses. Compared with conventional techniques, these techniques

have several advantages: they are easy to operate, require a very small volume sample, and generate very little waste.

In this study, SERS DNA sensors and microfluidic channels were incorporated into one system. The systems showed high sensitivity and reproducibility, and it had the advantages of being easy to handle and economical to operate [12, 13].

3.2 Experimental

3.2.1 Chemicals

All the reagents were used as received. Mercaptopropionic acid ($HSCH_2CH_2$ COOH) (MPA) and 4-aminothiophenol (4-ATP) were purchased from Aldrich. The NaOH and tris(hydroxymethyl)aminomethane were purchased from Fischer Scientific and polystyrene carboxyl latex nanospheres from Invitrogen company. All DNA strands were obtained from Integrated DNA technologies (IDT) with HPLC purification. The 46 thiol modified hairpin structure ssDNA were received in a disulfide form, protected by a mercaptohexanol group on one end (/5ThioMC6-D/). Before usage, both the thiol-modified hairpin probe strands DNA and the target DNA were suspended in 1xTE buffer (pH 8) which consists of 10 mM Tris, 1 mM EDTA and 1M NaCl for the DNA reaction. All the solutions were prepared using triply distilled water.

3.2.2 SERS substrate fabrication

In this study, film over nanosphere technique was used to prepare substrates [12, 13]. Briefly, as described in the previous chapter, glass cover slides were cleaned by immersion in piranha solution (3:1 concentrated H_2SO_4: 30% H_2O_2) at approximately 80 °C for 1 hour and following treatment with 5:1:1 H_2O: NH_4OH: 30%H_2O_2 solution for 60 minutes. The glass

substrates were rinsed repeatedly with D.I. water and then used immediately. The polystyrene nanospheres suspension was spin coated to form a polystyrene nanosphere mask. After air drying overnight (~12 h), the nanosphere film was sputter coated with a layer of silver and a top layer of gold. In all the DNA experiments, Au/Ag FONs were used freshly after preparation.

3.2.3 DNA sequences and sensor fabrication

Three different oligonucleotides were designed in the system: hairpin probe oligonucleotide, target oligonucleotide, non-complementary oligonucleotide as illustrated in Table 3.1. The probe used was a hairpin structure with 46 base long oligonucletide as 5'-5ThioMc6/TTTGATCGCCCTTTTCCATTTCCATACATATTTCTGTTAGCGATCT/3Cy3Sp/-3'. The target oligonucleotide used is 39 base long as 3'-AAACT AGCGG GAAAA GGTAA AGGTA TGTAT AAAGA CAAT-5'. The non-complementary oligonucleotide is 39 base long as 5'-ATTGT CTTTA TTCTT TTCTT TTCCT TTTCC CCCCC TTTT-3'. The self-assembled monolayer of oligonucleotide probes was prepared by transferring 10 μL 10.4 μM hairpin probe solutions (1xTE 1M NaCl buffer, pH=8) onto the newly prepared substrate followed by self-assembling for 10 minutes at room temperature. The gold substrate was then soaked in water for 5 minutes and rinsed repeatedly with water to remove probes that were not adsorbed. Following this step, the substrate with hairpin probe was soaked in 1mM MPA solution for 3 minutes to remove the non-specific hairpin oligonucleotide on the substrate surface. After allowed drying, the SERS studies of oligonucleotide probes were conducted at room temperature. The hybridization of oligonucleotide probes was performed according to the following procedure: the substrate modified with the hairpin probes was immersed into a hybridization buffer 10 mM Tris, 1 mM EDTA and 1M NaCl (pH 8) and was incubated at room temperature for approximately 1 hour. Following hybridization, the substrate was then rinsed thoroughly with water. Thus, the

double stranded (ds) helices were formed on the gold substrate. Finally, the Raman spectrum was conducted to measure the sensor performance.

3.2.4 Microfluidic channel design

The procedures for fabricating poly dimethylsiloxane (PDMS) chips were similar to those published previously [11, 12]. Generally, a 1:10 (wt) mixture of PDMS curing agent and prepolymer was mixed thoroughly in a plastic weighing dish. After that, the mixture was poured over the mold into the petri dish, which was then placed in a vacuum desiccator and degassed to remove the air bubbles. The petri dish was then kept in an oven overnight (~12 h) at 70°C. After the chips were cured, they were cut into rectangular shape containing a straight channel and then were peeled off the petri dish. Before applying the PDMS, a silver wire roughed with HNO_3 solution was adhered to the glass slides surface. The glass slides were treated by rinsing with abundant acetone. Then the PDMS containing one microchannel and a glass slide was placed into a plasma system for 45 seconds to allow surface oxidation. Immediately after removal from the plasma cleaner, the PDMS chips were placed on top of the glass slides and sealed together spontaneously. In this procedure, the micro-channel must cross the roughed silver wire as shown in Illustration 3.1. On one end of the channel, a hole of 3 mm in diameter was made through the PDMS as a waste reservoir; on the other end, a syringe with a needle was inserted directly into the micro-channel for fluid control.

3.2.5 SERS instrument

SERS spectra were measured by a Raman microscope system (Renishaw InVia) with a 514.5 nm laser and a 50× long working distance objective lens. The scattered light was passed through a holographic notch filter to eliminate the Rayleigh line. The detector was a charge-

coupled device (CCD) detector. The accumulation time is 20 seconds with five accumulations with laser power 25mW.

3.3 Results and discussions

3.3.1 Principle of the study

Previously, hairpin DNA structures have been widely used as molecular Beacons systems based on the methods of electrochemical and fluorescent detection [2, 3]. In this chapter, a Raman sensor detection that involves a DNA hairpin loop is studied. The DNA hairpin loop has a thiol label molecule at one end and Raman active dye Cy3 at the other end.

Cartoon 3.1 depicted the operating principles of the SERS detection scheme. The substrate for signal enhancement was prepared based on a modification of the film over nanosphere technique. The method is feasible and reproducible. The DNA hairpin probe sequence consists of 46 bp sequence, which contains a sequence section complementary to the target oligonucleotide to be detected, and two stems that have complementary sequences to form a hairpin loop configuration. The hairpin structure is designed such that the Raman active dye is close to the substrate surface when immobilized on the surface, thus giving a strong SERS effect. Then, hybridization with a complementary target DNA opens the hairpin loop and physically separates the Raman label Cy3 from the substrate surface. The Raman enhancement G strongly depends on the distance d, between the Raman label and the substrate surface by $((d+r)/r)^{-10}$. The hybridization process leads to a strong decrease in the SERS signal [14, 15]. In this study, based on the conformational change, the SERS technique was used to detect the response at room temperature.

3.3.2 Characterization of film over nanosphere (FONs) substrate

Experiments were performed to optimize the Ag/Au FONs in order to achieve the strongest SERS enhancement as described in Chapter 2. The deposition time ratio for the silver and gold metal precursor was 1:1 to give a total film thickness of about 145 nm. The diameter of the polystyrene nanosphere used is about 300 nm. As mentioned in the previous chapter, it can be clearly seen that the surface of the Ag/Au substrates is uniform and exhibits good reproducibility. The substrate must be handled with extreme care during experiments because the weak bonds between the Ag/Au and the glass support make the SERS substrate unstable over time.

3.3.3 Effect of the concentration of the DNA probe and mercaptopropionic acid in mixed self-assembled monolayer

Immobilization efficiency of the hairpin sequence on the surface plays an important role in the detection sensitivity. In this sensor system, surface probe density was also carefully considered. Based on previous study, the immobilization time chosen for the immobilization of probe sequence was 10 minutes in this system. The isothermal absorption processes of hairpin DNA monolayer are illustrated in Figure 3.2. By increasing the concentration of the probe sequence, the SERS intensity increased up to 5 μM. This demonstrates that sensor surface was saturated by the probe sequence at this concentration. In the following work, probe concentration of 10.4μM was used for the sensor fabrication.

Mixed self-assembled monolayer of a thiolated DNA sequence and thiol compounds have been used to control the surface density of immobilized DNA. This also allows the control of the orientation and distribution of the DNA sequence as well as steric effect in conformational

changes [16, 17, and 18]. The effect of the concentration of mercaptopropionic acid was used in this study. With mixed SAM of DNA and mercaptopropionic acid, the sensitivity of the sensor was highly improved, because the mercaptopropionic acid and the DNA sequence are both negatively charged. This provides a hydrophilic condition that controls the orientation and distribution of the hairpin probe sequence. Based on five experiments under the same condition, the SERS signal change ratio remained relatively constant upon changing the concentration of MPA from 0.1 mM-100 mM, as shown in Figure 3.3. It is estimated that nonspecific adsorption of the hairpin probe is very low when the DNA concentration is 10.4 μM and the immobilization time is 10 minutes. This concentration does not affect the efficiency of the surface density of the DNA probe.

3.3.4 Response and regeneration performance of the sensor

Figure 3.4 shows the SERS spectra of the DNA hairpin on the SERS substrate introducing the target sequence. In the absence of the target, its conformation is maintained, keeping the Cy3 in close proximity to the surface of the substrate. A strong SERS signal from the Cy3 is observed with typical Raman bands appearing in the region from 1000 cm^{-1} to 1800 cm^{-1} as shown in Table 3.2 and Figure 3.1.

Upon the addition of the target of the same concentration, hybridization occurs resulting in the disruption of the hairpin structure. The Cy3 molecule becomes physically separated from the substrate, resulting in the SERS signal being significantly reduced. In this study, there was an average decrease of 65% of the SERS signals in the 1471 cm^{-1} peak. To demonstrate the reproducibility of the sensors, the spot-to-spot relative standard deviations for at least 10 experiments in each sensor were found to be within 8% either before or after the introducing of

the target. This indicates that although the SERS signal on the substrate is not uniform, the reproducibility is still acceptable. These findings suggested that quantitative detection could be achieved by using the developed SERS-based DNA sensor.

The selectivity of the sensor was studied using a non-complementary DNA sequence. As shown in Figure 3.5, a detectable SERS signal is observed from control DNA experiment that had a non-complementary sequence to the hairpin probe. Because non-complementary sequence cannot disturb the configuration of the probe, there was no significant change of the SERS signal. From the t-test, the P value between the SERS of hairpin DNA monolayer and the buffer control is 0.9854, which indicate no difference. No difference is found between the hairpin and the non-complementary target with the P value 0.5793.

In order to reduce cost, it is always desirable to construct reusable sensors. One method to achieve this is to dissociate the DNA double strand by thermal or chemical methods so as to regenerate the sensor. In this work, the hybridized DNA was regenerated by soaking and washing with copious of 5M NaOH solution. Figure 3.4 shows how the activity of the sensor was recovered after the washing step. SERS responses were found to reproduce easily with signal recovery of 95%.

3.3.5 Detection of the Target sequence

Under optimized conditions, the quantitative aspect of SERS sensor was further investigated to detect target sequence in a 1xTE buffer. As shown in Figure 3.6 A, a series of measurements was carried out. The concentration of the hairpin probe was kept constant at 10.4 μM and the concentration of the target sequence varied from 0.01 to 18.5 μM in all measurements. As shown in Figure 3.6A, SERS intensity decreases with increasing target

concentration. This is consistent with the principles of sensor response with the conformation change. The decrease of the signal with increasing of target concentration confirmed that more hairpin structures were opened up to separate the Cy3 from the substrate during the hybridization process. In further analysis of the sensing process, it was found that there is a relationship between the signal response and the target DNA concentrations, which can be applied in quantitative study shown in Figure 6B. This relationship can be explained by the DNA binding kinetics. When the concentration is low, the target DNA is captured easily by the hairpin probe. However, at higher concentrations, the surface becomes saturated, leaving little room for the target DNA. Moreover, as the target DNA hybridizes to the hairpin probe, the surface becomes densely packed and negatively charged, resulting in steric hindrance and electrostatic repulsion that tend to prevent further hybridization. Therefore, in order to improve the detection sensitivity, the hybridization kinetics must be improved.

3.3.6 Microfluidic channel experiment

To miniaturize the application and make it more convenient, a microfluidic system was designed specifically for the Raman sensor. For the microchip experiments, the chip was mounted on the stage of the Raman microscope and measurements were made *in situ*. Compared with the data from FONs substrate, the microfluidic chip greatly improves the convenience of the system due to less disturbances of the system from the outside environment. As illustrated in Figure 3.7 A), the sensor shows good response with SERS signal changes before and after the incubation with the target molecules. The microfluidic based sensor system can be regenerated by using chemical de-hybridization method (5mM NaOH solution). Additionally, based on 3 different experiments with 3 microfluidic chips, good selectivity against non-complementary DNA sequences are found as shown in Figure 3.7 B). The calibration curve of the microfluidic

systems are shown in Figure 3.8. A similar trend of the sensor response was achieved. However, in the microfluidic system, because roughen silver surfaces have lower Raman enhancement comparing with the FONs substrates, the sensitivity of the sensor system remains a challenge to further studies. The combinations of microfluidic chips with SERS-active substrates in the SERS techniques can therefore be used in various SERS measurements to further improve the sensitivity.

3.4 Conclusion

In summary, a DNA biosensor based on the conformational change of the DNA sequence before and after the hybridization process has been developed. The DNA sensor includes a hairpin structure probe DNA labeled with a Raman reporter, and a free labeled target DNA. The calibration curve with different concentration of target sequence was constructed indicating a SERS signal change of up to 70% upon hybridization. To miniaturize the system, a microfluidic channel was designed. More studies need to be conducted to improve the sensitivity of the sensor. In addition, because SERS is a potential technique for multiplexing, a multiplexing system to simultaneously detect several different DNA sequences will be investigated. Optimization of the substrate and Raman measurement conditions should be considered to improve the sensitivity of the biosensor.

Name	Sequences (5’-3’)	5’Modification	3’Modification
Probe DNA	TTTGATCGCCCTTTTCCATTT CCATACATATTTCTGTTAGCG ATCT	Mercaptohexanol	Cy3
Target DNA	TAACAGAAATATGTATGGAA ATGGAAAAGGGCGATCAAA	_	_
Non complementary	TAACAGAAATAAAAATGGAA AAGGAAAAGGGCGATCAAA	_	_

Table 3. 1 Oligonucleotide sequences and modification information.

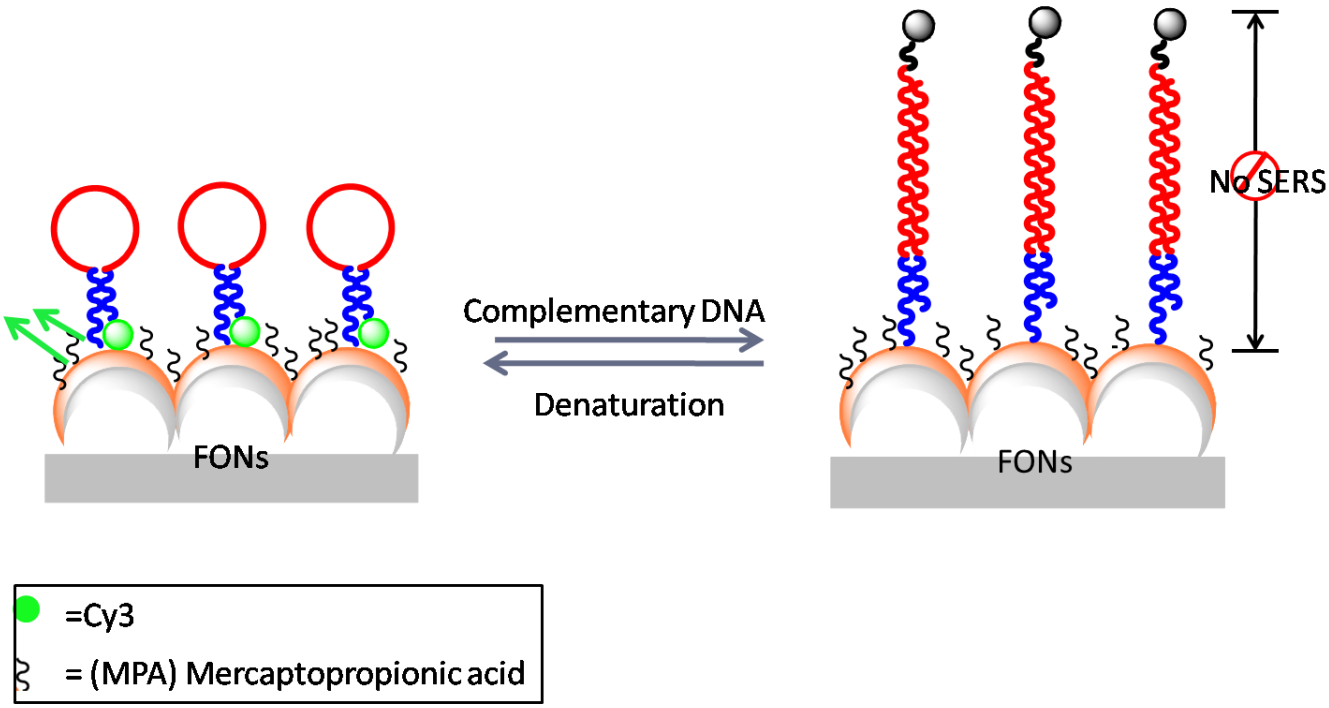

Illustration 3.1 Principle of sensor response.

Raman shift (cm^{-1})	**Assignment**
1587	б(C=C)+ν(C-C)
1470	ν(C-C)
1409	б(C-H)
1394	б(C-N)
1311	б(C-H)
1196	ν(C-C)+б(C-N)

Table 3.2 Cy3 Raman peak assignments [20].

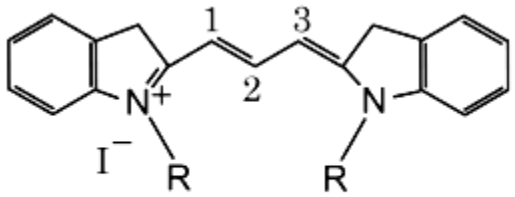

Cy3

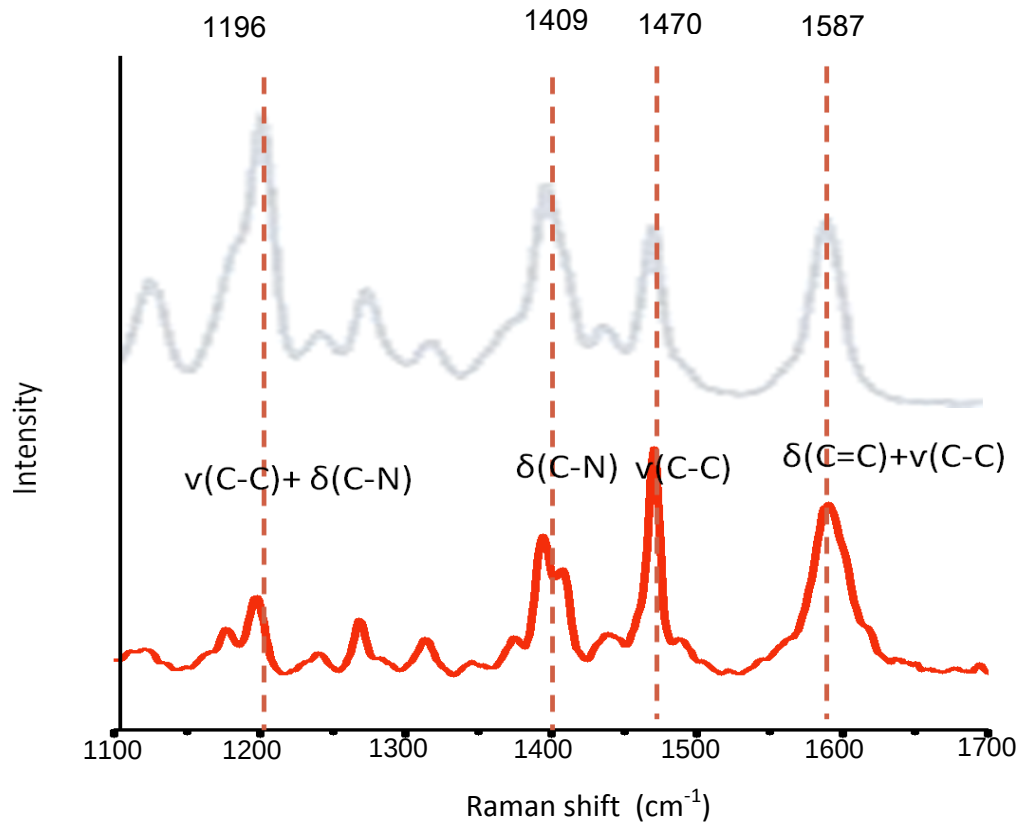

Figure 3.1 Raman spectrum of Cy3 and peaks assignment. Gray curve is from literature (Reprinted from Ref 19) and red curve is obtained from the sensor system. Raman condition: 514 nm laser, 20 seconds accumulation time.

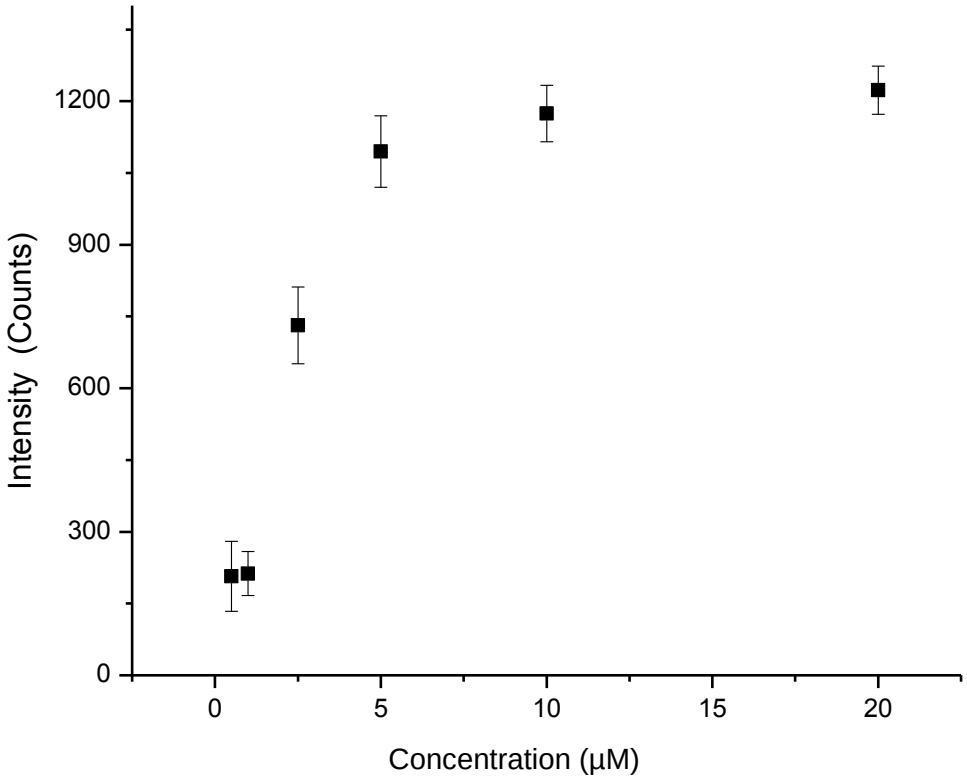

Figure 3.2 Hairpin DNA monolayer isothermal absorption process. SERS of DNA probe on the FONs surface with concentration change from bottom to top: 1.3μM, 2.6μM, 5.2μM, 10.4μM, 20.8μM.

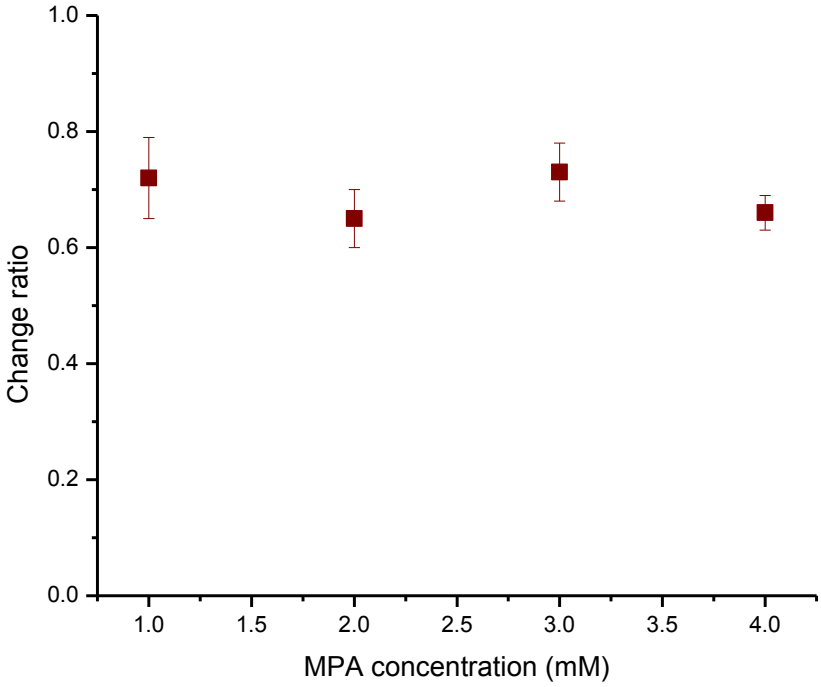

Figure 3.3 MPA concentration effect.

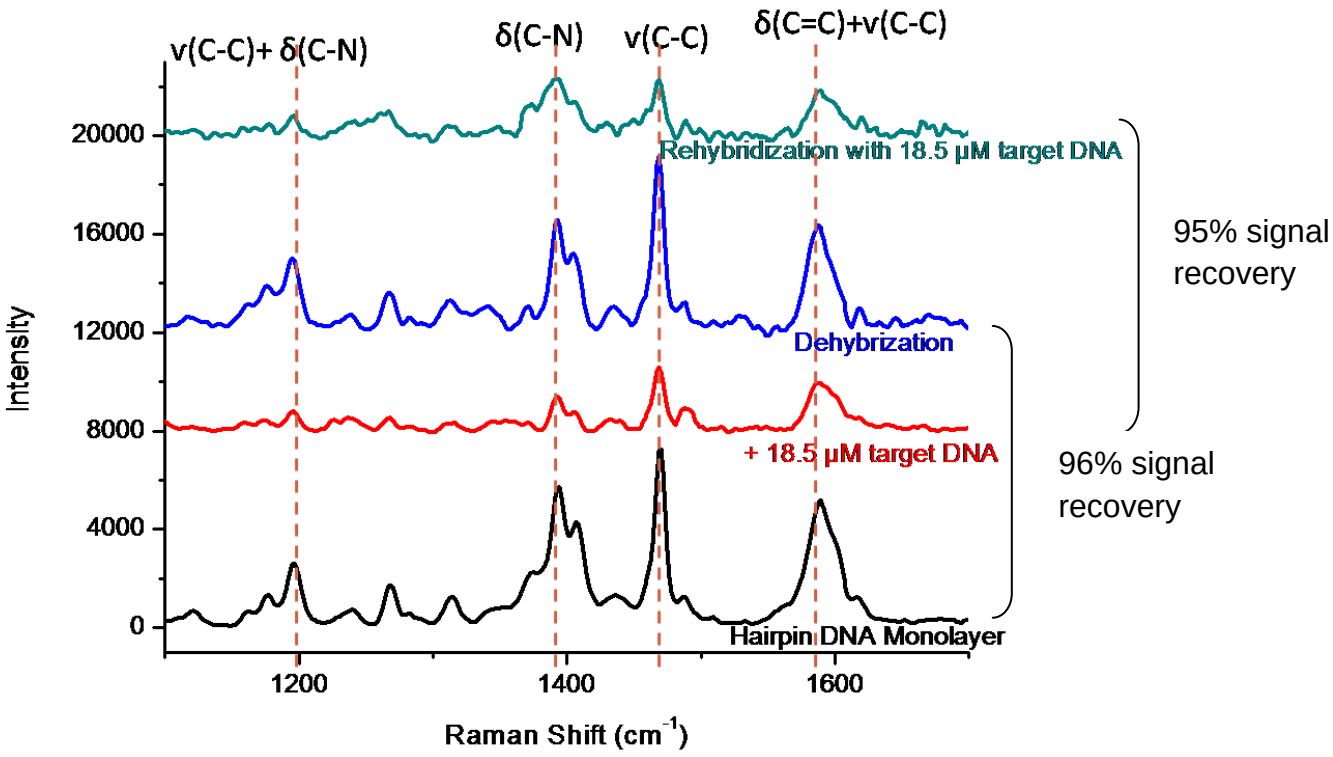

Figure 3.4 SERS response before and after introducing DNA target. The concentration of DNA probe is 10.4 µM and the concentration of target 18.5 µM.

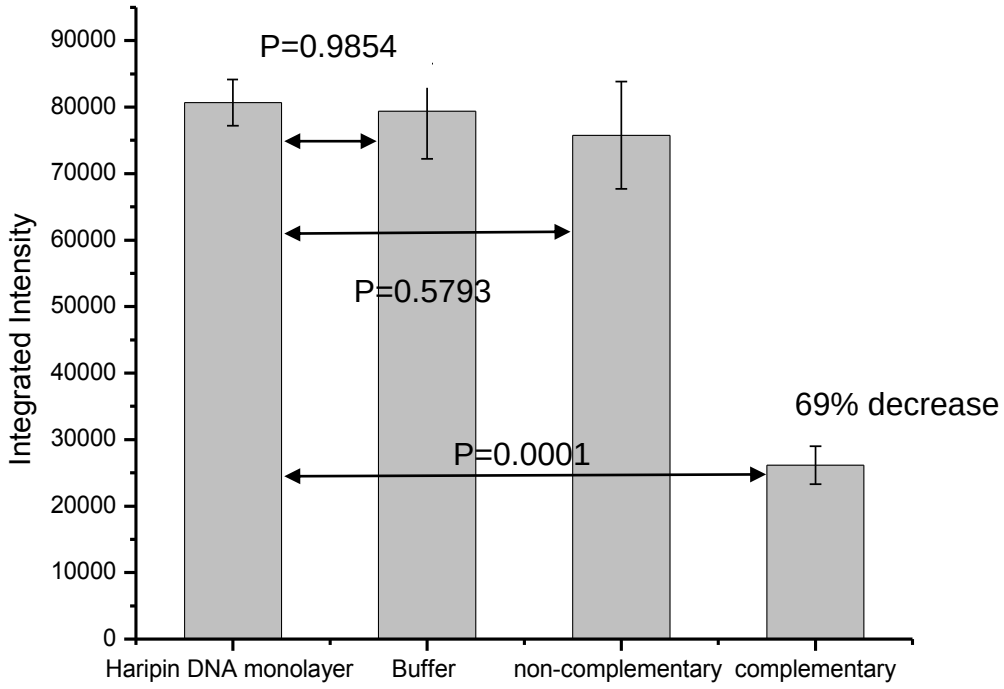

Figure 3.5 SERS response and control experiments. SERS relative signal after DNA probe modified on FONs surface, buffer solution incubation, non-complementary DNA incubation, and complementary DNA incubation (based on 10 experiments).

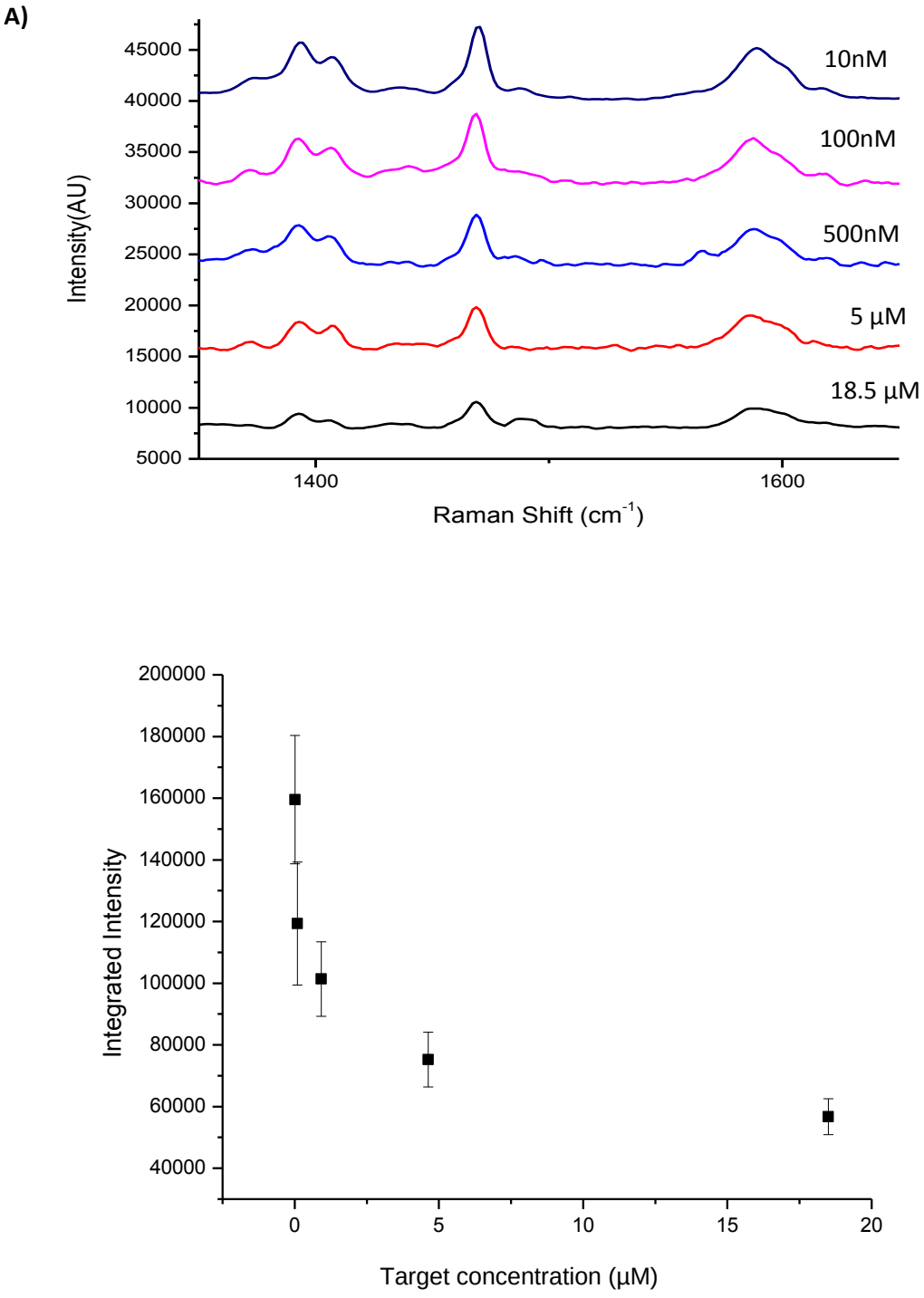

Figure 3.6 Calibration curve A) SERS response with adding target concentration (from top to bottom) 0.01µM, 0.1 µM, 0.5µM, 5µM, 18.5µM. B) SERS response by using peak position 1470 cm^{-1}.

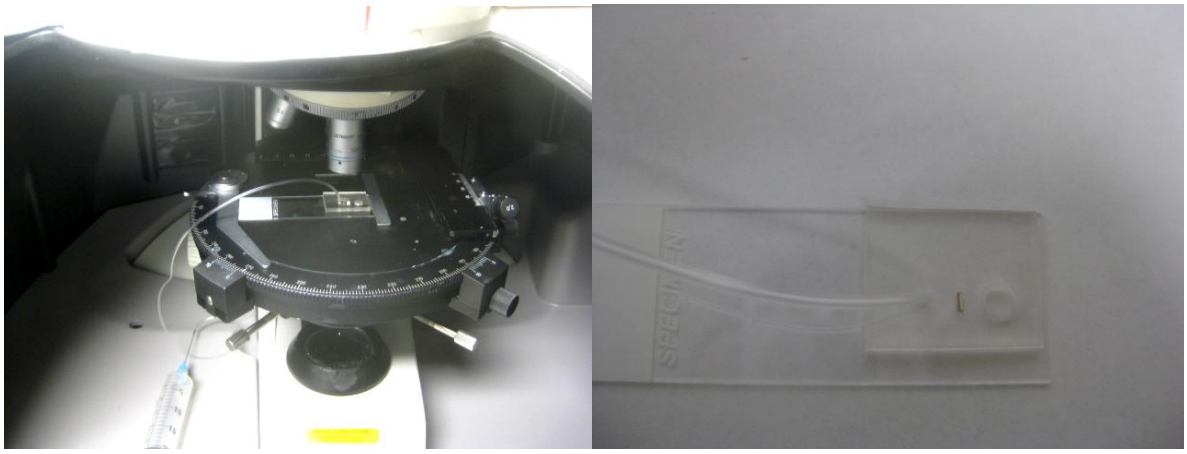

Picture 3.1 Microfluidic chip designed for DNA sensor with Raman measurement.

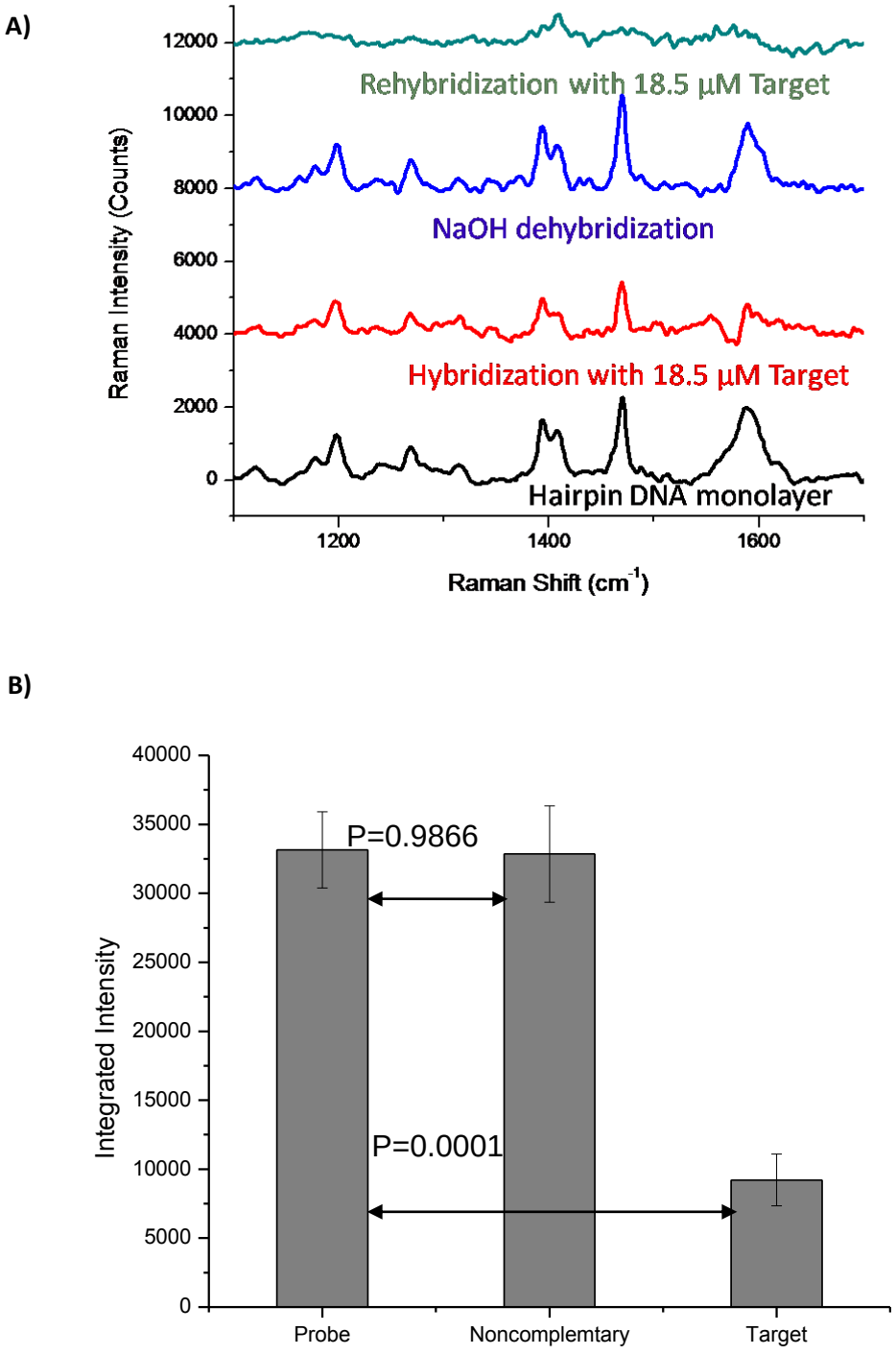

Figure 3.7 SERS response and control experiments in the microfluidic system. A) Sensor responses. B) Control experiments, hairpin SAM, non-complementary DNA incubation, and complementary DNA incubation.

A)

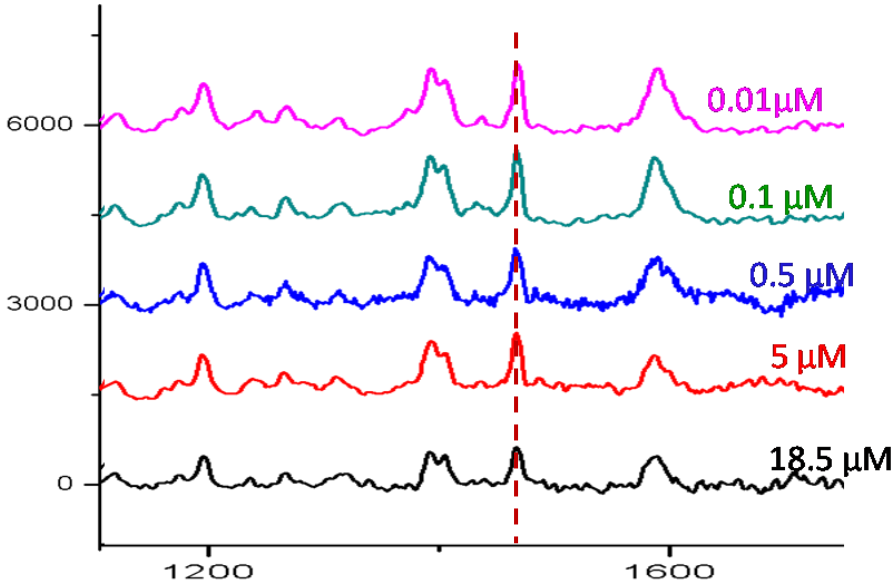

B)

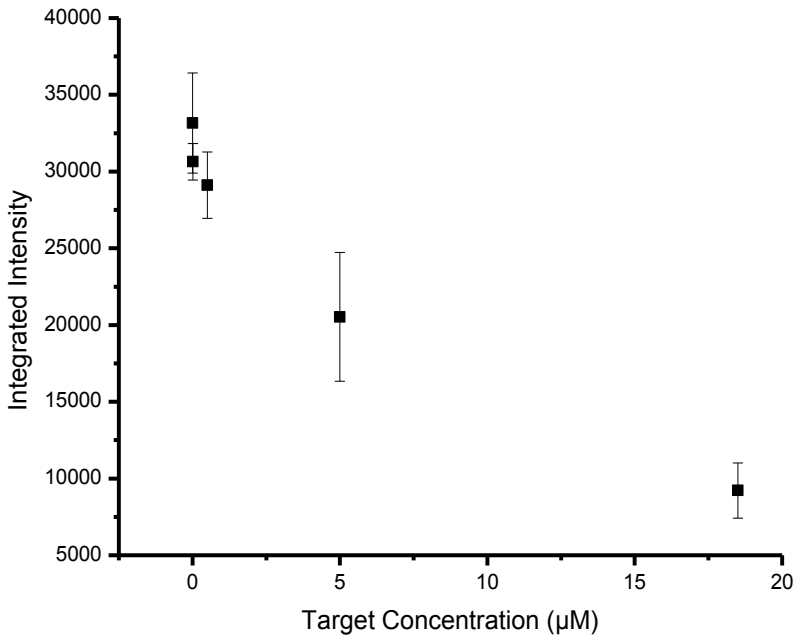

Figure 3.8 A) Calibration curve, SERS response with adding target concentration (from top to bottom) 0.01µM, 0.1 µM, 0.5µM, 5µM, 18.5µM. B) SERS response by using peak position 1470 cm^{-1}.

References

[1] Dieringer, J. A.; McFarland, A. D.; Shah, N. C.; Stuart, D. A.; Whitney, A.V.; Yonzon, C. R.; Young, M. A.; Zhang, X. Y.; Van Duyne, R. P. *Faraday Discuss*. **2006**, *132*, 9.

[2] Vet, J. A.; Majithia, A. R.; Marras, S. A.; Tyagi, S.; Dube, S.; Poiesz, B. J.; Kramer, F. R. Proc. *Natl. Acad. Sci*. **1999**, *96*, 6394.

[3] Graham, D.; Mallinder, B. J.; Smith, E. W. *Angew. Chem., Int. Ed.* **2000**, *39*, 1061.

[4] Nie, S.; Emory, S. R. *Science* **1997**, *275*, 1102 .

[5] Wabuyele, M. B.; Vo-Dinh, T. *Anal. Chem.* **2005**, *77*, 7810.

[6] Chang,R. K.; Furtak, T.E. *Surface Enhanced Raman Scattering*, Plenum Press, New York, **1982**.

[7] Haynes, C. L.; McFarland, A. D. Van Duyne, R. P. *Anal. Chem*. **2005**, *77*, 338A.

[8] Albrecht, M. G.; Creighton, J. A. *J. Am. Chem. Soc.* **1977**, *99*, 5215.

[9] Cao, Y. C.; Jin, R. C.; Mirkin, C. A. *Science* **2002**, *297*, 1536.

[10] Chen, J.; Jiang, J.; Gao, X.; Liu, G.; Shen, G.; Yu, R *Chem. Eur. J.* **2008**, *14*, 8374.

[11] Endo, T.; Kerman, K.; Nagatani, N.; Takamura, Y.; Tamiya, E. *Anal. Chem.* **2005**, *77*, 6976.

[12] Stuart, D. A.; Biggs, K. B.; Van Duyne, R. P. *Analyst* **2006**, *131*, 568.

[13] McFarland, A. D.; Young, M. A.; Dieringer, J. A.; Van Duyne, R. P. J. *Phys. Chem. B* **2005**, *109*, 11279.

[14] Wolkow, R. A.; Moskovits, M. J. J. *Chem. Phys.* **1987**, *87*, 5858.

[15] Campion, A.; Kambhampati, P. *Chem. Soc. Rev.* **1998**, *27*, 241.

[16] Gearheart, L. A.; Ploehn, H. J.; Murphy, C. J. *J. Phys. Chem. B* **2001**, *105*, 12609.

[17] Du, H.; Strohsahl, C. M.; Camera, J.; Miller, B. L.; Krauss, T.D. *J. Am. Chem. Soc.* **2005**, *127* ,7932.

[18] Tonya, M. H.; Tarlov, M. J. *J.Am. Chem. Soc.* **1997**, *119*, 8916.

[19] Cao, Y.C.; Jin, R.; Mirkin, C. A. *Science* **2002**, *297*, 1536.

Chapter 4

Hybrid materials for supercapacitor application

4.1 Introduction

Hybrid supercapacitors have recently received attention because of their combined advantages of electric double layer capacitors (EDLCs) and pseudocapacitors. Through Faradaic and non-Faradaic processes of storing energy, hybrid supercapacitors can reach higher power and energy densities than supercapacitors without losing cyclability and affordability [1]. Recent research has mainly focused on two different kinds of composite materials: carbon materials integrated with conducting polymers, and carbon materials integrated with metal oxide to take advantage of both physical and chemical charge storage mechanisms together in a single electrode [2-3]. On one hand, the carbon based materials have a large surface area which could improve the contact efficiency between the deposition materials and the solutions [4-8]. On the other hand, the metal oxide materials enable further improvement of the hybrid electrode through the redox reactions [6].

For electrolytic supercapacitors, Mn_3O_4 is a promising electrode material because of its abundance, low cost, environmental compatibility, and naturally high energy storage capacity [6, 9, 10]. However, Mn_3O_4 has poor electronic conductivity. It also has limitations of low surface areas and relatively small specific capacitance. On the contrary, carbon materials are both light weighted and electronically conductive with relatively large surface area. Therefore, by combining Mn_3O_4 into composites with carbon materials, the conductivity of the composite will be greatly enhanced without losing the capacitance [11]. Many fabrication methods have been

published regarding the preparation of hybrid metal oxides for energy storage. For example, solid state reactions have been utilized in the process of thermal decomposition of the respective metal salts. Physical methods have been used, whereby metal oxide salts are mixed mechanically in a process called ball milling [12-15]. Electrochemical deposition methods have become popular because they can overcome the problems of other fabrication processes such as non-uniformity and insufficient contact. Electrochemical cathodic and anodic depositions have been achieved by using corresponding metal salt in the solution [14-17]. However, improvement of the deposition process must be carefully considered in order to maintain the physical and thermal stability of the materials.

4.2 Experimental

4.2.1 Chemicals

Commercial purity $MnCl_2 \cdot 4H_2O$ and polyethylenimine (PEI, Mw = 70,000) were purchased from Aldrich and used as received. In addition, 5mM $MnCl_2$ solutions containing 0.4–0.8 g/l PEI in the ethanol–water (5vol % water) solvent were prepared and used for electro-deposition. The solution of $MnCl_2$ was turned brown after the addition of PEI. Cathodic deposits were obtained on working electrode (50 mm×50 mm×0.1 mm) by the galvanostatic method at a current density of 1 mA/cm^2. The deposition time was varied in the range of up to 1 hour. Cathodic deposition method is used in our study to avoid anodic dissolution of the substrates during electro-deposition.

4.2.2 Characterization

Raman spectroscopy, X-rays diffraction (XRD) and scanning electron microscopy (SEM) were used to characterize the morphologies, structures, and chemical composition of the electrode surface.

Raman measurements were performed using the 514 nm laser (20 mW) from an air-cooled argon ion laser (Spectra-Physics Lasers, Inc.) as the excitation source. Raman spectra were collected and analyzed using a Renishaw InVia Raman microscope system.

4.2.3 Electrochemical test and specific capacitance calculation

All electrochemical measurements were carried out at room temperature using a three-electrode set-up. The reference electrode was Ag/AgCl (Bioanalytical Systems, Inc.), and the counter electrode was Pt. gauze. The deposition was studied by weighing the substrates before and after deposition experiments followed by air drying at room temperature for 24 hours.

Cyclic voltammetry (CV) measurements were carried out in a 0.5 M KOH solution from 0mV to 800mV at different scan rate. The Specific capacitance (SC) was calculated by first integrating the area in the CV plot to obtain the charge (Q), and then dividing the charge by the mass of the electrode m and the width of the potential window ΔV as indicated in Equation (1):

$$Cs = \frac{Q}{m\Delta V} \qquad (1)$$

Charging and discharging cycles were performed using three-electrode set up, with Ag/AgCl as the reference electrode. Galvanostatic charge and discharge cycling in the potential range of 0–0.6V was performed at a constant current density. The charge and discharge curves obtained were used for the calculation of SC from Equation (2).

$$Cs = \frac{I}{\left(\frac{dV}{dt}\right)m} \qquad (2)$$

where $\frac{dV}{dt}$ is the slope of the linear discharge curve and *I* is the discharging current.

4.3 Results and Discussion

4.3.1 Mn_3O_4 deposition rates studies

As described above, the cathodic deposition method was used in the study to avoid anodic dissolution of the substrates during the electro-deposition process. The weight of the material deposited as a function of deposition time was studied in 5 mM $MnCl_2$ solutions, containing 0.4 g/l PEI. Figure 4.1 indicates that the weight of the deposit increases with deposition time at a constant deposition current density. The increase in the weight of deposit was basically linear, demonstrating a constant rate of the cathodic deposition. The use of the PEI, which has natural binding property, allows the formation of adherent and relatively thick oxide films with little or no cracks [18].

As described in previous reports, the mechanism of the cathodic deposition is based on the formation of the PEI-Mn^{2+} complexes in the solution, followed by the deposition of the oxidized Mn [18,19]. The color change before and after adding the PEI solution indicated the successful formation of the complex in the system.

4.3.2 Hybrid materials characterizations

Two kinds of material were used in this study: stainless steel fiber (ss) and carbon fiber. After deposition of Mn_3O_4, the hybrid materials were characterized using Raman spectroscopy with 514 nm laser. As shown in the Raman spectrum Figure 4.2, a typical peak at 650 wavelength number reflects the formation of Mn_3O_4 on electrode surface of stainless steel mesh.

Similarly, Mn_3O_4 characterization for the carbon mesh with the same parameters is shown in Figure 4.3. The graph shows typical peaks from the carbon materials (at 1598 and 1339 cm^{-1}) and the one at 635 wavelength number specifically from the Mn_3O_4 deposition. Those

results illustrate the successful deposition of the Mn_3O_4 on both stainless steel mesh material and carbon fiber material.

Both of the hybrid materials were further studied using XRD. To avoid the background noise from the carbon fiber and stainless steel fiber, Mn_3O_4 was prepared to cover the whole surface. Deposition solution was 5 mM $MnCl_2$, containing 0.4 g/l PEI. The deposition time was 50 minutes. Under these conditions approximately 0.9 mg were deposited on the surface of 1 cm^2 carbon fibers. In order to achieve accurate spectrums, the hybrid materials (Mn_3O_4/stainless steel and Mn_3O_4/carbon fiber) were freshly prepared and dried under air for 24 hours. X-ray diffusion studies of the fresh deposits prepared from the 5 mM $MnCl_2$ solution containing 0.4 g/l PEI show broad peaks in the XRD spectrum, which indicate successful deposition of the Mn_3O_4. The broad peaks are a result of the amorphous nature as shown in the Figure 4.4 and Figure 4.5

SEM was used to study the deposition condition before and after the Mn_3O_4 deposition. Figure 4.6 shows the stainless steel fiber material, and Figure 4.7 shows the Mn_3O_4/Stainless steel hybrid material. The difference before and after the Mn_3O_4 deposition can be understood from the surface structure. Figure 4.8 and Figure 4.9 show the carbon fiber material before and after the Mn_3O_4 deposition. Clearly, deposition not only forms on the surface of the material electrode but also shows uniformity within the material, which suggests good contact of the Mn_3O_4 with carbon fiber and stainless steel fiber.

4.3.3 Electrochemical tests

Cyclic voltammetric (CV) studies of both hybrid materials are shown in Figure 10 and Figure 11. Figure 10 represents the CV from the Mn_3O_4/ss hybrid materials, and Figure 11 represents the CV for Mn_3O_4/Carbon fiber materials. Both hybrid materials were prepared with an area of 1 cm x 1 cm and used as the working electrode. The capacitive responses were

measured in the potential window of 0–0.8 V versus Ag/AgCl at different scan rates. As illustrated in Figure 11 A and Figure 12 A, there are no re-dox peaks in the range between 0 and 0.8 V and typical CV curves obtained at different scan rates show a roughly rectangular shape with respect to the zero-current line, which indicates that the composite electrode exhibits a capacitive behavior.

SCs are calculated using Equation (1). Figures 4.10 B and 4.11 B show the results of specific capacitance at different scan rates for the composite electrodes. As shown in the figures, the specific capacitance decreased with the increasing scan rate due to limitation in the diffusion of the electrolyte. The highest specific capacitance of 544 F/g was achieved for Mn_3O_4/stainless steel fiber and 562 F/g for Mn_3O_4/carbon fiber, respectively. The results show that the hybrid materials have good performance relative to other hybrid materials reported.

Charge–discharge behaviors for the composite electrodes were obtained at two different current densities as depicted in Figures 4.12 and 4.13. The SC calculated from Equation (2) is 366 F/g, which is consistent with the average calculation form the CV plot using equation (1). The average SC value calculated from the CVs of the Mn_3O_4/ Carbon fiber was found to be 452 F/g which is close to the specific capacitance of 428F/g for charging and discharging measurement.

4.4 Conclusion

In summary, two types of hybrid material were fabricated using cathodic deposition of Mn_3O_4 and both showed good supercapacitor performance. A comparison between the stainless steel fiber and carbon fiber shows the carbon fiber exhibits better capacitive activity. By controlling the deposition time, higher capacitances can be achieved. In addition, the cathodic method has the advantage of avoiding dissolution of the Mn_3O_4 [20-21]. It is believed that the

cathodic deposition method can be used to improve the duration of the supercapacitor. However, more detailed studies are needed for the practical application of the materials. This includes better control of the fabrication process. In addition, the thermal stability (TGA) and cycle duration also need to be studied to better understand the supercapacitor performance.

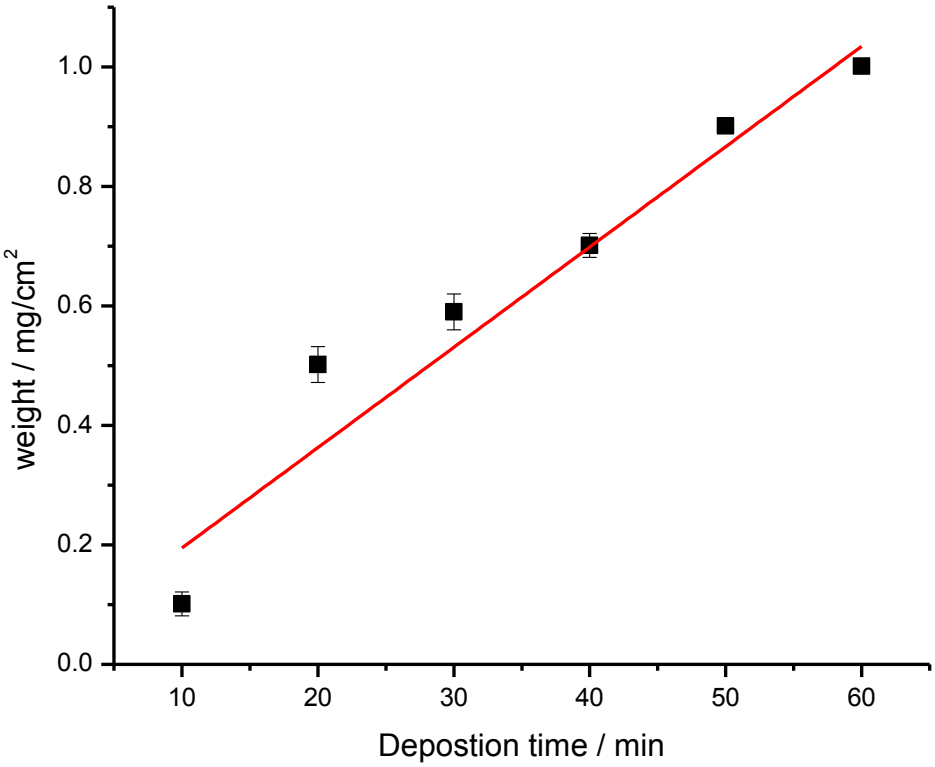

Figure 4.1 Deposit weight Vs deposition time for the cathodic deposits, prepared with the 5mM $MnCl_2$ solution containing 0.4 g/l PEI at a current density of 1 mA/cm^2.

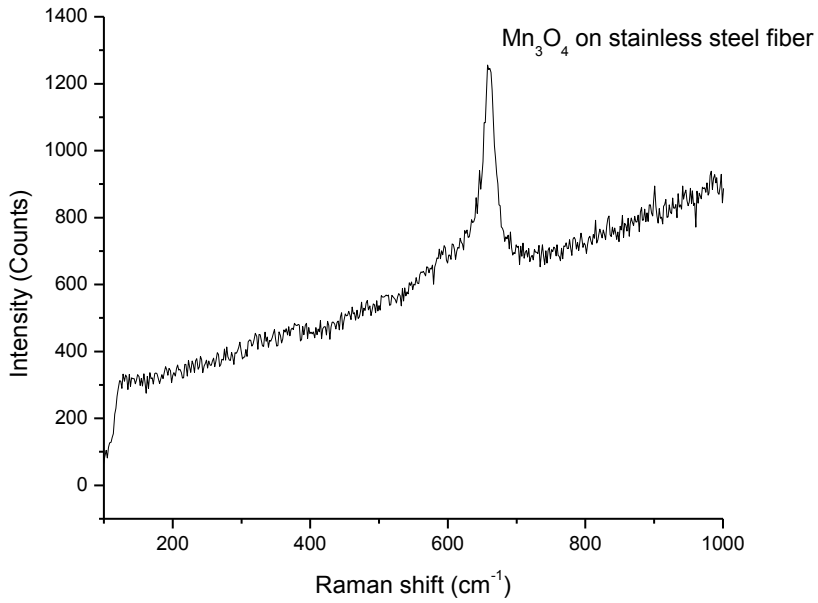

Figure 4.2 Raman spectrum of Mn_3O_4 deposition on the stainless steel fiber surface. Raman measurement condition: 514nm excitation laser and 10 seconds accumulation time.

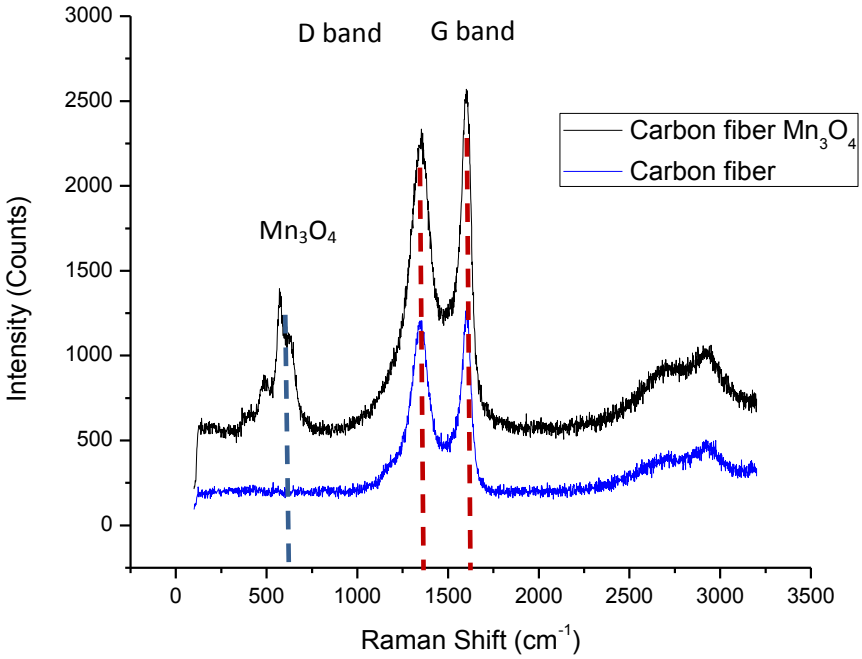

Figure 4.3 Raman spectrum of Mn_3O_4 deposition on the carbon fiber material, bottom one is the blank carbon fiber, the top one is the fiber after the deposition. Raman measurement condition: 514 nm excitation and 5 accumulations with 20 second per accumulation.

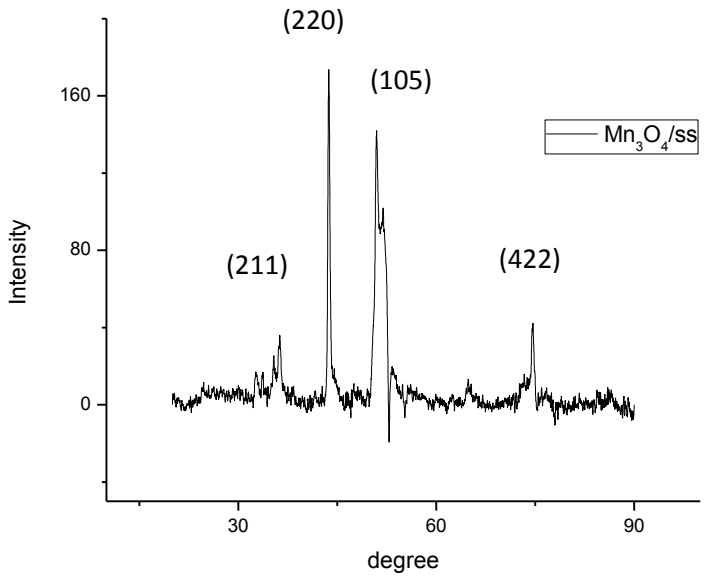

Figure 4.4 XRD spectrum of Mn_3O_4 / stainless steel fiber hybrid materials.

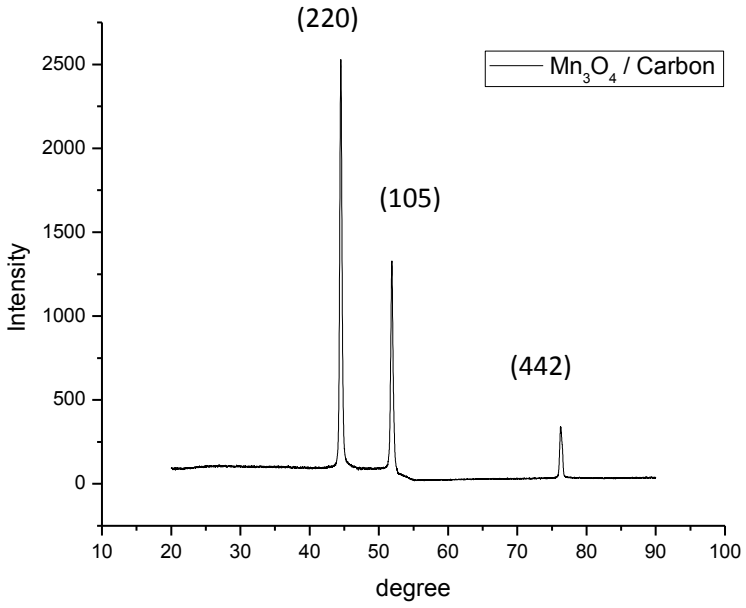

Figure 4.5 XRD spectrum of Mn_3O_4 and carbon fiber hybrid material.

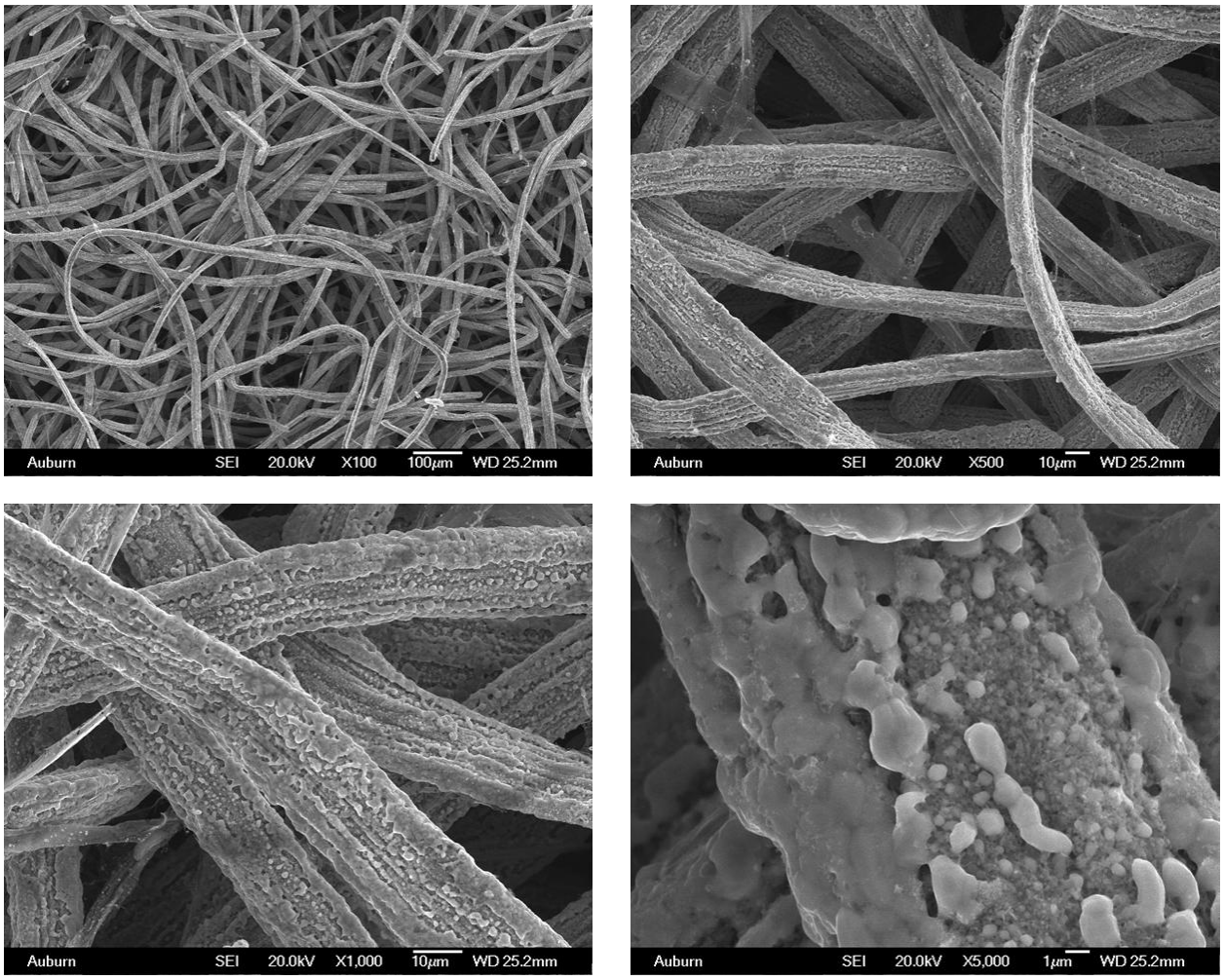

Figure 4.6 SEM of the stainless steel mesh material without Mn_3O_4 deposition.

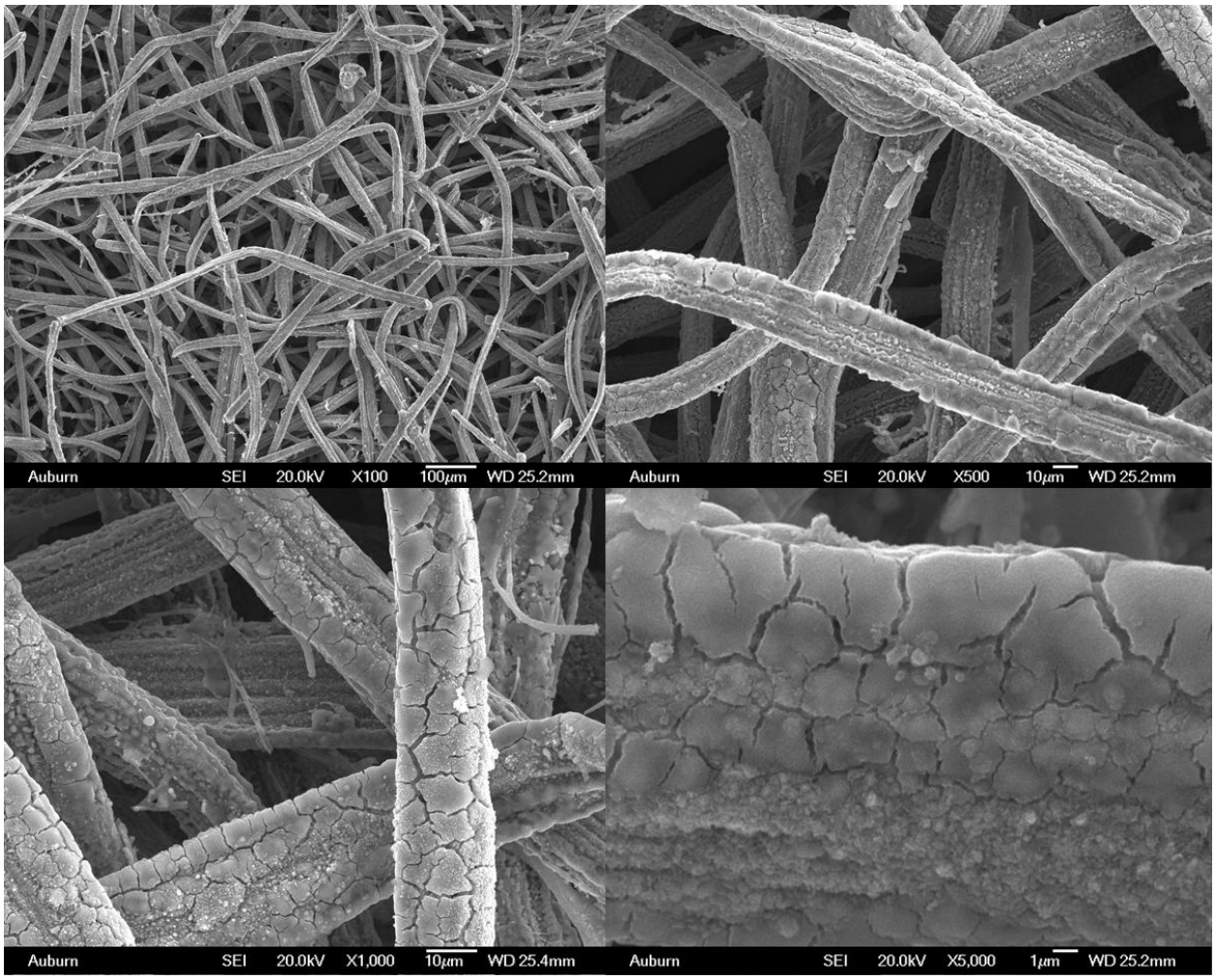

Figure 4.7 SEM of Mn_3O_4/Stainless steel hybrid material.

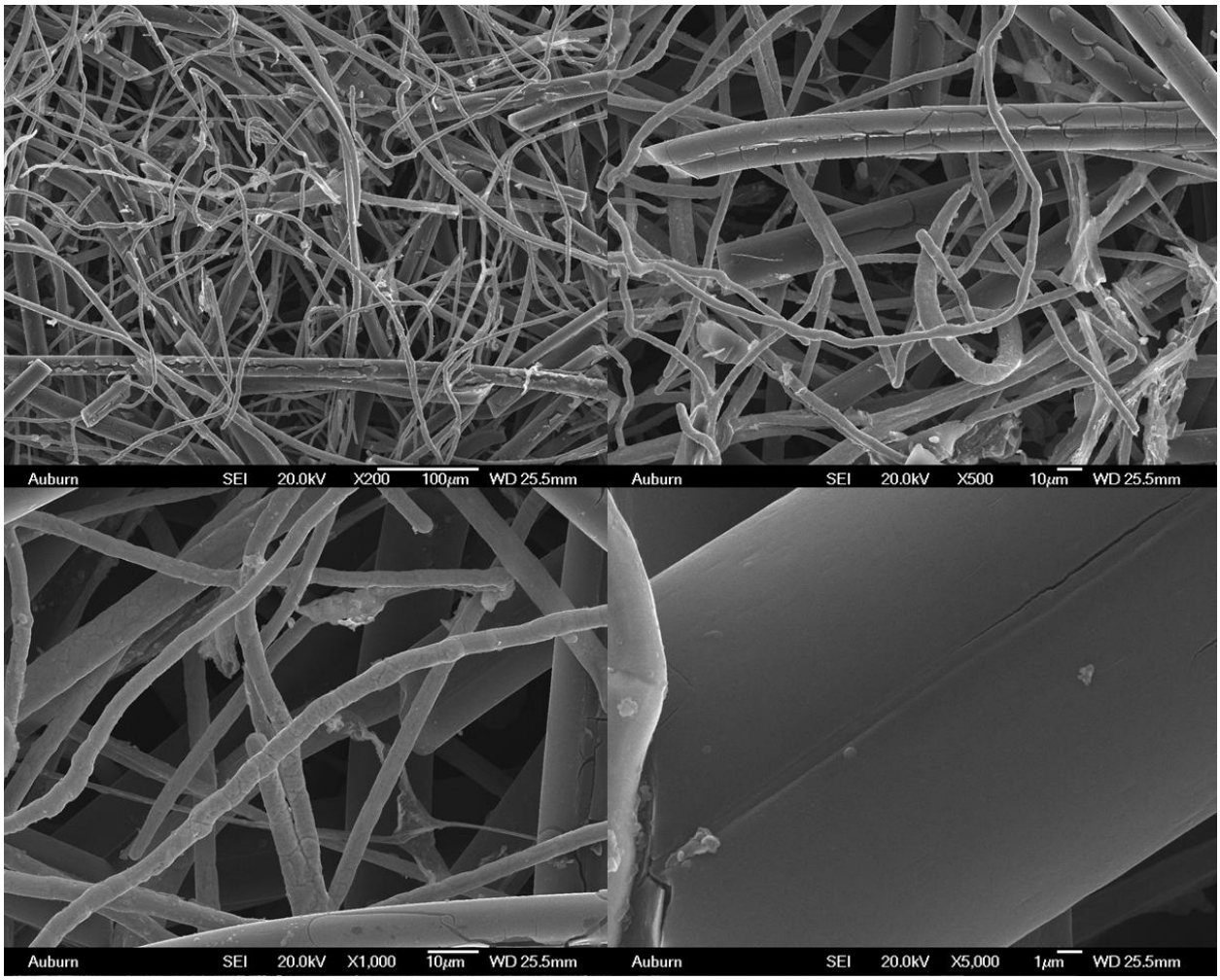

Figure 4.8 SEM of carbon fiber electrode before deposition.

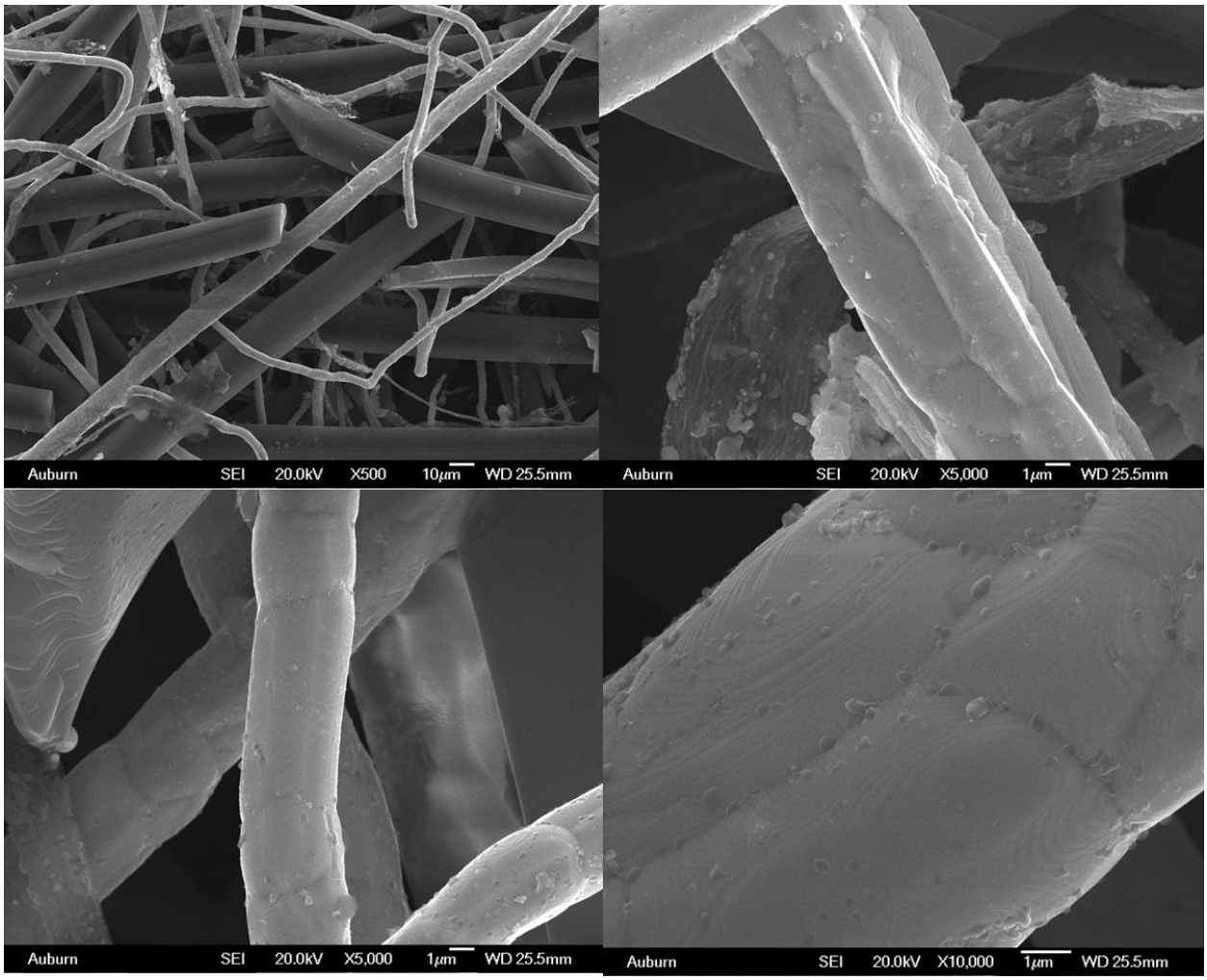

Figure 4.9 SEM of the carbon fiber material with the Mn_3O_4 deposition.

A)

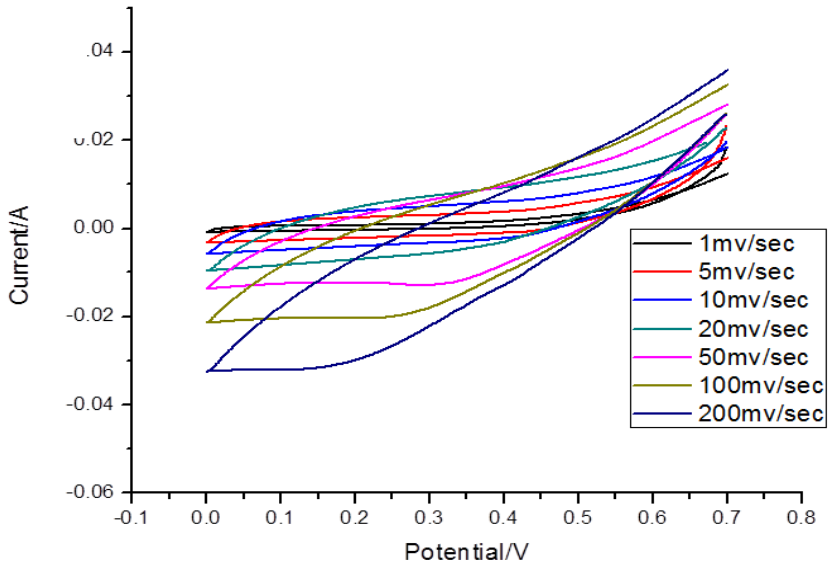

B)

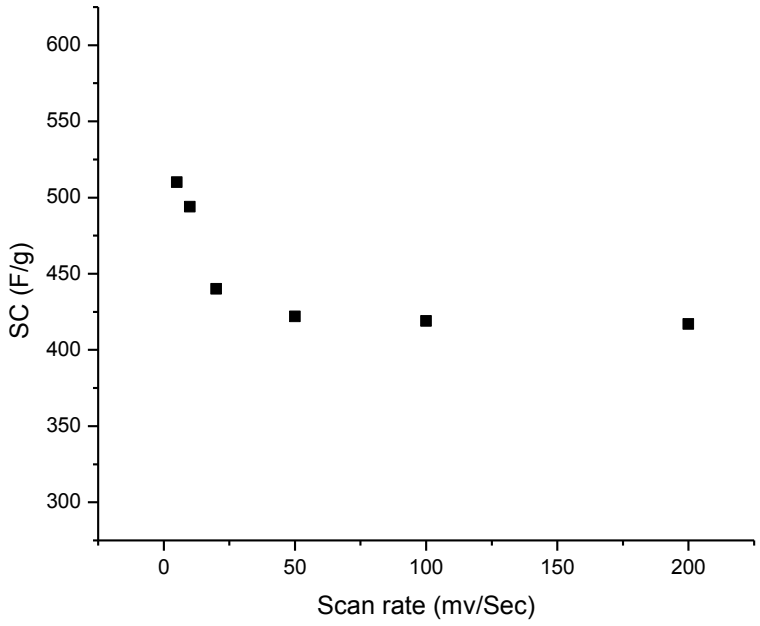

Figure 4.10 CV measurements of the hybrid materials Mn_3O_4 on carbon fiber electrode.

A)

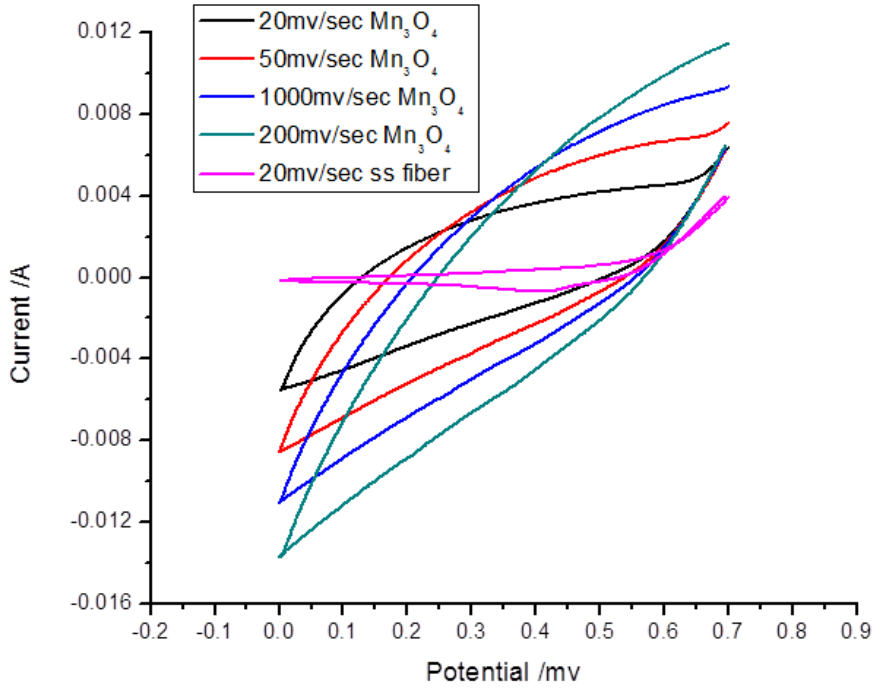

B)

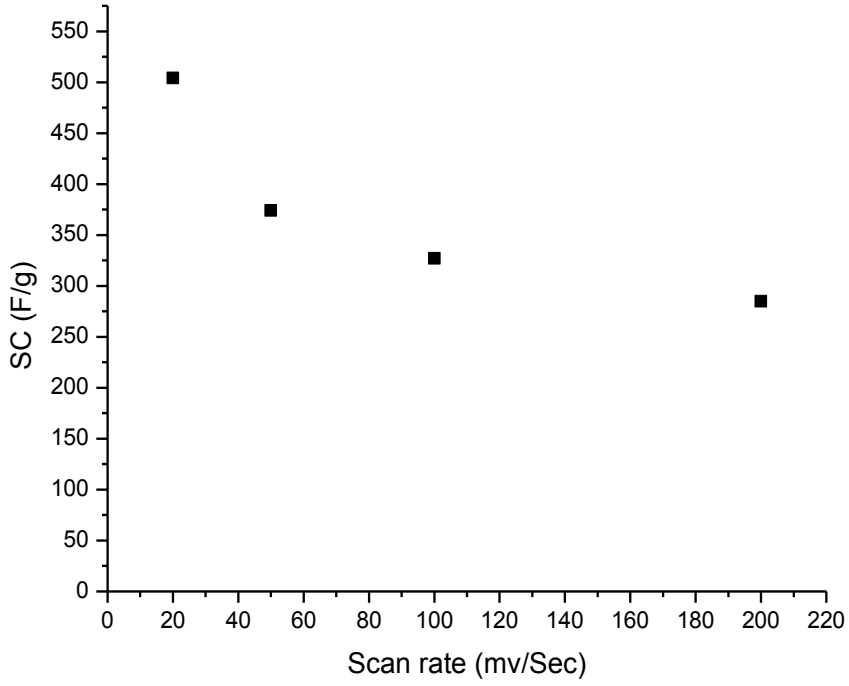

Figure 4.11 CV study of stainless steel mesh before Mn_3O_4 deposition (Blank curve). CV study of hybrid material Mn_3O_4/stainless steel fiber with different scan rates.

A)

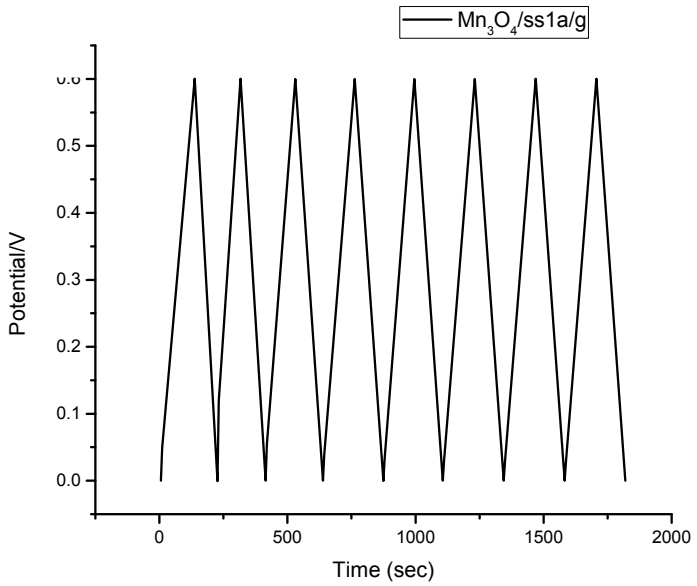

B)

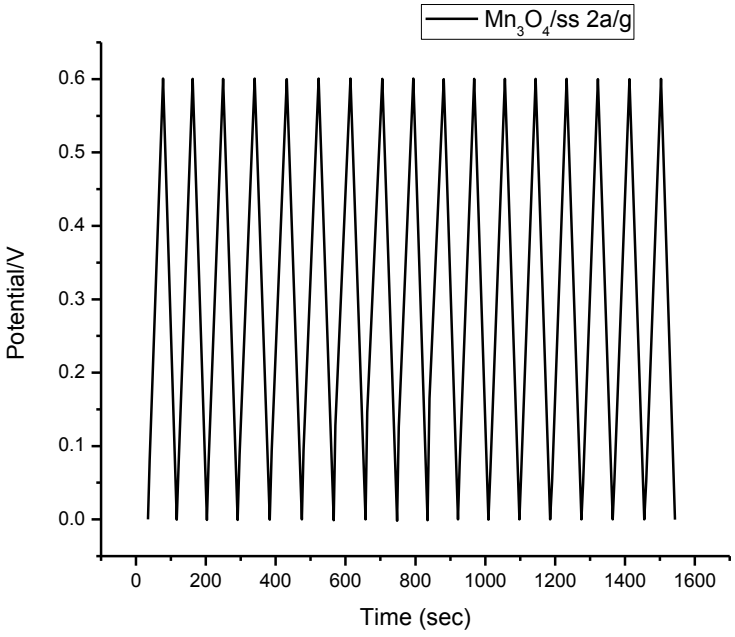

Figure 4.12 Charging and discharging of Mn_3O_4/stainless steel fiber electrode, A) current density 1A/g, and B) 2A/g.

A)

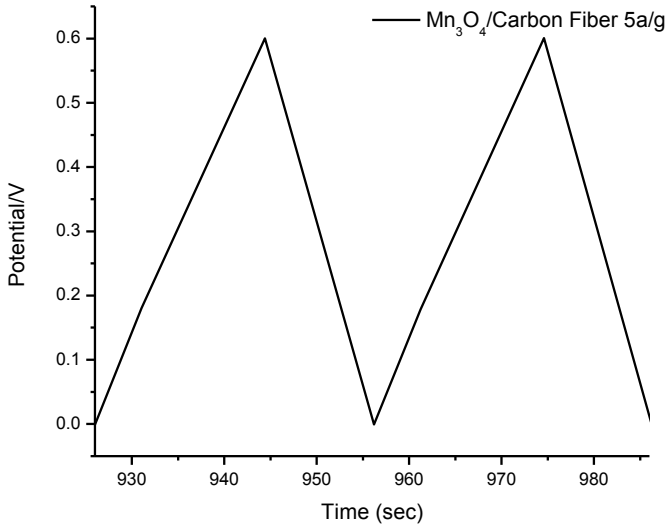

B)

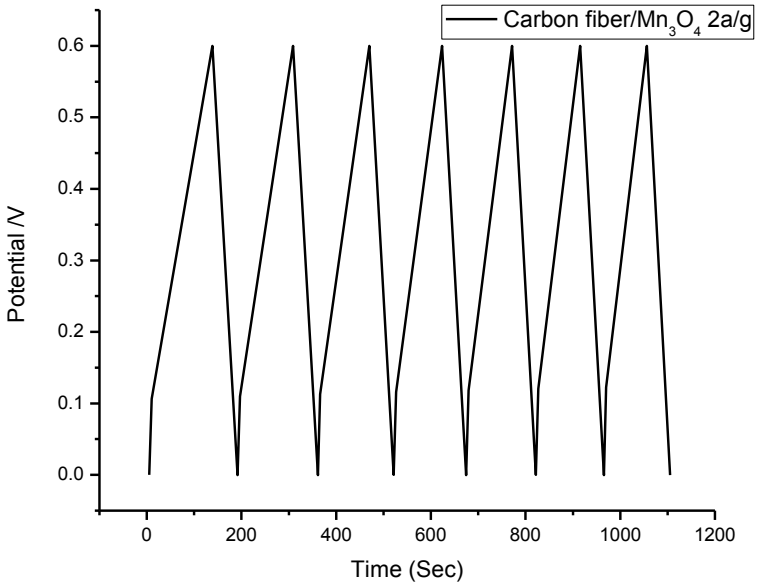

Figure 4.13 Charging and discharging of the hybrid material Mn_3O_4/Carbon fiber with current density A) 5A/g, and B) 2A/g.

References

[1] Chu, A.; P. Braatz. *J. Power Sources* **2002**, *112*, 236.

[2] Burke, A. *J. Power Sources* **2000**, *91*, 37-50.

[3] Niu, C.; Sichel, E. K.; Hoch, R.; Moy, D.; Tennent, H. *Appl. Phys. Lett*. **1997**, *70*, 1480.

[4] Gamby, J.; Taberna, P. L.; Simon, P.; Fauvarque, J. F.; Chesneau, M.; *J. Power Sources* **2001**, *101*, 109.

[5] An, K. H.; Jeon, K. K.; Heo, J. K.; Lim, S. C.; Bae, D. J.; Lee, Y. H. *J. Electrochem. Soc.* **2002**, *149*, A1058.

[6] Zheng, J. P.; Cygan, P. J.; Jow, T. R. *J. Electrochem. Soc.* **1995**, *142*, 2699.

[7] Yu, G.; Hu, L.; Vosgueritchian, M.; Wang, H.; Xie, X.; McDonough, J. R.; Cui, X.; Cui, Y.; Bao, Z. *Nano Lett.* **2011**, *11*, 2905.

[8] An, G.; Yu, Ping.; Xiao, M.; Liu, Z.; Miao, Z.; Ding, K.; Mao, L. *Nanotechnology* **2008**, *19*, 275709 .

[9] Jurewicz, K.; Delpeux,S.; Beguin, F. *Chem. Phys. Lett.* **2001**, *347*, 36.

[10] Lu, W.; Hartman, R. *J. Phys. Chem. Lett*. **2011**, *2*, 655.

[11] Jiang, J.; Kucernak, A. *Electrochim. Acta*, **2002**, *47*, 2381.

[12] Wu,Y.; Hu, C. *Electrochem. Solid-State Lett.* **2005**, *8*, A240.

[13] Djurfors, B. J.; Broughton, N.; Brett, M.J.; Ivey, D.G. *Acta Mater*. **2005**, *53*, 957.

[14] Djurfors, B. J.; Broughton, N.; Brett, M.J.; Ivey, D.G. *J. Mater. Sci.* **2003**, *38*, 4817.

[15] Pang, S.C.; Anderson, M.A. *J. Mater. Res.* **2000**, *15*, 2096.

[16] Chin, S.F.; Pang, S. Anderson, M.A. *J. Electrochem. Soc.* **2002**, *149*, A379.

[17] Broughton, J.N.; Brett, M.J. *Electrochim. Acta* **2004**, *49*, 4439.

[18] Rivas, B.L.; Geckeler, K.E. *Adv. Polym. Sci.* **1992**, *102*, 171.

[19] Zhitomirsky, I. *J. Appl. Electrochem*. **2004**, *34*, 235.

[20] Therese, G.H.; Kamath, P.V. *Chem. Mater*. **2000**, *12*, 1195.

[21] Nagarajan, N.; Humadi, H.; Zhitomirsky, I. *Electrochim. Acta* **2006**, *51*, 3039.

Chapter 5

5.1 Capacitance study of DNA SAM on gold surface

5.1.1 Introduction

DNA arrays are of great importance for DNA sensor and sequencing applications. Characterization of DNA molecules on substrate surface is essential for the improvement of these techniques. DNA molecules are often functionalized with alkyl thiols to enable immobilization on metal surface. The significance of the alkyl chain length on the immobilization density, intermolecular atmosphere, and geometry of the monomolecular assemblies has attracted particular scientific attention. It is widely accepted that methyl-terminated, long-chain n-alkanethiols can form a dense and well-ordered monolayer on gold electrodes [1]. The well-ordered SAM are based on the relatively high stability mediated by the strength of the Au-S (~50 kcal mol^{-1}) bond and by van der Waals force (~1–2 kcal mol^{-1} per CH_2 between hydrocarbon chains as reported) [2-3]. These monolayers are relatively stable under ambient conditions. Several studies have been performed concerning the characterization and manipulation of SAMs, among them SAMs of n-alkanethiols are most thoroughly studied.

In sensor applications, self-assembled monolayers of Mercaptohexanol are utilized to reduce the nonspecific sequences so that well-ordered monolayers can be formed and the background interference is reduced. In previous ECPA sensor studies, there has been a problem of large background noise of the signal. In order to reduce the background noise and thus to improve the sensitivity of the system, it is critical to obtain a more detailed understanding of the

structure-function relationship of surface-immobilized DNA. In this study, self-assembled monolayer of n-alkanethiols on gold electrode was utilized to extract information of DNA self-assembled monolayer. Electrochemical methods were used to characterize this system.

5.1.2 Experimental

Self-Assembly of monolayers on gold surface

The n-alkanethiols and DNA SAM assemblies were spontaneously prepared by immersing clean gold electrodes into diluted 1 mM n-alkanethiols or DNA solutions for 2 hours. Then modified electrodes were rinsed with plenty of distilled H_2O and dried with N_2. The chemicals used in the studies include hexanethiol(C6), octanethiol (C8), decanethiol (C10), octadecanethiol (C18), mercaptohexanol (MCH) and DNA sequence.

Electrochemical Measurements

All the cyclic voltammetry measurements were carried out with a three-electrode set up. The reference electrode was Ag/AgCl (Bioanalytical Systems, Inc.), the counter electrode was Pt gauze and working electrode was gold with diameter of 1.6 mm. The electrochemical circuit was controlled using an Epsilon electrochemistry workstation (Bioanalytical Systems, Inc.).

5.1.3 Results and discussion

Based on previous studies, well-ordered SAM was formed on a gold electrode by controlling the concentration of the solution and the incubation time. Differential capacitance rises with a decreasing separation between the electrode surface and the plane of closest approach for ionic charges. It also increases with increasing dielectric constant of the intervening medium in the electrochemical double layer system [4]. The capacitance depends on the capacitive current, the scan rate, and the electrode area as shown in Equation (1) below. Figure 5.1.1 displays the calculated capacitances of different monolayers assembled on the gold

electrode at different scan rates (10 mv/sec, 20 mv/sec, 50 mv/sec, 100 mv/sec, and 200 mv/sec). The top curve in the plot illustrates the capacitance of bare gold electrode. The capacitance depends on the capacitive current, scan rate, and electrode area, as shown in Equation (1).

$$\boldsymbol{I = 2cv} \qquad \textbf{(1)}$$

As with a capacitor, the capacitance of the electrode decreases with the increasing scan rate. The capacitance of different assembled monolayer depends on the length of the molecule, and decreases with increasing length of the SAM on the surface. The capacitive current at n-alkanethiols covered Au electrode less than that of bare gold by a factor of 20. The behavior of these electrodes is in agreement with the Helmholtz theory for the EDL [5], which models the theory of electrochemical interface as an ideal capacitor.

The Helmholtz theory models the double layer as an ideal capacitor as described in the first chapter [6]. The reciprocal of the capacitance is related with the thickness of the dielectric medium as shown in Equation (2) below:

$$\boldsymbol{C^{-1} = d / \varepsilon\varepsilon_0} \qquad \textbf{(2)}$$

where d is the thickness of the dielectric medium that separates the two conducting plates, ε is the dielectric constant of the separation medium, and ε_0 is the permeativity of free space. The equation shows that the capacitance is directly proportional to ε and inversely proportional to d. Although there are some constraints of the theory such as the electrolyte and applied potential, the behavior of these SAM-modified electrodes is consistent with that predicted by the Helmholtz theory. As plotted in Figure 5.1.2, there is a linear relationship between the reciprocal of the capacitance of alkanethiols assembled electrodes and the thickness of the dielectric separated by the different alkanethiols' length with a slope of $1/\varepsilon\varepsilon_0$. By linear fitting of the data, the relationship between the slope and intercept was obtained. From the average slope of the line,

ε can be calculated. The calculated value of the dielectric constant was found to be 2.1, which is close to the reported values [7]. This result indicated that these self-assembling monolayers can act as a dielectric medium in a capacitor.

The behavior of the mercaptohexnol (MCH) and thiolated DNA sequence assembled electrodes was also studied and the result is shown in Figure 5.1.3. The mercaptohexnol shows similar capacitance behavior due to their similar structures. However, with an additional -OH group on one end, mercaptohexnol has a smaller capacitance than hexnethiol. This difference can be explained by the fact that the hydrophobic property of the –OH on the electrode surface facilitates for the electron transfer and accordingly, which in turn reduces the thickness of the dielectric double layer, resulting in a smaller capacitance.

Finally, as shown in Figure 5.1.3, a thiolated DNA sequence with a much longer length showed comparable capacitance to both decanethiol and octadecanethiol. This can be explained by the fact that DNA sequence is negatively charged, making it easy for the positively charged electrolyte ions to penetrate the SAM and reside closer to the gold surface, which can reduce the effective distance (d_{eff}) and thereby reducing the capacitance as described in Figure 5.1.4. The capacitances of these modified gold electrodes are summarized in Table 5.1.1. Comparing with previous reported numbers, these capacitances show comparable numbers but a little bit higher capacitances due to different electrolytes.

The capacitance of DNA SAM on electrode surface was studied. However, in order to improve the sensor, a detailed characterization of structure-function relationship of the surface-immobilized DNA is needed.

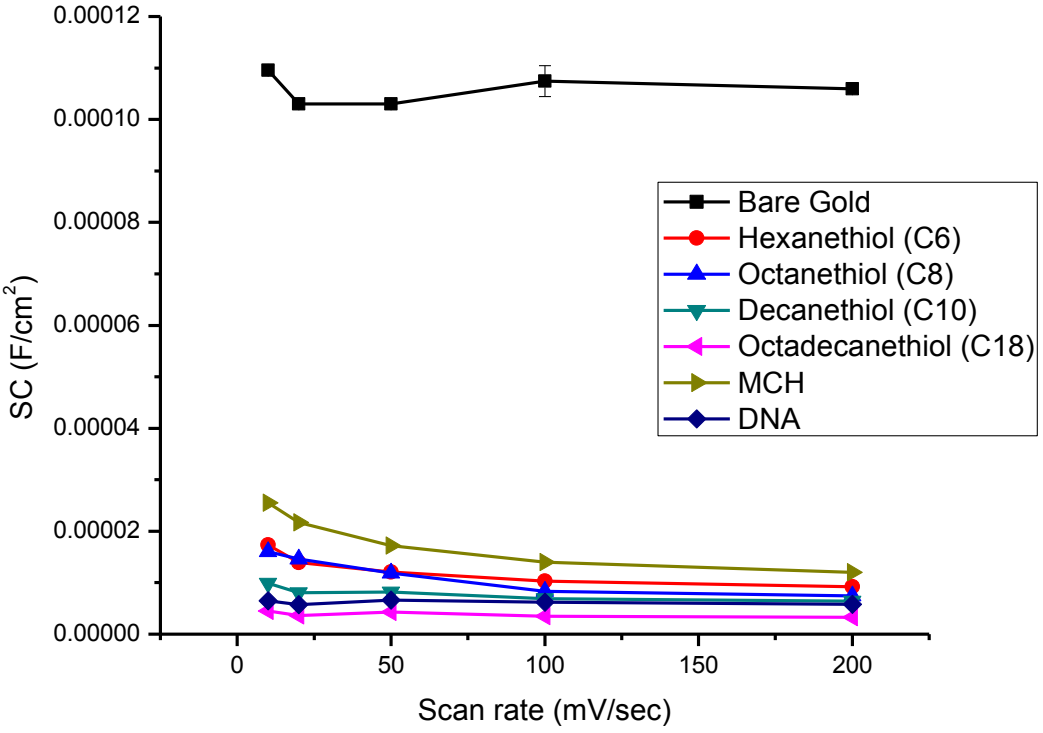

Figure 5.1.1 Calculated capacitance of different monolayer assembled gold electrode at different scan rates (10mv/sec, 20mv/sec, 50mv/sec, 100mv/sec, and 200mv/sec). Top one is the bare gold electrode.

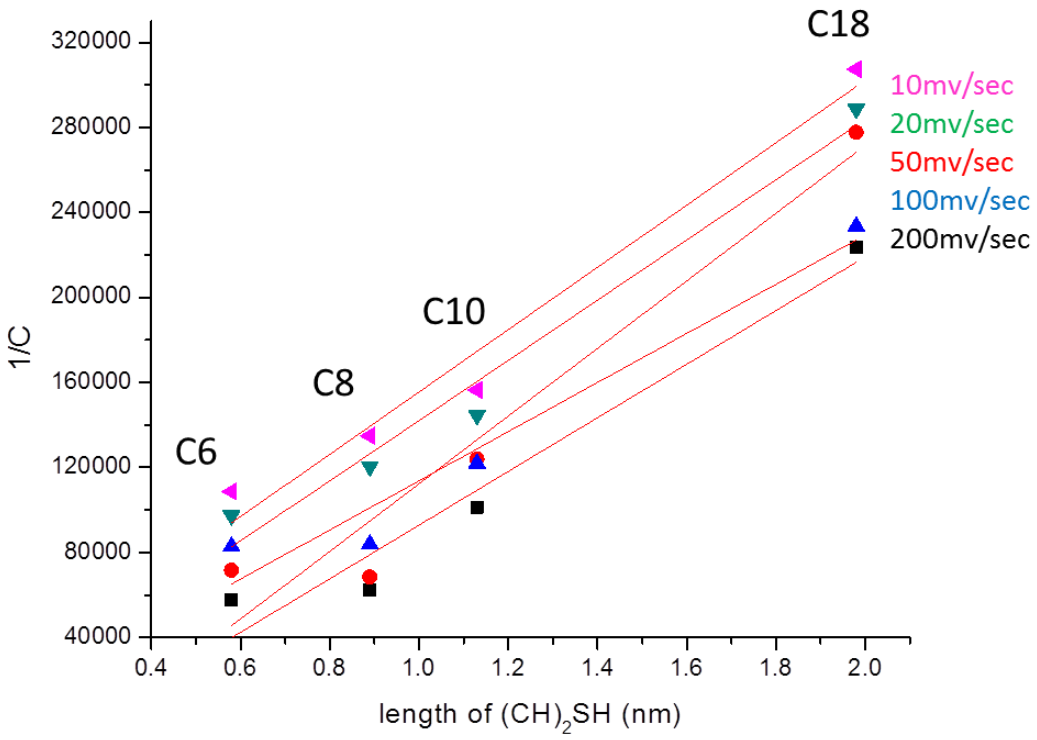

Figure 5.1.2 Linear relationship between reciprocal of the capacitance of different alkanethiols assembled electrodes with the space length separated by alkanethiols self-assembled monolayer.

Self-assembled monolayer	Capacitance (F/cm^2) (This work)	Reported numbers (Ref below)
Hexanethiol (C6)	$9. \times 10^{-6}$ ($NaClO_4$)	$(2.5\text{-}3.5) \times 10^{-6}$ (NaOH)
Octanethiol (C8)	7.41×10^{-6}	2.2×10^{-6} (NaCl+PBS)
Decanethiol (C10)	6.39×10^{-6}	1.7×10^{-6} (NaCl+PBS)
Octadecanethiol (C18)	3.4×10^{-6}	1×10^{-6} (NaCl+PBS)
Mercaptohexanol (MCH)	1.1×10^{-5}	$(4.9\text{-}6) \times 10^{-6}$ (PBS buffer)
DNA	5.77×10^{-6} (36 bp)	~2.5×10^{-6} (15 bp) (PBS buffer)

Table 5.1.1 Capacitances of self-assembled monolayer modified electrodes in this work and reported numbers [38-40].

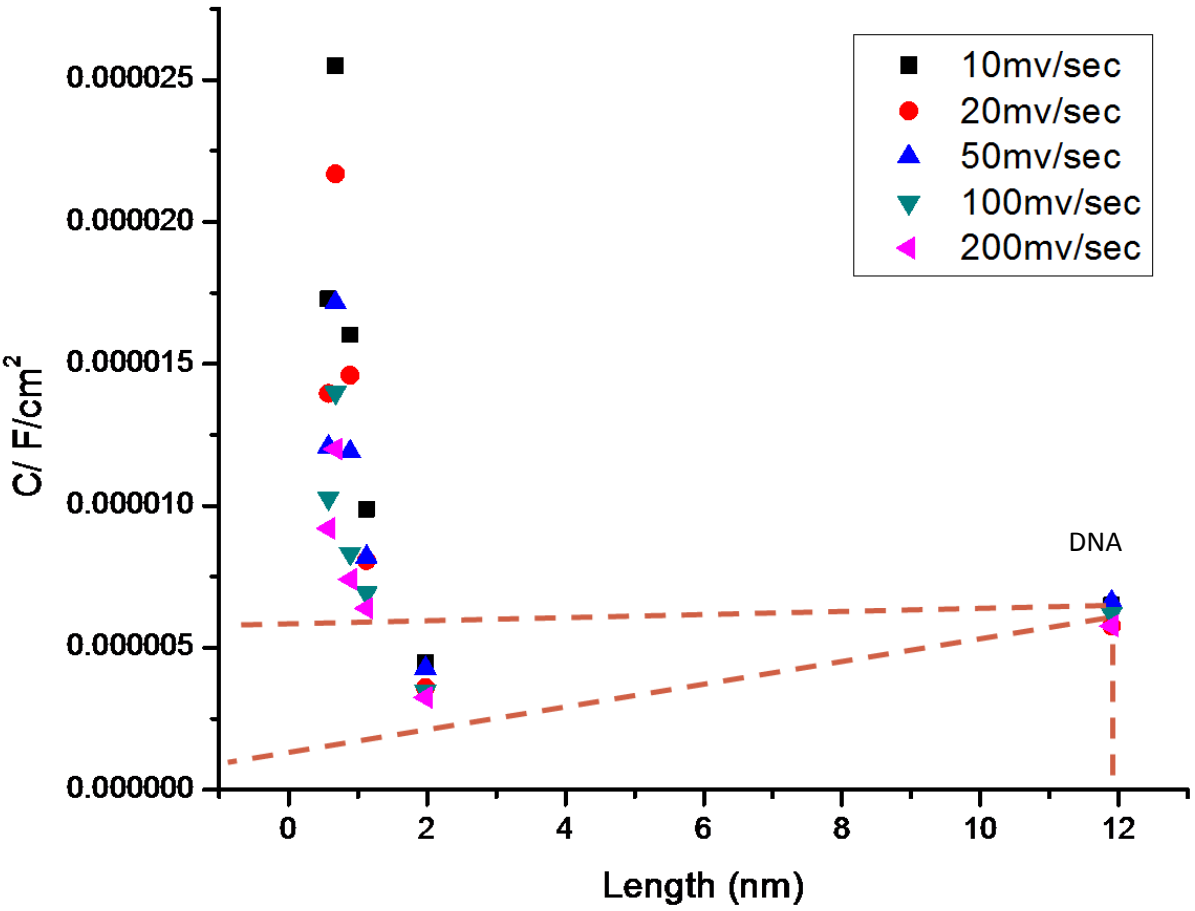

Figure 5.1.3 The relationship between the capacitance of different alkanethiols, mercaptohexanol and thiolated-DNA assembled electrodes with the space length separated by those self-assembled monolayer. All of them are represented by five different scan rates.

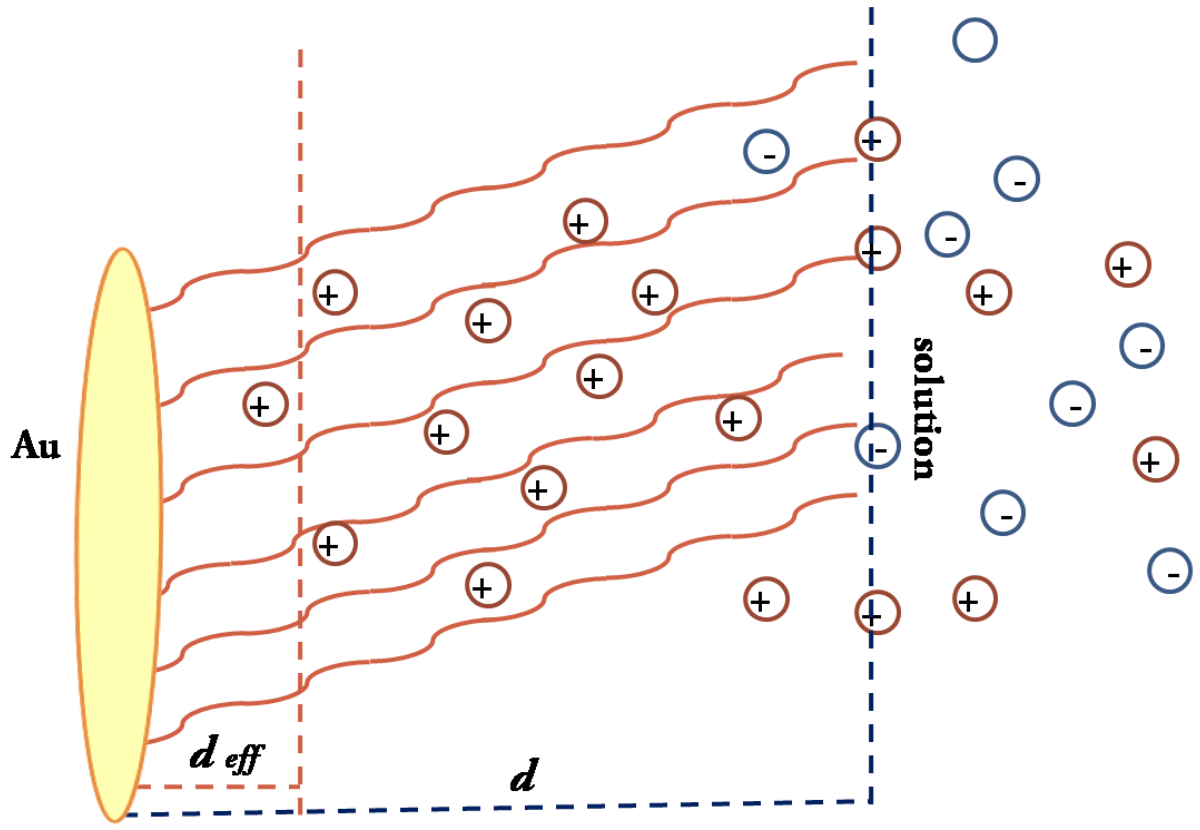

Figure 5.1.4 Helmholtz model of DNA and alkanethiol SAM modified gold electrodes.

5.2 Fast, reusable and sensitive electrochemical proximity assay for protein detections

(Collaboration work with Jiaming Hu from Dr. Easely's group)

5.2.1 Introduction

Early medical diagnosis of critical health changes enables the prevention of death and ensures appropriate and timely care and treatment to patients [1-4]. Highly sensitive detection and accurate analysis of disease-associated proteins are required for early diagnosis [5-7]. Current standard detection methods such as Western blots and enzyme-linked immunosorbent assays (ELISA) are usually slow and cumbersome. These laboratory-bound processes require at least several hours or days to obtain the clinical information [6]. Point-of-care analysis could overcome these drawbacks and speed treatment processes, and thus improve patient treatment outcomes [2, 7-11]. As a promising technology, point-of-care analysis can highly improve the early diagnosis and on-site monitoring of disease by offering useful information to doctors and clinics [12-13]. Moreover, point-of-care technology can be used in poorly equipped testing laboratories without the need of specialists. This will ensure diagnosis within a short period of time and at low cost [14-15]. However, certain challenges must be overcome concerning the laboratory sensor development for point-of-care application [16, 17]. First of all, the biosensor must be very selective in order to reject false signals. Secondly, it must operate incessantly without batch process steps, such as separations. Thirdly, it must be fast and highly sensitive. In addition, the sensors must be reusable since reusability is a very important factor that could greatly reduce the cost of the product.

A lot of studies have been carried out to develop point-of-care devices. These include optical, electrochemical, piezoelectric, thermal or electrical methods [18-22]. With the development of biosensing techniques, DNA-based electrochemical sensors have become more promising towards point-of-care application due to their rapidity, and low-cost on-field detection. They are particularly suitable for miniaturized devices, and for application in chemically complex environments, such as blood serum [23-24]. Various designs for such sensors have been published. These include electrochemical DNA (E-DNA), traditional sandwich/supersandwich assays, competition-type assays, electrochemical aptamer-based sensors (E-AB), double-antibody sandwich assays, and aptamer-based sandwich assays [25-29]. Generally, DNA-based electrochemical sensors are fabricated by labeling an electro-active reporter on one end of the DNA sequence which can undergo redox reactions on the electrode surface, thus inducing electrochemical signal change. The principles could be based on target-induced strand displacement mechanism, analyte-induced conformational change, or combination with sandwich and competition assays, by forcing redox-labeled DNA into the proximity of the electrode surface [26].

Motivated by the point-of-care application, the first generation of electrochemical proximity assay (ECPA) was successfully developed by Hu *et al.* for detection of proteins [30]. This sensor uses the proximity effect to move an electrochemically active label, methylene blue (MB), closer to a gold electrode upon binding of two probes to a protein target. The technique exhibits very high sensitivity and selectivity [31]. By combining the double-antibody-oligo sandwich assay and the aptamer-based sandwich assays with DNA-based electrochemical sensor, ECPA provides a direct insulin detection limit that is lower than most commercially available ELISAs, with a dynamic range >40-fold wider than these ELISAs. Because of its intrinsic

flexibility, ECPA has the potential to detect various proteins. It can be further developed to allow multiplexing detection using an electrochemical microarray. In addition, because of the high sensitivity and selectivity, it is very promising for point-of-care applications. However, in the work of Hu *et al.*, the ECPA sensor is not reusable, and long detection times are required to avoid the background interference.

One common way to make a reusable biosensor assay is to rinse the device with water after use [26, 33, 34]; However, this reusable method has some deficiencies. First of all, it is only useful for dsDNA with little base-pairs. If two DNA strands have more complementary bases, forming hairpin structure or creating complex structures by proximity effect of three or more DNA strands binding together, the sensors cannot be regenerated by simple rinsing. Secondly, water rinse can cause signal decrease. However, signal decrease is not sufficient to prove the sensor is regenerated, because the dsDNA sequence may not be denatured and target molecules may still remain attached on the surface.

To overcome all these problems, a new regeneration method was accomplished in this study by incorporating uracils into selected probe strands that can be cleaved enzymatically. These strands can be cleaved into short DNA pieces (< 6 oligonucelotides) by Uracil-DNA excision mix that can easily diffuse into liquid solutions at 37 °C, or even at RT. Also, in order to achieve direct detection of unprocessed samples such as animal blood, which is required for applied products, ECPA sensor cyclic assembling methods were optimized. Several developments were accomplished in this study. For instance, by using the Uracil sequence design along with Uracil enzyme, the ECPA system was regenerated about 20 times with excellent signal recovery and selectivity. Moreover, the sensor exhibits a faster detection time window of three minutes at body temperature. Co-immobilization of the thiolated DNA probe with a back-

filler (mercaptohexanol [MCH] used in our system) was employed to reduce the background noise. Based on these developments, a fast, sensitive and reusable ECPA sensor was successfully developed and higher sensitivity for insulin detection was accomplished. Insulin detection from pancreatic islets and direct detection of insulin form mouse blood serum are realized.

5.2.2 Experimental

Chemicals and Oligonucleotides

Methylene blue-conjugated DNA (MB-DNA) was purchased from Biosearch Technologies (Novato, CA), purified by RPHPLC. Other DNA oligonucleotides were synthesized by Integrated DNA Technologies (IDT; Coralville, Iowa). Additionally, 6-mercapto-1-hexanol (97%), 4-(2-hydroxyethyl)-1-piperazineethanesulfonic acid (HEPES) (99.5%), tris-(2-carboxyethyl) phosphine hydrochloride (TCEP), human thrombin, immunoglobulin E (IgE), and insulin were obtained from Sigma Aldrich. Bovine serum albumin (BSA, 98%; EMD Chemicals Inc) were used as received. HEPES/$NaClO_4$ buffer (10 mM HEPES and 0.5 M $NaClO_4$, pH 7.0) was prepared for all the solutions using deionized, ultra-filtered water (Fisher Scientific). Table 5.1 shows all the oligonucleotides (listed 5' to 3') used in the study.

Sensor fabrication

Gold electrodes were cleaned before use according to the following procedure. First, the electrode was immersed into fresh piranha solution (H_2SO_4/H_2O_2, 3:1 Vol) for 30 minutes, then rinsed with D. I. water and ethanol, and dried under a stream of nitrogen gas. Next, the electrode was polished carefully to a mirror surface with aqueous alumina slurry of 0.05 μm diameter and then sonicated for 15 minutes in the mixture solution of ethanol and water. After that, the gold

electrode was treated with fresh piranha solution for another 20 minutes. Finally, the gold electrode was electrochemically cleaned by redox process of cyclic voltammetry in 0.1 M H_2SO_4 at a scan rate of 100mv/sec for 12 cycles.

Uracil-DNA Excision Mix is used for restoring the system. Uracil-DNA Excision Mix consists of two enzymes, HK™-UNG (Heat-Killable Uracil N-Glycosylase [UNG]) and Endonuclease IV. First, HK-UNG can cleave the uracil base from a uracil-deoxynucleotide in any DNA sequences, creating an abasic spot at the location of dUTP incorporation. Endonuclease IV then cleaves the phosphodiester bond at this abasic location to generate a series of digestion fragments.

Prior to the modification of the electrode, thiolated-DNA was incubated in TCPE for 2 hours at room temperature to allow reduction of disulfide bonds in the thiolated-DNA and the MB-moeity of the MB-DNA. The solution was then diluted to a final concentration of 1 μM to prepare the self-assembled-DNA monolayer. This was done by incubating a gold electrode in the solution overnight ~16 hours at room temperature in the dark. After incubation, excess thiolated-DNA physically adsorbed on the electrode surface was removed with deionized water rinse (~ 20 s). After that, the electrode was immersed into 3 mM 6-mercapto-1-hexanol (MCH) solution in HEPEs buffer for 40 minutes, followed by rinsing thoroughly with water (~1 minute). For the non-cyclic assembling process, the DNA-modified electrode was transferred into solution with either antibody-oligo or aptamer sequences with MB-DNA for SWV measurement. For the cyclic assembling process, the pretreated electrode was incubated with 1μM 10μL thrombin aptamer A or insulin antibody arm 1 for 3 minutes, then rinsed with washing buffer. After that, the electrode was incubated in thrombin or insulin solution for 3 minutes, followed by drop incubation with 1μM, 10μL thrombin aptamer B or insulin antibody arm 2 for 3 minutes. The

electrodes were rinsed by washing buffer between the assembling. After the measurement, the electrode was incubated into 1µL Uracil-DNA excision mix for 7 minutes under 37 ^{o}C for regeneration. Detailed fabrication processes are described below.

In the model system experiments**,** the pre-modified electrode was transferred into a glass electrochemical cell with HEPES/$NaClO_4$ buffer. The modeling signal of the sensor was measured using 10 nM ECPA-loop and 15 nM MB- DNA. Solutions of 15 nM MB-DNA were used for the background detection. In the Aptamer-Based reusable ECPA System, seven gold working electrodes were used for signal measurement. Thrombin of seven different concentrations was incubated with 10 nM thrombin aptamer A and 15 nM thrombin aptamer B in HEPES/$NaClO_4$ buffer for the SWV measurements. After measurement, each sensor was regenerated by incubating in enzyme solution for 7 minutes at 37 °C. The enzyme solution was prepared with 2 unit uracil DNA excision mix in 100 µl uracil excision enzyme buffer (50 mM Tris-HCl (pH=9.0), 10 mM EDTA and 20 mM $(NH_4)_2SO_4$). Then the enzyme solution and cleaved DNA freagments on electrode surface were removed by flushing with D.I. water for about 30 seconds. Finally, the electrodes were dried under N_2 gas. The sensor was then ready for measurements.

The detections of insulin secretions from pancreatic islets using antibody-oligonucleotide conjugates were performed using the cyclic approach. First, the sensor was incubated with 50 nM DNA conjugated antibody 1(AbArm1−3A6) for 3 minutes by dropping 10 µL solution on the sensor surface. After that, the electrodes were washed gently with washing buffer (HEPES/$NaClO_4$ PH=7) for 15 seconds. Next, the sensor was transferred to pancreatic islets solution kept at 37 °C by temperature controlled heat block for 3 minutes following with rinsing with washing buffer. After that, 50 nM Ab2 (DNA conjugated antibody 2: AbArm2−8E2) was

drop coated on the gold surface for another 3 minutes. Finally, the electrode was transferred to solution for electrochemical measurements.

Electrochemical Measurements

Electrochemical measurements were performed using a Gamry reference 600 potentiostat with a standard three electrode setup consisting of a Ag/AgCl reference electrode (Bioanalytical systems, Inc.), a homemade platinum gauze flag (0.77 cm^2) counter electrode, and a gold working electrode (CH Instruments, Inc. r=1mm). All potentials are measured with reference to the Ag/AgCl reference electrode. Electrochemical measurements were carried out using square wave voltammetry (SWV) over the potential window from -0.45 V to 0.00 V under the set-ups of 50 mV amplitude, 60 Hz frequency. The specific oxidation peak of MB was detected by SWV at -210 mV in the system.

5.2.3 Results and discussion

Reusable ECPA principle

Figure 5.1 demonstrates the principle of the reusable electrochemical proximity assay (ECPA). The sensor was fabricated by self-assembly of thiolated DNA strands onto a gold electrode through the reaction of the alkanethiol moiety at the 5' terminus with the gold surface (Au-S). Then 3mM MCH was co-immobilized as backfiller to remove the nonspecific sequences on the surface [35, 37]. As mentioned earlier, mixed self-assembled monolayers of thiolated DNA sequences and thiol compounds have been widely used to control the surface density, the orientation, distribution, and the steric hindrance in order to improve the binding efficiency [37]. The sensor complex consists of five parts as shown in Figure 5.2.1A: thiolated DNA, Ab1 sequence, target protein, Ab2 sequence, and MB DNA. In the system, uracil bases are incorporated into complementary parts of Ab1 and MB conjugated DNA for thiolated DNA as

depicted in Table 5.2.1. The regeneration mechanism is shown in Figure 5.2.1 B. The Ab1 and MB conjugated DNA are enzymatically cleaved into three and two small DNA pieces separately using a uracil-DNA excision mix. After that, excess enzyme solution and DNA pieces can be removed by rinsing thoroughly with D.I. water.

Reusable ECPA Model system

Fast measurements are required for an ideal sensor design. In the first generation of ECPA study [30], the signal measurement time of DNA-based experimental model was 40 minutes. Three complementary bases: G5, G7 and G10 were compared. It was found that G5 system has the lowest background current but with a large signal reduction. The G10-competitor system had a large signal current background; however, in order to avoid the big current noise, a long time was needed for the signal detection.

In order to cut the measurement time, three different systems were compared as shown in Figure 5.2.2. Based on previous study, it is expected that the G5 system will be more suitable for the study due to its low background signal. However, additional optimizations are required to enhance the signal. Several optimizations were made including improving the concentrations of MB-DNA. The concentration of 50 nM was used in G5, G7, and G10-competitor systems. In the G5 system, because the binding between G5 and MB-DNA was very week at room temperature, the higher amount of MB-DNA did not affect the background significantly. However, the signal intensity can still be obtained due to the proximity effect discussed in previous works [30, 32]. The signal and background responses of the G5, G7, and G10-competitor systems were compared as shown in Figure 5.2.2. As hypothesized, the background current of G5 system was still kept at low levels while signal current was increased compared to the previous G7 and G10

systems. Because of more complementary bases in the thiolated DNA of G7 and G10, the stronger hybridization energy speeded up the complex formation, which gave a relatively large background current. Even under the conditions of short DNA competitor or higher concentration of MB-DNA, both signal and background formed rapidly in G10 system. Therefore, G5 is the most suitable design for the reusable studies. Another advantage of the G5 is that it greatly simplified the fabrication of the system because no competitor is required.

The uracil enzymatic regeneration method was compared with different commonly used methods as shown in Figure 5.2.3. The red plot in the figure represents the current signal measured at 3 minutes after the electrode incubation. For the SWV measurement, 10 nM thrombin with 10 nM THRaptA, 15 nM THRaptB and 50 nM MB-DNA in the buffer solution were used. According to the literature, sensor regeneration can be accomplished with either water rinsing or thermal de-hybridization such as using washing solution with relatively high temperature [33]. However, there are some limitations to these methods such as incomplete de-hybridization for double strand DNA with long complementary stem. In the ECPA system, three methods were compared with the enzymatic regeneration approach including D.I. water rinsing at RT and water/warm buffer rinsing at 37 °C as shown in the figure. The pink curve shows the signal from the electrode after 7 minutes incubation in HEPES/$NaClO_4$ buffer at 37 °C. The green curve is signal after immersing the sensor in 37 °C warm water for 7 minutes and the regeneration result of water rinse is shown in blue curve. It can be seen that these methods do not lead to complete regeneration in our system. The signal current goes down to 80% of original value after using 7 minutes washing buffer at 37 °C. The current value is about 35% of original one when using the water flow rinsing with 65% denaturation achievement. After immersing the sensor in warm water at 37 °C for 7 minutes, 80% denaturation of cooperative complex was

achieved. None of these methods can completely regenerate the ECPA system because several sequences are incorporated in the signal ECPA system which can have stronger energy under the loop structure. The black line represents the regeneration result using uracil-DNA enzyme. The result shows almost 100% denaturation of the system.

Reusable ECPA for thrombin detection

A schematic of aptamer-based reusable ECPA for thrombin detection is shown in Figure 5.2.4A (insert). Two thrombin binding aptamers (TBA) (THRaptA, THRaptB) are used in the system to form a sandwich structure. Background measurement without thrombin is shown in the black curve in Figure 5.2.4A. Seven electrodes were prepared for the experiment. Seven various concentrations of thrombin (from 0 to 10 nM) were measured by each sensor. Typical MB oxidation peaks showed at −210 mV in the presence of various amounts of thrombin measured at 3 minutes time window. In this experiment, each sensor was regenerated seven times using 7 electrodes. The calibration curves are shown in Figure 5.2.4B. The solid line curve with error bar is the average value of 7 sensors.

Two sensors with two different concentrations (1.25 nM, 5nM) of thrombin were chosen to investigate the duration of regeneration. As shown in Figure 5.2.4C, the regenerated signal of both sensors remains almost 100% recovery with 19 cycles of regeneration by uracil-DNA excision enzyme.

To demonstrate specificity and signal reproducibility, the reusable ECPA was studied with nonspecific proteins including human IgE, insulin, and BSA as shown in Figure 5.2.4D. The graph shows that essentially little current signal was detected in the presence of IgE (15 nM) or insulin (15 nM) even with higher concentration. Almost no current was detected in the

presence of 3% BSA in 5 nM thrombin solution. In addition, no response was observed in the presence of 3% BSA. These results show that the ECPA sensor has excellent selectivity even after the regeneration cycles.

Reusable ECPA for insulin detection

In the ECPA system, two antibody-oligonucleotide conjugates are used to form a sandwich conformation after binding insulin. As mentioned earlier, in the ECPA system two aptamers are required for the target protein detection. However, since aptamer pairs are present for only a few proteins, the flexibility of the aptamer-based approach is limited. The use of antibody-oligonucleotide conjugates can be used as probes to overcome these challenges because antibody /antigen are readily available [35, 36].

The principle of antibody-based reusable ECPA is demonstrated in Figure 5.2.5A. In this experiment, several optimizations were achieved. First, the cyclic protocol was utilized in order to improve the potential of the sensor to be used for a real sample such as blood serum. Moreover, the temperature of insulin incubating solution was kept at 37 °C which is the same as secretion sample measurements from pancreatic islets and body temperature. In addition, higher concentrations of sequences were used to improve the sensitivity with 50 nM antibody-oligo and 50 nM MB-DNA. Typical MB oxidation peaks appear at −210 mV in the presence of various amounts of insulin as shown in Figure 5.2.5 B. The calibration curves with different insulin concentration are also shown. The detection limit of ECPA system can reach 100 fM with a wide dynamic range up to 6.25 nM.

The regeneration times of the ECPA were investigated and the result are shown in Figure 5.2.6 A. It was found that antibody-based reusable ECPA can be regenerated about 18 times

without losing the sensitivity. Selectivity of antibody-based reusable ECPA was studied against insulin-like growth factor 1 (IGF-1) and C-peptide. IGF-1 and C-peptide were chosen because IGF-1 has a very similar structure to insulin and C-peptide is usually released with insulin into bloodstream. As expected, the sensor did not respond even to higher concentrations of either IGF-1 or C-peptide as shown in Figure 5.2.6 B.

Measurement of Insulin secretion from pancreatic islets

Before the measurement of the blood sample, experiments are performed in order to monitor insulin secretion from endocrine tissues. In this study, the sensor fabrication process was optimized in order to reject the false signal from complicated sample as shown in Figure 5.2.7A. As mentioned earlier, the cyclic assembling methods are fabricated as follow for simplicity. First of all, 10 µL of Ab1 solution was dropped on the gold surface with SAM of thiolated DNA and incubated for 3 minutes. Then the electrode was transferred into pancreatic islets solution. Next, 10 Ab2 µL was drop-coated onto the electrode surface with 3 minutes' incubation. After that, the electrode was transferred to the solution of 50 nM MB-DNA for the signal measurements. Finally, the electrode was incubated with uracil-DNA excision mix solution for 7 minutes at 37 °C to regenerate the sensor surface for next cycle. Between the incubations, the electrode was rinsed with washing buffer and D.I. water. During this experiment, pancreatic islets solution was kept at 37 °C (body temperature) for the assembling.

The results of insulin secretion measurements by the antibody-based reusable ECPA are shown in Figure 5.2.7B. In this experiment, solutions with 5 and 15 pancreatic islets were used. The islets were obtained from two different mice. The numbers of the islets can be counted using a microscope. Glucose was added from basal (3 mM) to stimulatory (11 mM) glucose levels.

More insulin was released at higher glucose level than the basal level. All the results are summarized in Figure 5.2.7B. As expected, the response signal from the solution with 15 pancreatic islets was almost 3 times higher than that from 5 pancreatic islets solution. The results were presented as the current changes by subtracting the previous signal from the current one. At the basal glucose level (3 mM glucose) as plotted as the first 3 data points, the current remained constant. After adding glucose to stimulatory glucose levels (11 mM glucose), large current changes were observed because more insulin was released. Signal changes were from 132 to 212 nA under 5 pancreatic islets, and from 266 to 505 nA and 272 to 491 nA under the 15 pancreatic islets solution. Compared to the calibration curve, quantitative insulin detection can be obtained during the continuous monitoring processes. The figure was plotted by integrating the area under the oxidation peaks from MB versus the times for the monitoring.

Insulin measurement from mouse Blood Serum

In this experiment, insulin measurements from mouse blood serum are reported. The cyclic approach for the sensor assembling was used in measurement of hormone secretions. The procedure is the same as the one in the islet experiment except that the blood serum was kept at 0 °C in order to reject the false signal from other enzymes and proteins in the mouse blood serum. It was found that, the temperature affects the selectivity of the system due to the fact that blood serum is made up of several components. One enzyme that can significantly affect the signal is the deoxyribonuclease (DNases), which catalyzes the cleavage of phosphodiester linkages within DNA backbone. By maintaining the temperature at 0 °C, the activity of DNases can be inhibited. Figure 5.2.8A shows that a single electrode can be reused ~9 times without loss of signal in 20-fold dilution of blood serum. As shown in Figure 5.2.8B, insulin detection from blood serum of two different mice (C57BL/6J) was measured. The solution of blood serum was diluted by a

factor of 20. Using standard addition method, the concentration of insulin in blood serum was measured as shown in the figure. By performing a linear fit to the addition curve, insulin concentrations were calculated to be 120 and 140 pM from blood serum samples obtained from two mice. The times of the reusability of the sensor in the blood serum were also studied as shown in the Figure 5.2.8A. It shows that the sensor can be regenerated about 10 times without significant loss of the signal. From literature, the normal concentration range of mouse blood is 16.4 ± 4.5 mU/ml (113.8 ± 31.2 pM). It was found that the detected concentration using ECPA sensor fell between the ranges. This finding shows that ECPA sensor can be successfully used in the real blood sample study.

5.2.4 Conclusion

In summary, a fast and reusable ECPA has been successfully developed. Several optimizations are achieved. For example, by using uracils sequence, this assay can be enzymatically regenerated for both Aptamer-based and antibody-based ECPA. A detection time of only 3 minutes was achieved without losing the sensitivity and selectivity. In addition, monitoring insulin secretions from pancreatic islets was accomplished and the antibody based-ECPA can be used in the measurement of blood serum. It can be concluded that the general ECPA sensor design has great potential for point-of-care application for various protein detections. More studies are being carried out to further improve the sensitivity of the sensor.

Name	Abbreviation	DNA sequence, listed 5′ to 3′
ECPA-MB	MB-DNA	CCA CCC TCC TCC TTT TCC TAT CTC TCC CTC GTC ACC A**U**G C/MB-C7/
ECPA-Gold-10	G10	/5ThioMC6-D/GCA TGG TGA CAT TTT TCG TTC GTT AGG GTT CAA ATC CGC G
ECPA-Gold-7	G7	/5ThioMC6-D/GCA TGG TAT TTT TCG TTC GTT AGG GTT CAA ATC CGC G
ECPA-Gold-5	G5	/5ThioMC6-D/GCA TGA ATT TTC GTT CGT TAG GGT TCA AAT CCG CG
Thrombin aptamer A	THRaptA	AGTCCGTGGTAGGGCAGGTTGGGGTGACTTTTTTTTTTTTTTTTTTATATTTTTTTTT CTCGCGGA**UUU**GAACCC**U**AACG
Thrombin aptamer B	THRaptB	TAGGAAAAGGAGGAGGGTGGGATTGGTGTGTGTTTTTTTTTTTTTTTTTTTTTTTTT TTTTTTTTTGGTTGGTGTGGTTGG
Insulin antibody arm 1	AbArm1	/5AmMC6//iSp18/CCC ACT TAA ACC TCA ATC CAC GCG GA**U** **UU**G AAC CC**U** AAC G
Insulin antibody arm 2	AbArm2	TAG GAA AAG GAG GAG GTG GCC CAC TTA AAC CTC AAT CCA/iSp18//3AmMC6

Table 5.2.1 DNA Oligonucleotides used in the ECPA sensor.

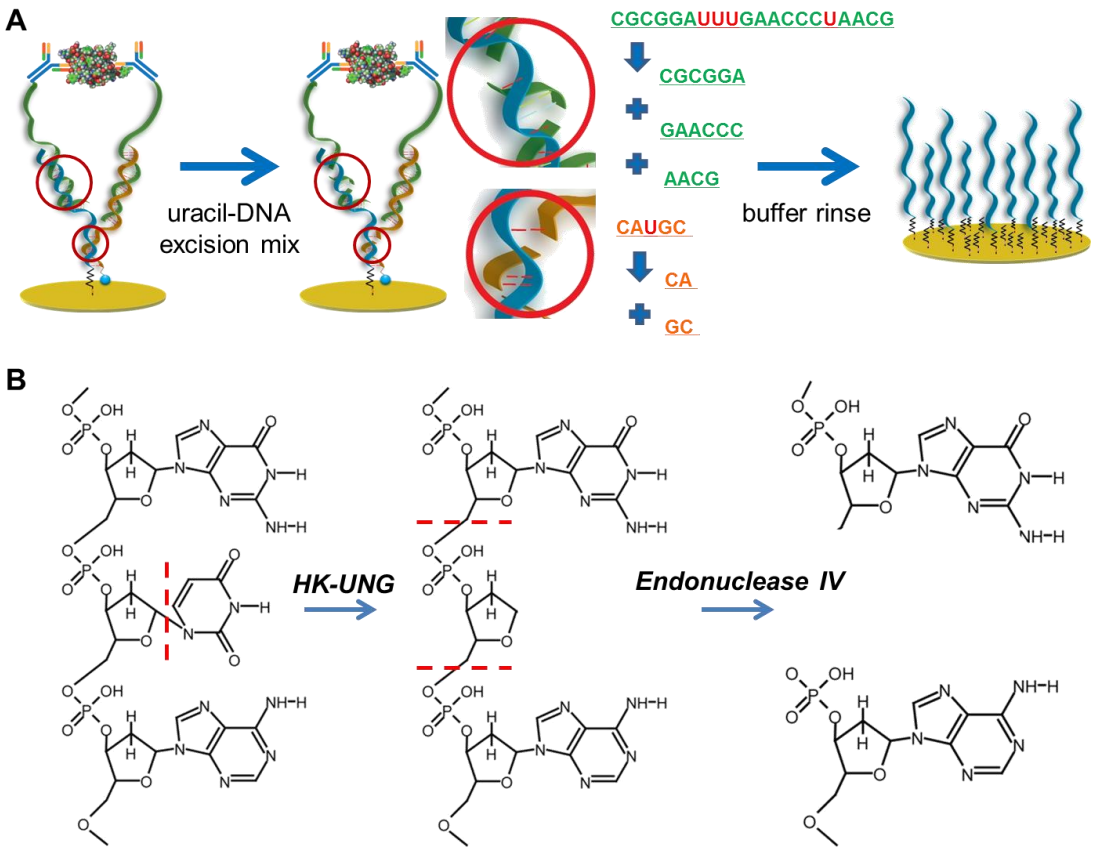

Figure 5.2.1 Illustration of the principle of the reusable ECPA. A) Reusable ECPA assay, B) Demonstration of uracil-DNA excision mix mechanism.

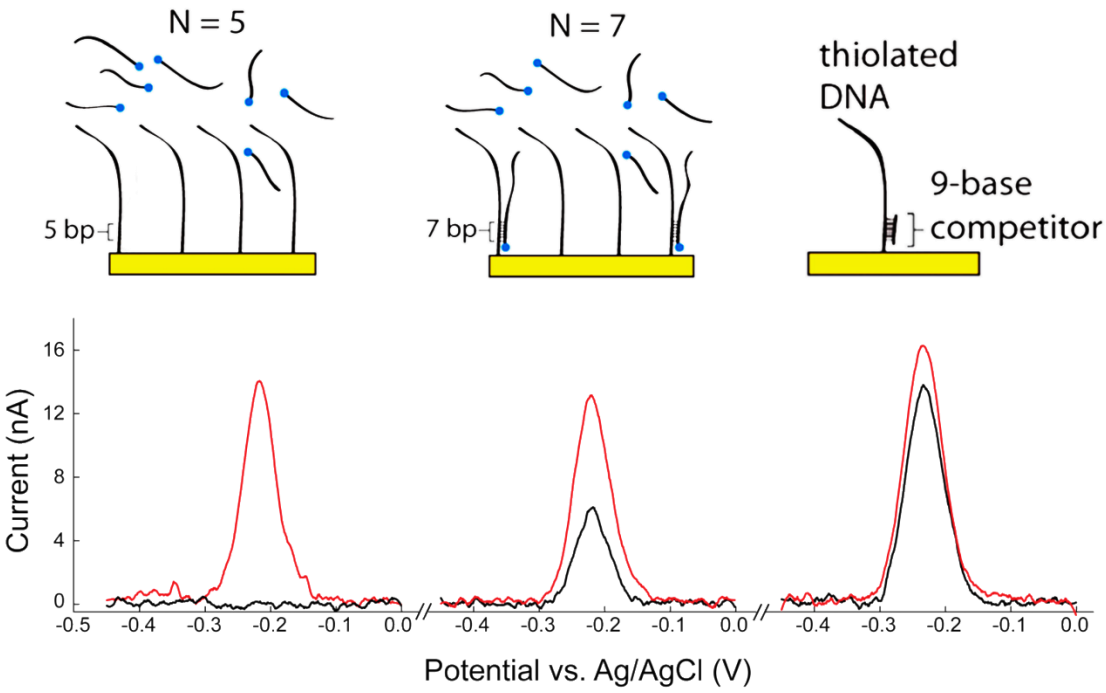

Figure 5.2.2 Comparisons of responses from the G5, G7, and G10 with C9 competitor in model system.

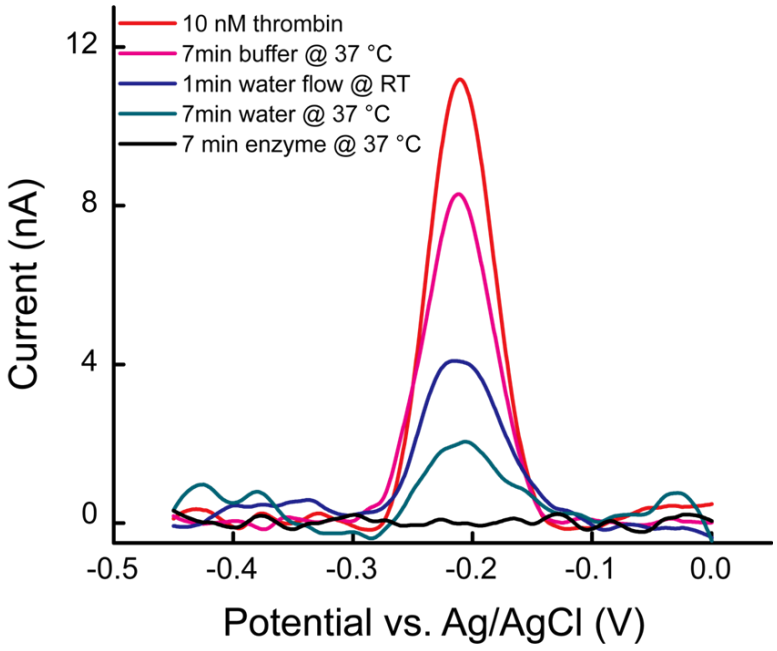

Figure 5.2.3 Uracil enzyme regeneration method comparisons with other three commonly used methods.

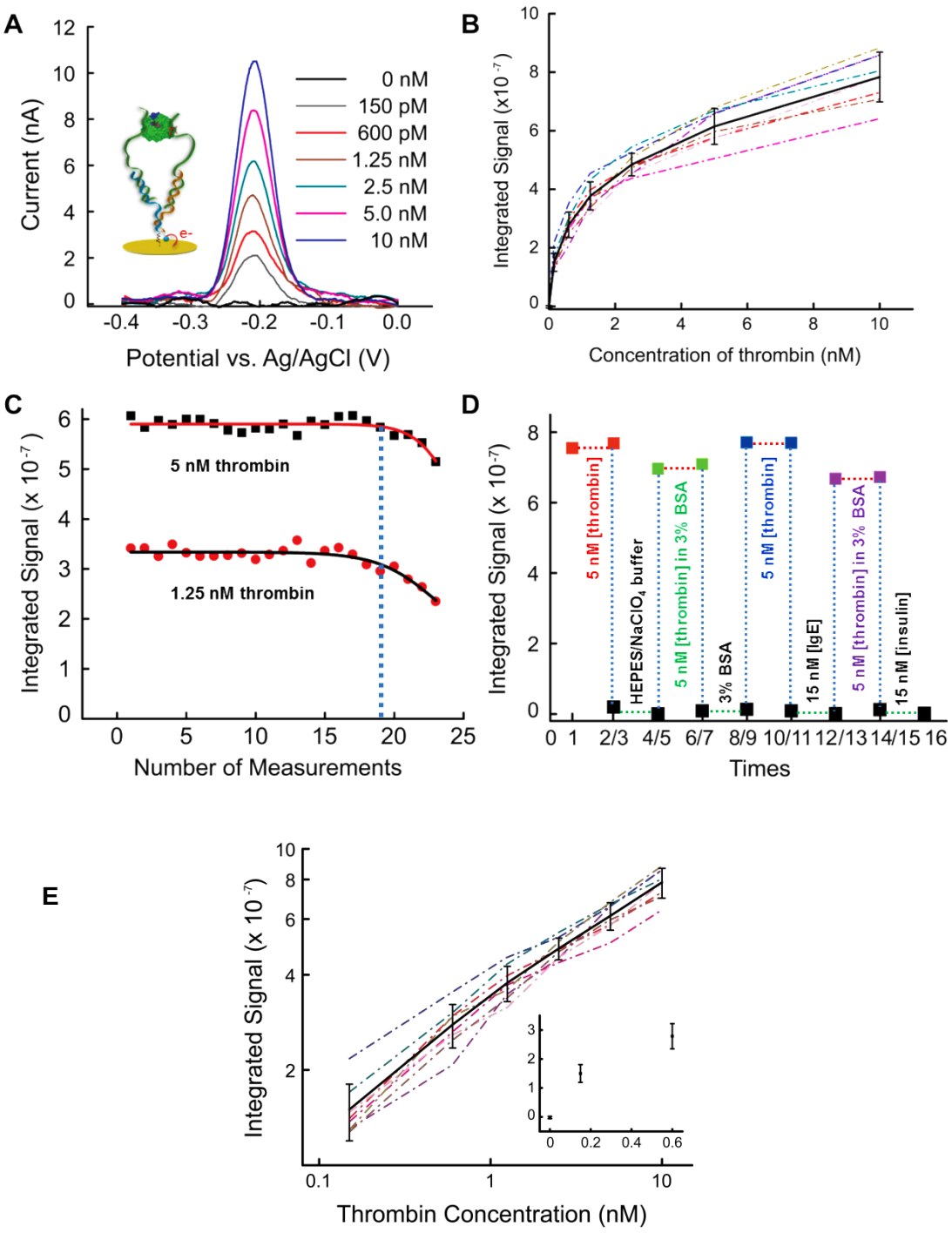

Figure 5.2.4 Aptamer-based reusable ECPA for thrombin detection. A) Signal responses of varying thrombin concentration from pM to nM. B) Calibration curves. Black line with error is the average data with 7 electrodes. C) Reusable times study, using 5nM and 1.25 nM thrombin separately. D) Selectivity of reusable ECPA against BSA, IgE, and Insulin. E) Linear range of calibration curve.

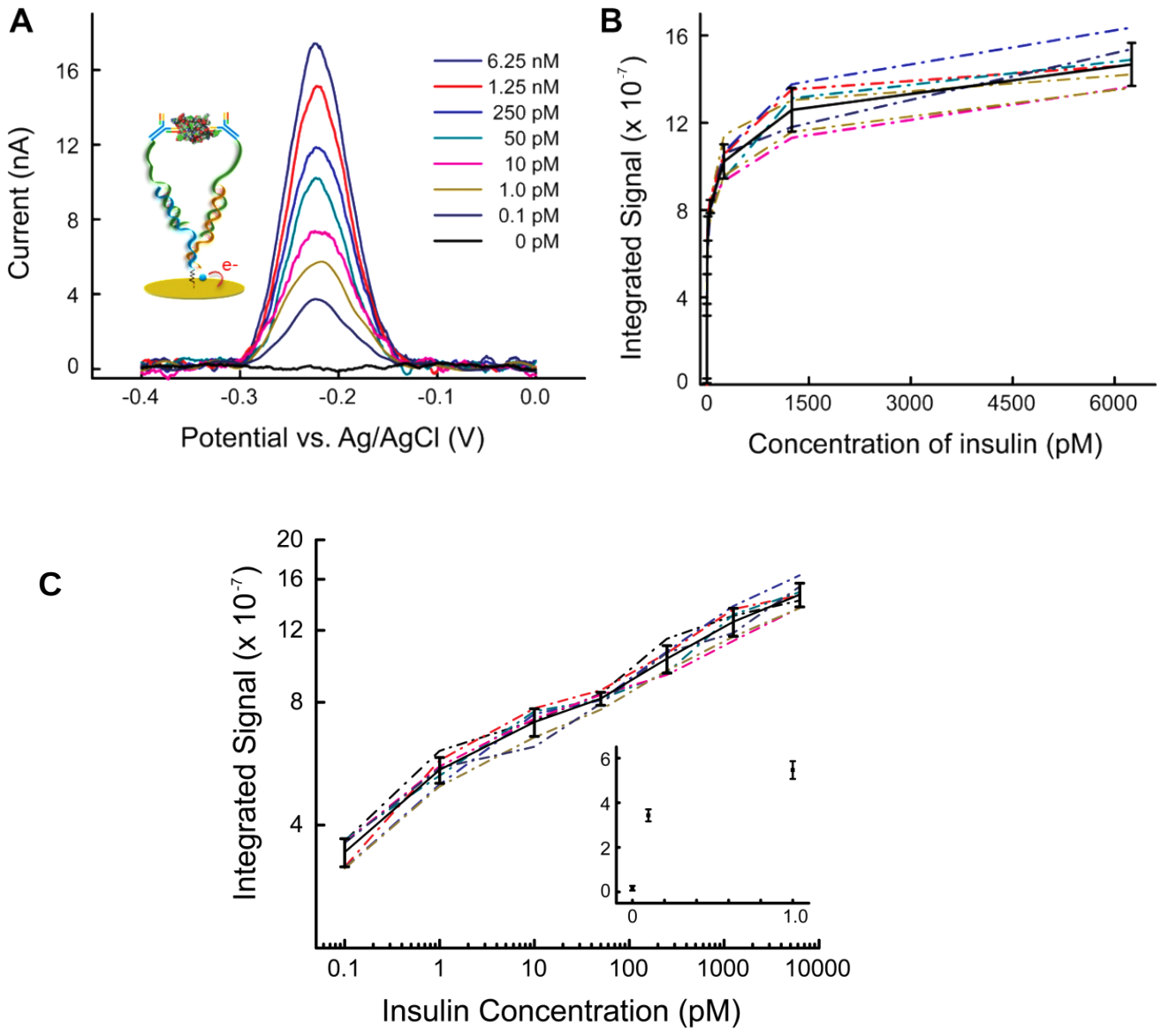

Figure 5.2.5 Antibody-based reusable ECPA for insulin detection. A) ECPA sensor response with different insulin concentrations from 100 fM to 6.25 nM. B) Calibration curves generated by seven different electrodes, the black curve represent the average data. C) Calibration curve with concentration from 0.1pM to 10nM.

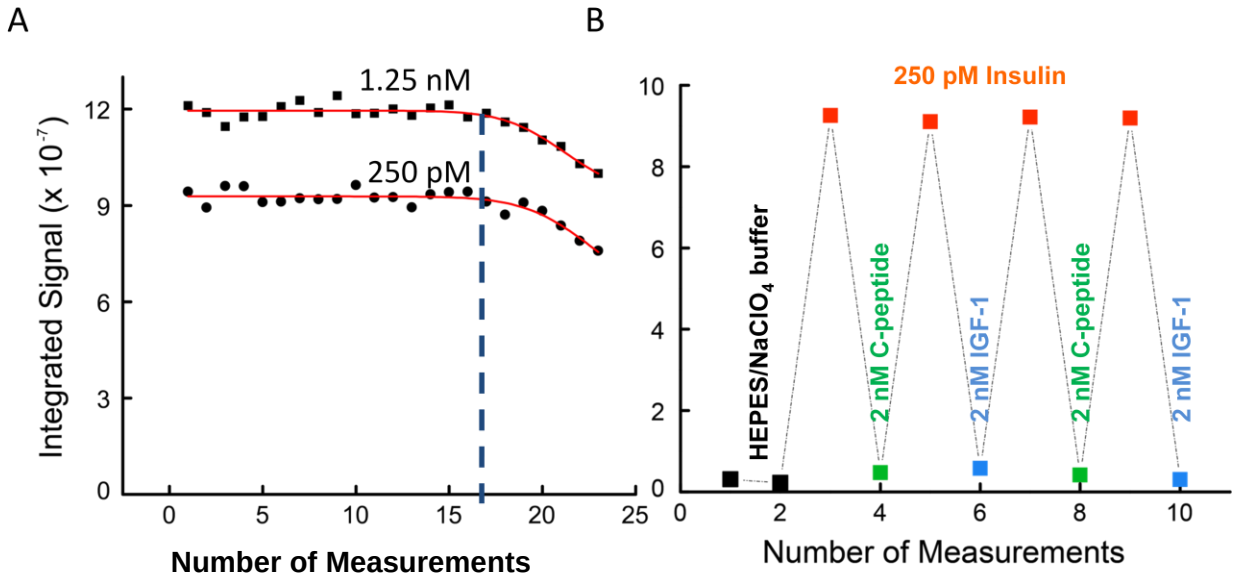

Figure 5.2.6 Regeneration times and selectivity of antibody based ECPA. A) Regeneration times of ECPA with insulin concentration of 1.25 nM and 250 pM. B) Reusable ECPA selectivity study against C-peptide and IGF with 8 times concentration.

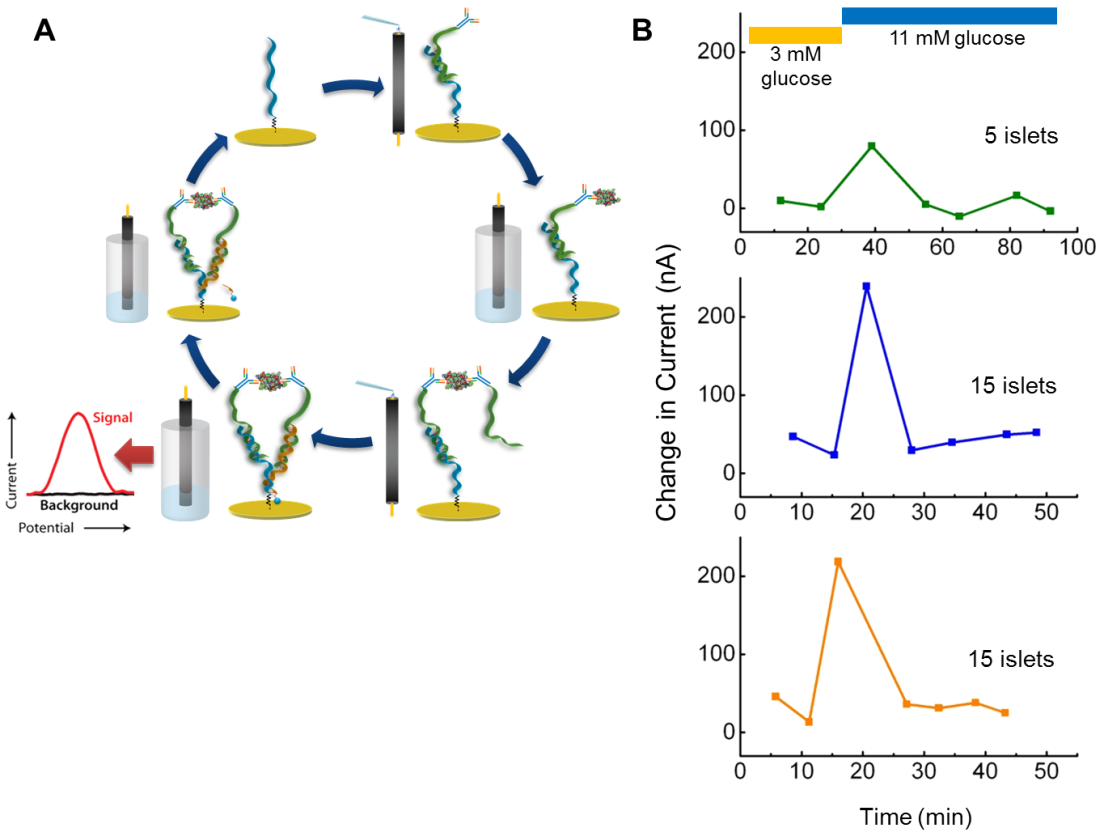

Figure 5.2.7 Monitoring of insulin secretion from endocrine tissue by using antibody-based reusable ECPA. A) Sensor fabrication process (cyclic approach). B) Insulin secretion detection from 5 and 15 mouse pancreatic islets during basal (3 mM) and stimulatory (11 mM) glucose levels. The data are plotted as the difference of the integrated area versus time.

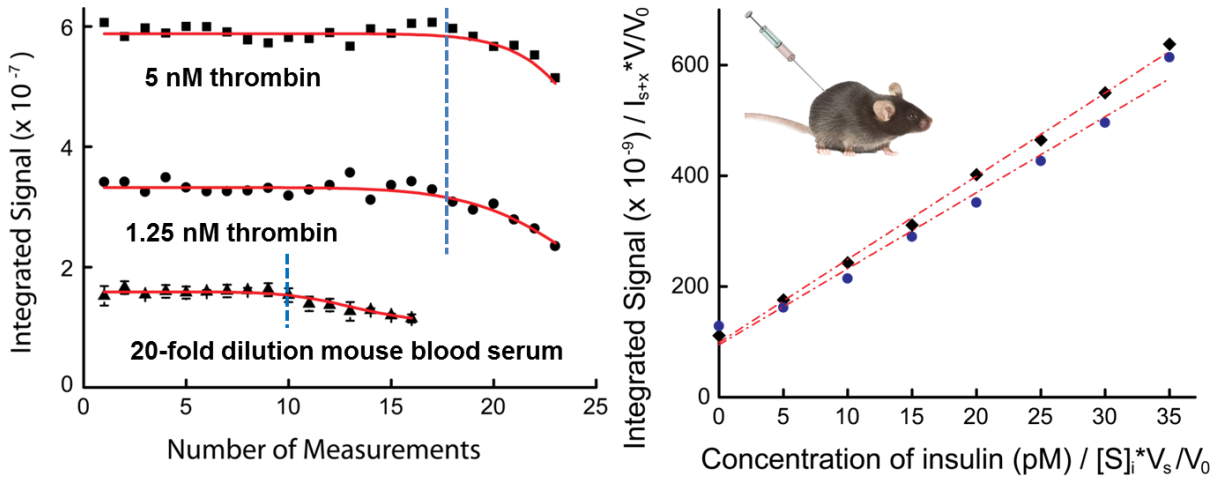

Figure 5.2.8 Insulin detection from mouse blood serum by using antibody ECPA. A) 01 regeneration times under the 20-fold diluted mouse blood serum. B) Standard addition method for insulin detection from blood serum from two different mice. Diluted by a factor of 20.

References

[1] Burgess, H. D.; Wasserman , J.; Dahl, C. A. *Global health diagnostics* **2006**.

[2] Yager, P.; Domingo, G. J.; Gerdes, J.; *Annu. Rev. Biomed. Eng*. **2008**. *10*, 107.

[3] Burgess, H. D.; Wasserman, J.; Dahl, C. *Nature* **2006**, *444*, 1.

[4] Wang, J. *Biosens. Bioelectron.* **2006**, *12*, 1887.

[5] Burtis, C. A.; Ashwood, E. R. *Textbook of Clinical Chemistry*. Saunders, Philadelphia, PA, **1999**.

[6] Rusling, J. F.; Kumar, C. V.; Gutkind, J. S.; Patel, V. *Analyst* **2010**, *135*, 2496.

[7] Sorell Gómez, L.; Rojas, G. *Clin. Chim. Acta* **1997**, *260*, 65.

[8] Jung, K.; Zachow, J.; Lein, M.; Brux, B.; Sinha, P.; Lenk, S.; Schnorr, D.; Loening, S. A. *J. Urol.* **1999**, *53*, 155.

[9] Stivers, C. R.; Baddam, S. R.; Clark, A. L.; Ammirati, E. B.; Irvin, B. R.; Blatt, J. M. *Diabetes Technol. Ther*. **2000**, *2*, 517.

[10] Davies, S; Byrn, F; Cole, L. A. *Clin. Lab. Med.* **2003**, *23*, 257.

[11] Seamark, D. A.; Backhouse, S. N.; Powell, *R. Ann. Clin. Biochem*. **2003**, *40*, 178.

[12] Sander, C. *Science*, **2000**, *287*, 1977.

[13] Huntington, W.; Misha, A.; Geoffrey, G.; *Philos. Trans. R. Soc.* B, **2005**, *360*, 1543.

[14] Feltis, B. N.; Sexton, B. A.; Glenn, F. I.; Best, M. J.; Wilkins, M.; Davis, T.J. *Biosens. Bioelectron.* **2008,** *23*, 1131.

[15] Hao, Y.; Foster, R. *Phys. Meas.* **2008**, *29*, R27.

[16] Millan, K. M.; Saraullo, S.; Mikkelsen, S. R. *Anal. Chem.* **1994**, *66*, 2943.

[17] Piunno, P. A. E.; Krull, U. J,; Hudson, R. H. E.; Damha, M. J.; Cohen, H. *Anal. Chim. Acta,* **1994**, *288*, 205.

[18] Minunni, M.; Tombelli, S.; Scielzi, R.; Mannelli, I,; MasciniMand, G. C. *Anal. Chim. Acta* **2003**, *48*, 55.

[19] Sawata, S, Kai, E.; Ikebukuro, K.; Iida, T.; Honda, T.; Karube, I. *Biosens. Bioelectron.* **1999**, *14*, 397.

[20] Kelley, S. O.; Boon, E. M.; Barton, J. K.; Jackson, N. M.; Hill, M. G. *Nucleic Acids Res.* **1999**, *27*, 4830.

[21] Drummond, T. G.; Hill, M. G.; Barton, J. K. *Nat. Biotechnol.* **2003**, *21*. 2.

[22] Plaxco, K. W.; Soh, H. T. *Trends Biotechnol*. **2011**, *29*, 1.

[23] Stefano, C.; Marcelo, C.; Carlotta, G.; Paolo, M.; Marty, R.; Mark, S.; David, D.; Todd, W.; Gerolamo, L. *Sensors* **2009**, *9*, 3122.

[24] Xia, F.; White, R. J.; Zuo, X.; Patterson, A.; Xiao, Y.; Kang, D.; Gong, X.; Plaxco, K. W.; Heeger, A. J. *J. Am. Chem. So*c. **2010**, *132*, 14346.

[25] Kang, D.; Zuo, X.; Yang, R.; Xia, F.; Plaxco, K. W.; White, R. J. *Anal. Chem*. **2009**, *81*, 9109.

[26] Zuo, X.; Xiao,Y.; Plaxco, K. W. *J. Am. Chem. Soc*. **2009**, *131*, 6944.

[27] Baker, B. R.; Lai, R.Y.; Wood, M. S.; Doctor, E. H.; Heeger, A. J, Plaxco, K. W. *J. Am. Chem. Soc.* **2006**, *128*, 3138.

[28] Xiao, Y.; Lubin, A. A.; Baker, B. R.; Plaxco, K. W.; Alan, J. *Proc. Natl. Acad. Sci. USA* **2006**, *103*, 16677.

[29] Liu,Y.; Tuleouva, N.; Ramanculov, Er.; Revzin, A, *Anal. Chem.* **2010**, *82*, 8131.

[30] Hu, J.; Wang, T.; Kim, J.; Shannon, C.; Easley, C.J. *J. Am. Chem. Soc.* **2012**, *134*, 7066.

[31] Fredriksson, S.; Gullberg, M.; Jarvius, J.; Olsson, C.; Pietras, K.; Gústafsdóttir, S. M.; Östman, A.; Landegren, U. *Nature Biotechnol*. **2002**, *20*, 473.

[32] Kim, J.; Hu, J.; Sollie, R. S.; Easley, C. *J. Anal. Chem*. **2010**, *82*, 6976.

[33] Xiao, Y.; Lai, R. Y.; Plaxco, K. W. *Nat. Protocols* **2007**, *2*, 2875.

[34] Rowe, A. A.; Chuh, K. N.; Lubin, A. A.; Miller, E. A.; Cook, B.; Hollis, D.; Plaxco, K. W.

Anal. Chem. **2011**, *83*, 9462.

[35] Gullberg, M.; Gustafsdottir, S. M.; Schallmeiner, E.; Jarvius, J.; Bjarnegård, M.; Betsholtz, C.; Landegren, U.; Fredriksson, S. *Proc. Natl. Acad. Sci*. **2004**, *101*, 8420.

[36] Heyduk, E.; Dummit, B.; Chang, Y. H.; Heyduk, T. *Anal.Chem*. **2008**, *80*, 5152.

[37] Gearheart, L. A., Ploehn, H. J., Murphy, C. J., *J. Phys. Chem. B.* **2001**, *105*, 12609.

[38] Esplandiu´, M. J.; Hagenstro¨m, H.; Kolb, D. M. *Langmuir* **2001**, *17*, 828.

[39] Rivera-Gandía , J.; Cabrera, C. R. *J. Electroanal. Chem*. **2007**, *605*, 145.

[40] Porter, M. D.; Thomas, S.; Bright, T. B.; Allara, D. L.; Chidseyi, C. E. D.; *J. Am. Chem. Soc*. **1987**, *109*, 3559.

Chapter 6

Conclusions and future work

In summary, this research focused on two aspects: biosensor development and optimization for human disease related study and the hybrid materials study for supercapacitor applications. The work for the biosensor includes the development of one DNA biosensor based on surface-enhanced Raman scattering, and the optimization of electrochemical proximity assay for protein detection via electrochemical techniques.

For the system, Ag/Au film over nanoshpere substrate was fabricated and optimized. The substrate showed high enhancement of Raman intensity and relatively good reproducibility. Using a series of thiols as spacer, the distance-dependent phenomenon of the SERS effect was also modeled in our system. Further, a DNA biosensor was successfully developed based on the conformational changes of the DNA sequence before and after the hybridization process. The DNA sensor consists of a hairpin structure DNA probe labeled with a Raman reporter and a free labeled target DNA. The calibration curve with different concentrations of target sequence is accomplished, with the largest SERS signal change being 65% of the original signal. To miniaturize the system, microfluidic channels were designed. However, more studies are needed to improve the sensitivity of the response. In addition, because SERS is a potential technique for multiplexing, a multiplexing system to simultaneously detect several different DNA sequences needs to be investigated.

Two types of hybrid material were fabricated using cathodic deposition of Mn_3O_4 on both stainless steel fiber and carbon fiber. Compared with stainless steel fiber, the carbon fiber exhibits a higher capacitance. By controlling the deposition time, the capacitance of the material can be optimized. In addition, the cathodic method has the advantage that the dissolution of the Mn_3O_4 can be prevented. However, more detailed studies are needed for the practical application of the materials. These include better control of the fabrication process. In addition, the thermal stability and cycle duration also need to be studied to better understand the supercapacitor performance.

Finally, several optimizations of standard ECPA were achieved. A faster, reusable ECPA sensor was accomplished with high sensitivity and selectivity. By incorporating Uracil bases enzyme in the probe sequences, the ECPA system can be regenerated using a cleavage. This allows the sensor to be reused up to 20 times with excellent signal recovery and selectivity. Moreover, the sensor has a faster detection time window of only 3 minutes at body temperature without losing its selectivity. Co-immobilization of the thiolated DNA probe with a back-filler (mercaptohexanol (MCH)) was used to reduce the background noise. Based on these developments, higher sensitivity for insulin detection in the 100 fM range was accomplished, and insulin detection from pancreatic islets at 37^oC and the direct detection of insulin from mouse blood serum were realized. The ECPA is a general design which can be suitable to any aptamer protein or antibody-antigen couple. However, more work has to be done to further improve the system toward point-of-care application. SPR and electrochemical techniques will be used to study the mechanism of the modification process in order to improve the performance of the sensor. Using lab-on-chip techniques, miniaturized and integrated electrochemical ECPA can be achieved with multiplexing ability.